Annual Report 2001

Address: Prof. Dr. Burkard Hillebrands
Fachbereich Physik
Universität Kaiserslautern
Erwin-Schrödinger-Straße 56
67663 Kaiserslautern, Germany
Tel.: +49-(0)631-205-4228
Fax: +49-(0)631-205-4095

Postal address: Postfach 3049
67653 Kaiserslautern, Germany

Internet: http://www.physik.uni-kl.de/w_hilleb/w_hilleb.html
E-Mail: hilleb@physik.uni-kl.de

Our Group

From left to right:

Thomas Wittkowski, Oscar Liedke, Martin Lesmeister, Sybille Müller, Dr. Jürgen Fassbender, Hans Nembach, Mathias Mautner, Bernd Pfaff, Gerd Distler, Heike Schuster, Andreas Beck, Stefan Poppe, Tim Mewes, Dr. Alexander Serha, Dr. Sergey Demokritov, Dr. Kurt Jung, Prof. Dr. Burkard Hillebrands, Marc Rickart

Contents

Chapter 1: Introduction

Dear colleagues and friends,

another successful year of research lies behind us, and it is a pleasure for us, to summarize the results in this report. We cover the period November 2000 to October 2001.

Our main research area, magneto-electronics, is fast moving. There are several new results in different areas of magneto-electronics you will find in this report. They range from fundamental results like insight into the dynamic eigen-excitations in small, inhomogeneously magnetized islands, the generation of bullet spin wave trains, the development of new epitaxial growth templates for MBE-growth of magnetic structures, new studies of the modification of the exchange bias effect by ion irradiation, and the improvement of the fabrication of magnetic tunnel junctions by ion embedding, just to name a few projects.

The key field still is magnetization dynamics. We address the problems with such different approaches like Brillouin light scattering, time resolved magneto-optic Kerr effect magnetometry and studies of nonlinear spin wave propagation in one- and two-dimensional structures. The work was rewarded this year by the decision of the Deutsche Forschungsgemeinschaft, to establish a center ("Schwerpunkt") on magnetization dynamics in Germany, which will start operation next summer.

Our second area of interest, the field of hard and wear resistant films and coatings, is the subject of our Institut für Dünnschichttechnologie – Transferstelle der Universität Kaiserslautern (Institute for Thin Film Technology – Center for Technology Transfer of the University of Kaiserslautern) located in Rheinbreitbach at the northern boarder of Rheinland-Pfalz. Our work concentrates increasingly around carbon films for medical applications. Since January 2001 Lisa Kleinen is in charge of the operation in Rheinbreitbach. Two members of our institute, Heinz Busch and Udo Grabowy, have founded their company Nuclear Thin Film Technology (nttf) as scheduled, and thus left our institute. They were members of the institute for a period of 2 years as part of a initiative of the state of Rheinland-Pfalz to found young enterprises in high-tech areas.

Again, a lot of work has been carried out in close collaboration with partner laboratories all over the world. I just would like to name the collaboration in the European Training and Mobility Network DYNASPIN, which will come to an end this November. As a result of this network, Alexandra Mougin, who worked as a post-doc in our lab, received a permanent position as a "chercheur" in Jacques Ferré's group at the CNRS in Orsay, and Jean Juraszek, who followed Alexandra on the post-doc position here in Kaiserslautern, received a permanent position as a "Maître de Conference" at the University in Rouen.

Four group members, Martin Bauer, Andre Frank, Jörg Jorzick and Björn Roos successfully completed their PhD work. They all found very attractive positions.

Our work would not have been possible without valuable collaborations with people all over the world. We would like to thank, in alphabetical order, Joachim Bangert, Bernard Bartenlian, Harry Bernas, Klaus Bewilogua, John Chapman, Claude Chappert, John Cochran, Horst Dötsch, Ursula Ebels, Giancarlo Faini, Claude Fermon, Jacques Ferré, Zdenek Frait, Ingo Gestmann,

Uwe Hartmann, Volker Herzog, Boris Kalinikos, Kathrine Kirk, Jürgen Klipfel, Mikhail Kostylev, Natatia Kreines, Achim Lunk, Wolfram Maaß, Roland Mattheis, Andrzej Maziewski, Ulrich Memmert, Jacques Miltat, Fabrizio Nizzoli, Kamel Ounadjela, Carl Patton, Yuri Rapoport, Theo Rasing, Frank Richter, John R. Sandercock, Andrei Slavin, Bob Stamps, Evgueni Tsymbal, Stefan Visnovsky, Joachim Wecker and Manfred Weiler for their interactions with us and their strong input on our work. Collaborations within the Fachbereich Physik at the University of Kaiserslautern (Martin Aeschlimann, Hans Schmoranzer, Herbert Urbassek, Richard Wallenstein and Christiane Ziegler and their groups) and the Institut für Oberflächen- und Schichtanalytik (Hans Oechsner and his group) have been very stimulating. I am especially grateful to Dr. Heinz Busch and Dr. Udo Grabowy and their start up company nttf GmbH for the close contact after they left our institute and their participation in all biomedical projects. I am much obliged to Walter Meuer and Dr. Stefan Sattel and the team from the TZO GmbH for providing convenient general conditions for our work in Rheinbreitbach.

I would also like to thank all our sponsors, which are the Deutsche Forschungsgemeinschaft, the Bundesministerium für Bildung, Wissenschaft, Forschung und Technologie, the Humboldt Foundation, the Deutscher Akademischer Austauschdienst, the European Community, the European Science Foundation, INTAS, the State of Rheinland-Pfalz and the University of Kaiserslautern. My special thanks go to Tim Mewes, Sibylle Müller and Heike Schuster for their technical help in preparing this report.

It is my special pleasure to greet all former group members. May this report help to stay in touch with each other.

If you are interested in our work I would be happy to hear from you. If you have any questions, comments, suggestions, or any kind of criticism, please contact us.

With all my best wishes for Christmas, and a Happy New Year,

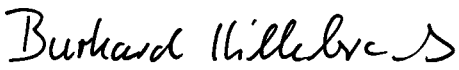

Kaiserslautern, November 2001

Chapter 2: Personnel

2.1 Members of the Group

Group leader:

Prof. Dr. Burkard Hillebrands

Senior scientists:

Dr. Heinz Busch, Wiss. Assistent (Rheinbreitbach)	until 04/01
Dr. habil. Sergey Demokritov, Hochschuldozent	
Dr. Jürgen Fassbender, Wiss. Assistent	
Dr. Jürgen Grabowy, Wiss. Assistent (Rheinbreitbach)	until 04/01
Dr. Kurt Jung, Akad. Direktor	

Postdocs:

Dr. Jean Juraszek	until 08/01
Dr. Alexander Serha	since 08/01

PhD students:

Dipl.-Phys. Martin Bauer	until 02/01
Dipl.-Phys. Andreas Beck	since 09/01
Dipl.-Phys. André Frank	until 11/00
Dipl.-Phys. Jörg Jorzick	until 07/01
Dipl.-Phys. Lisa Kleinen	since 10/00
Dipl.-Phys. Radek Lopusnik	
Dipl.-Phys. Tim Mewes	
Dipl.-Phys. Hans Nembach	
Dipl.-Phys. Stefan Poppe	
Dipl.-Phys. Marc Rickart	
Dipl.-Phys. Björn Roos	until 07/01
Dipl.-Phys. Thomas Wittkowski	

Diploma students:

Gerd Distler	since 01/01
Christian Krämer	until 08/00
Martin Lesmeister	since 12/00
Markus Weber	since 10/01

Engineers and Technicians:

Dipl.-Ing. (FH) Mathias Mautner
Bernd Pfaff
Sven Schlierkamp (Rheinbreitbach) until 08/01

Secretary:

Sibylle Müller
Heike Schuster (Schwerpunkt Materialwissenschaften)

2.2 Visiting Scientists, Postdoctoral Fellows and Exchange Students

Prof. Dr. Carl E. Patton, Colorado State University,
Fort Collins, U.S.A. January 01

Carl spent another month to complete his sabbatical in our lab supported by the Alexander von Humboldt foundation. He worked mostly on time resolved Brillouin light scattering experiments and on the analysis of the mode spectrum measured by time resolved magneto-optic Kerr magnetometry.

Dr. Zdenek Frait, Academy of Science, Prague, Czech Republic 21.05.01 – 24.05.01

This was a visit to discuss Ferromagnetic Resonance and to prepare future visits of group members in Prague to perform Ferromagnetic Resonance experiments on exchange bias systems.

Dr. Alexander Serga, Radiophysical Faculty, Taras Shevchenko
Kiev University, Kiev, Ukraine since 08/01

Alexander is working on the problem of nonlinear spin waves financed by a DFG project. In particular he works on time resolved Brillouin light scattering and experiments for parametric pumping of wave packets.

Prof. Dr. Andrei Slavin, University of Rochester, Michigan, U.S.A. 16.07.01 – 31.07.01

Andrei spent a short research stay in our lab. He was heavily involved in the modeling of nonlinear spin wave propagation and in the modeling of laterally quantized spin wave modes in confined magnetic objects.

Dr. Jean Juraszek, Université de Rouen, Rouen, France 01.11.00 – 31.08.01

Jean worked on ion irradiation induced defects in exchange biased bilayers. His special research topic was the role of different antiferromagnetic materials in this effect and the aspects of chemical ordering.

Dmitri Kholin and **Alexey Drovosekov,**
Ph.D. students, Institute for Physical Problems, Moscow, Russia. 16.06.01 – 15.07.01

Dmitri and Alexey spent one month in Kaiserslautern preparing and investigating high-quality magnetic Fe/Cr/Fe bilayers. They were supported through the Leonard-Euler-Fellowship of the DAAD. The main scientific goal of this project is to understand the temperature dependence of the bilinear and biquadratic interlayer coupling constants. For this purpose static remagnetization curves, ferromagnetic resonance, as well as Brillouin light

scattering from spin waves is under investigation in Kaiserslautern and in Moscow.

Oskar Liedke, Diploma student, University of Bialystok, Poland 10.08.01 – 31.10.01

Oskar spent almost three months in the frame work of a student exchange programme between University Kaiserslautern and University Bialystok. He was supported by the Sokrates program. He has learned magneto–optic magnetometry and has contributed to our research programs on vicinal magnetic films, and ion-beam-induced changes of the interlayer coupling in magnetic multilayers.

2.3 Guest Seminars

Dr. Harry Bernas 02.11.00	CSNSM-CNRS, Université d´Orsay, France *How ion irradiation may affect magnetic properties: the 3D, 2D, 0D cases* Materialwissenschaftliches Kolloquium
Dr. Giancarlo Faini and Cecile Naud 02.11.00	CNRS, Bagneux *Quantum transport in nanostructures* Sonderkolloquium im Materialwissenschaftliches Kolloquium
Prof. Dr. A. Maziewki 06.11.00	University of Bialystok, Polen *Magnetization processes and domain structures in ultrathin cobalt films* Sonderseminar
Dr. Nicolas Vernier 14.12.00	Laboratoire de Physique des Solides, Université Paris-Sud, France *Tunneling of large spins in anisotropic materials* Materialwissenschaftliches Kolloquium
Dr. A. Hölscher 08.02.01	Infineon, München, Germany *The development of the 0,13 µm CMOS process technology at Infineon Technologies* Materialwissenschaftliches Kolloquium
K. Vyborny 14.05.01	Institute of Physics, Charles-University Prague *Magnetotransport in two-dimensional small-period superlattices* Sonderseminar
Dr. Zdenek Frait 23.05.01	Institute of Physics, Academy of Sciences, Prague *Ferromagnetic resonance and antiresonance linewidth in metallic samples* Sonderkolloquium im Materialwissenschafltichen Kolloquium
Dr. R. Schäfer 31.05.01	IFW Dresden, Germany *Kerr-mikroskopische Untersuchungen dünner magnetischer Schichten* Materialwissenschaftliches Kolloquium
Prof. Dr. W.D. Doyle 13.06.01	MINT, University of Alabama, USA *A review of future storage technologies* Sonderkolloquium im Materialwissenschaftlichen Kolloquium

Dr. A. Dietzel 21.06.01	IBM Mainz, Germany *Magnetische Festplattenspeicher und ausgewählte F+E-Projekte der IBM Mainz* Materialwissenschaftliches Kolloquium
Dr. T. Silva 22.06.01	NIST, Boulder, Colorado, USA *Consideration of the spherical cow: the realities of magnetodynamics in an imperfect world* Sonderkolloquium im Materialwissenschaftlichen Kolloquium und Laserzentrum
Prof. Dr. A.N. Slavin 16.07.01	Department of Physics, Oakland University, Rochester, USA *Dark solitons and bullets* Sonderseminar
J.V. Kim 20.08.01	Department of Physics, University of Western Australia, Perth, Australia *Defects and thermal properties of domain-wall driven exchange bias* Sonderseminar

2.4 Visits of group members at other laboratories

S.O. Demokritov	Institute for Physical Problems, Russian Academy of Science, Moscow, Russia 10.08-20.08.01 Host: Prof. N. Kreines
B. Hillebrands	Hawaiian Institute of Geophysics and Planetology, Honolulu, USA 05.05.-08.05.01 Host: Prof. M.H. Manghnani
B. Hillebrands	LPS and IEF Orsay, France 01.10. – 05.10.01 and 17.10.–02.11.01 Host: Dr. J. Ferré
T. Mewes	IFW Dresden 08.07. - 13.07.01 Host: Dr. R. Schäfer
H. Nembach	Academy of Sciences, Prague, Czech Republic 07.07.-14.07.01 Host: Dr. Z. Frait
S. Poppe	LPN Paris/Bagneux, France 26.02. - 02.03.01 Host: Dr. G. Faini
S. Poppe	Synchrotron LURE, Orsay, France 02.04.-06.04.01 Host: Dr. F. Bertrand

2.3 Group Member Photo Gallery

Martin Bauer
Ph.D. student

Andreas Beck
Ph.D. student

Dr. Heinz Busch (Rbb)
Senior scientist

Dr. habil. Sergey Demokritov
Senior scientist and lecturer

Gerd Distler
Diploma student

Dr. Jürgen Fassbender
Senior scientist

André Frank
Ph.D. student

Dr. Udo Grabowy (Rbb)
Senior scientist

Prof. Dr. Burkard Hillebrands
Group leader

Rbb: Institut für Dünnschichttechnologie, Rheinbreitbach

Jörg Jorzick
Ph.D. student

Dr. Kurt Jung
Senior scientist

Dr. Jean Juraszek
Guest scientist

Lisa Kleinen (Rbb)
Ph.D. student

Martin Lesmeister
Diploma student

Oskar Liedke
visiting Diploma student

Radek Lopusnik
Ph.D. student

Mathias Mautner
Mechanical engineer

Tim Mewes
Ph.D. student

Sibylle Müller
Secretary

Hans Nembach
Ph.D. student

Bernd Pfaff
Technician

Stefan Poppe
Ph.D. student

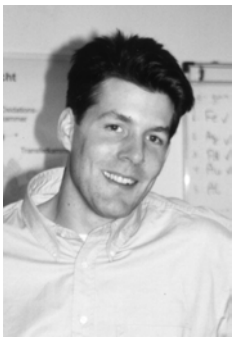

Marc Rickart
Ph.D. student

Björn Roos
Ph.D. student

Sven Schlierkamp (Rbb)
Technician

Heike Schuster
Secretary

Alexander Serha
Guest scientist

Markus Weber
Diploma student

Thomas Wittkowski
Ph.D. student

Chapter 3: Research Topics

The field of magnetism in films and multilayers is currently one of the strongest developing areas in modern solid state physics. This is caused both by the challenging developments in the discovery and understanding of the basic physical phenomena, and by the strong impact into industrial applications in the areas of sensors and information storage technology. New mechanisms like interlayer exchange coupling, the giant magnetoresistance effect, the room-temperature tunneling magnetoresistance effect, and, since very recently, spin current phenomena were discovered all within the last one and a half decade. Applications based on these effects were developed, like the magnetic read head based on the giant magnetoresistance effect found in nearly every hard disk drive sold nowadays. The combination with microelectronics, the so-called field of magneto-electronics is strongly expanding and bridging the gap between conventional magnetism and semiconductor physics in view of potential applications in sensor devices and magnetic random access memories.

Most of our research projects are in this field. We fabricate epitaxial layers and multilayers and study their structural, magnetic and magneto-transport properties.

One focus is in the field of spin dynamics. We study the eigen-frequency spectrum of excitations of the magnetization on the frequency scale using the Brillouin light scattering technique, and the temporal evolution by time resolved magneto-optic methods. We investigate high frequency properties like linear and nonlinear spin waves, time dependent magnetization effects, and fast magnetic switching.

A key issue is the fabrication of high-quality epitaxial film and multilayer systems and devices using molecular beam epitaxy as prototype systems to study fundamental problems.

In the field of applications we address problems of fast magnetic switching, the exchange bias effect and tunneling magnetoresistance. We transfer our results into actual devices by working closely together with industrial partners.

As a second working area we develop and investigate carbon films for medical applications in the framework of the Institute for Thin Film Technology in Rheinbreitbach. A special focus is on the determination of elastic properties of hard coating materials.

Overview on projects

1. Epitaxial magnetic films and multilayers: growth, structure and magnetic properties

The preparation of samples with highest possible structural quality and characterization is very important to be able to study magnetic phenomena with the necessary precision. We achieve this by using molecular beam epitaxy employing the standard in situ methods for chemical and structural analysis. They comprise Auger spectroscopy for chemical analysis, low and high energy electron diffraction, and *in situ* scanning tunneling and atomic force microscopy. To characterize the magnetic properties we perform *in situ* Brillouin light scattering spectroscopy and magneto-optic Kerr-magnetometry. *Ex situ*, the samples are investigated using Brillouin light scattering, vector Kerr magnetometry, vibrating sample magnetometry, and more. Scientific subjects are magnetic anisotropies induced at interfaces and by controlled defects, and interlayer coupling effects between magnetic films in multilayers.

Special attention is paid to the interplay between the morphology at the interfaces (atomic defects, steps, roughness and interdiffusion) and the magnetic properties. For example, magnetic

films grown on vicinal substrates representing templates with arrays of ordered atomic steps are a prototype system for a direct investigation of such interplays.

2. Exchange bias systems

The investigation of exchange bias systems is of fundamental as well as technological importance. The effect is a shift of the hysteresis loop along the field axis, and it appears in multilayers of coupled ferromagnetic and antiferromagnetic films. We study in particular structurally well characterized epitaxial bilayers. The role of defects and interfacial mixing is investigated using ion irradiation in order to artificially create disorder. Ion irradiation techniques are also applied to modify the magnitude and direction of the exchange bias field. This is of high technological interest, especially for magnetic sensor applications.

3. Tunneling magnetoresistance

A magnetoresistive tunnel device is basically a three-layer sandwich system consisting of two ferromagnetic electrodes separated by a very thin (~1nm thick) insulating barrier. The structure changes its electrical resistance (up to 50 % at room temperature) according to the relative orientation of the magnetizations of the two electrodes to each other. Its properties depend dramatically on the homogeneity and quality of the barrier layer. We investigate transport phenomena based on the magnetic tunneling effect with the aim to develop a new generation of magnetic sensors and nonvolatile memories. In a dedicated project we put special emphasis on the development of new methods for the preparation of the barriers and for the investigation of their crystallographic and chemical structures. We have introduced and developed a technology for preparation of thin oxide and nitride layers as tunnel barriers using low energy beams of ionized atomic oxygen/nitrogen. Monoenergetic, low-energy atomic oxygen ions are embedded into an Al film and allow for a very homogeneous formation of the tunnel barrier. Of particular interest are, e.g., the chemical and physical processes taking place during the preparation of the barriers.

4. Magnetic nanopatterning

Light ion irradiation is an excellent tool to locally modify magnetic properties on the submicrometer scale, without affecting the surface topography. This effect is used to magnetically pattern ultrathin films and multilayers using resist masks patterned by electron beam lithography. The major difference between this technique and conventional lithographic techniques is that the environment of the nanostructures can also be magnetic (paramagnetic, antiferromagnetic).

5. Dynamic magnetic properties of laterally patterned nanostructures

We investigate the basic magnetic properties of systems patterned on the micrometer to nanometer scale. In particular we focus on the domain structure and the change in the spin wave mode spectrum due to lateral confinement effects. We have developed a Brillouin light scattering setup, operating in a Fourier microscope like mode, to obtain sub-micrometer scale spatial information about the distribution of dynamic excitations in small magnetic objects. Using this method we have observed a lateral quantization of spin waves in magnetic stripes and rectangular elements. Main results are the observation of quantized modes and of edge modes existing in areas with a large internal field gradient, and static and dynamic coupling effects between magnetic objects.

6. Nonlinear properties of microwave excited spin waves

Spin waves with high precession angles, which can be excited using microwave stripe lines are an interesting object for the investigation of general effects of nonlinear wave propagation in dipersive, anisotropic, and dissipative media. Contrary to nonlinear optical pulses the spectrum of spin waves can be easily manipulated, by, e.g., changing the orientation and the value of the applied magnetic field. In addition spin waves are much slower than light pulses making their observation easier.

Using the time resolved Brillouin light scattering technique developed in our lab, we measure the intensity distribution of spin waves propagating in a magnetic film with spatial and temporal resolution. Central problems are: the propagation of spin waves in the linear and nonlinear intensity regimes, the formation of instabilities (e.g. self-focusing), the propagation of nonlinear excitations (solitons, magnetic "bullets") and collision experiments of these excitations. An important development of these studies is the investigation of self-generation of solitons and bullets in loops with a feedback and the development of a spin wave soliton “laser”.

7. Fast magnetic switching

For memory devices it is of special importance how fast and secure magnetic domains can be written or the magnetization of a single magnetic object can be reversed. The corresponding time scale is in the picosecond to nanosecond regime. In order to investigate these phenomena a time-resolved magneto-optic Kerr magnetometer has been constructed. The time evolution of the magnetization is sensed stroboscopically. The switching behavior and the write endurance of technologically relevant magnetic tunnel junction devices are studied.

8. Numerical simulations

Numerical simulations are used for several aspects. i) The evolution of the magnetization upon pulse field application is calculated and compared to the results of the time-resolved magneto-optic Kerr investigations. ii) Quasi static switching properties like the modification of the well known Stoner astroid by additional anisotropy or coupling contributions are studied. iii) The magnetization reversal behavior of epitaxial exchange bias layers is investigated with respect to different anisotropy contributions.

9. Elastic properties of hard, super-hard and inhomogeneous films and multilayers

We prepare hard and super-hard films and investigate their elastic properties using Brillouin light scattering. Research subjects are amorphous carbon (a-C:H and ta-C:H) and boron nitride films, which are prepared using unbalanced magnetron sputtering. The elastic constants are determined from the dispersion curves of surface and film phonons (Rayleigh and Sezawa modes). Our aim is to prepare hard and super-hard films with minimized internal stresses.

10. Biofunctionalized surfaces for medical applications

Amorphous thin carbon films are known to be very biocompatible, and they can be prepared by various deposition techniques to qualify for miscellaneous applications in the biological and medical field. At the Institute for Thin Film Technology we develop in close collaboration with our spin off company nttf GmbH biocompatible and biofunctionalized surfaces for medical implants and surgical instruments. Currently we are working on carbon coatings for intraocular lenses, cardiovascular stents and orthopedic implants as well as on the development of low temperature coating processes for temperature sensitive materials.

Chapter 4: Equipment

A) Preparation and characterization of thin films and multilayers

1. multi-chamber molecular beam epitaxy system (Pink GmbH) comprising
   a. deposition chamber
      (electron beam and Knudsen sources, RHEED, LEED, Auger)
   b. scanning tunneling and atomic force microscopy chamber
      (*in situ* STM/AFM, Park Scientific)
   c. Brillouin light scattering and Kerr magnetometry chamber
      (magnetic field 1.2 T, temperature range 80 – 400 K)
   d. load lock chamber
   e. preparation chamber
      (optical coating, heating station 2300° C)
   f. transfer chamber
   g. atom beam oxidization chamber with *in situ* four-probe resistively measurement stage
2. two-chamber UHV deposition system
3. two-magnetron sputtering system
4. scanning tunneling and atomic force microscope (TopoMetrix)

B) Patterning of magnetic films

1. UV laser interference lithography setup
2. clean room facility with flow box, spin coater, etc.
3. reactive ion beam etching facility with *in situ* metal coater

C) Magnetic characterization

1. vibrating sample magnetometer
   (magnetic field 1.6 T, room temperature)
2. vibrating sample magnetometer
   (magnetic field 5 T, temperature range 2 – 350 K)
3. vector Kerr magnetometer
   (longitudinal and transverse Kerr effect, magnetic field 1.2 T, temperature range 2 – 350 K, automated sample positioning)
4. high-field polar Kerr magnetometer
   (magnetic field 5 T, temperature range 2 – 350 K)
5. Kerr magnetometer with time resolution and setup for generation of short field pulses
6. confocal Kerr microscope (under construction)
7. two Brillouin light scattering spectrometers, computer controlled and fully automated (magnetic field 2.2 T) with stages for
   a. low temperature measurements (2 – 350 K)
   b. space-time resolved measurements for spin wave intensity mapping (resolution 50 µm, 0.83 ns)
   c. *in situ* measurements
   d. elastic measurements
8. microwave setup (up to 32 GHz) comprising a network analyzer, microwave amplifiers, modulators, pulse generators, etc.
9. magneto-transport setup (magnetic field 1.5 T, temperature range 20 – 400 K)

Chapter 5: Transfer of Technology

1. Magnetism and elastic properties

With our facilities within the Department of Physics at the University of Kaiserslautern we offer consultance and transfer of technology in the areas of thin film magnetism, magnetic film structures and devices, magnetic sensors, and in corresponding problems of metrology.

We are equipped to perform magnetic, transport, elastic and structural measurements of films and multilayer systems.

This is in detail:

- magnetometry (magnetic field up to 5 T, temperature range 2 – 400 K) using vibrating sample magnetometry, Kerr magnetometry, Brillouin light scattering spectroscopy
- magnetic anisotropies, optionally with spatial resolution
- magneto-transport properties
- test of homogeneity of magnetic parameters
- exchange stiffness constants in magnetic films
- elastic constants
- surface topography

2. Institut für Dünnschichttechnologie – Transferstelle der Universität Kaiserslautern

(Institute for Thin Film Technology – Center for Technology Transfer of the University of Kaiserslautern)

As part of technology transfer the Institute of Thin Film Technology offers among other activities

- consultance in tribological problems
- development of product specific coatings especially for medical applications
- coating of samples and small scale production series
- management for R&D-projects

The institute is located about 20 km south of Bonn in the Center for Surface Technologies (TZO) to support the economy in the northern part of the Rheinland-Pallantine State.

Address:

Institut für Dünnschichttechnologie

Maarweg 30

53619 Rheinbreitbach, Germany

Scientific director:

Prof. Dr. B. Hillebrands phone: +49 631 205 4228
e-mail: hilleb@physik.uni-kl.de

Contact:

Dr. K. Jung phone: +49 631 205 2278
e-mail: jung@physik.uni-kl.de

Representatives in Rheinbreitbach:

Lisa Kleinen phone: +49 2224 900 693
fax : +49 2224 900 694
e-mail: kleinen@physik.uni-kl.de

Dr. S. Sattel (TZO) phone: +49 2224 942 113
e-mail: rtzo@rz-online.de

Please contact us for more information.

Chapter 6: Experimental Results

A. Magnetic Tunnel Junctions

6.1 Barrier formation mechanisms in magnetic tunnel junctions prepared by ionized atom beams

B.F.P. Roos, P.A. Beck, S.O. Demokritov, and B. Hillebrands

Magnetic tunnel junctions (MTJs), comprising two ferromagnetic layers separated by a thin insulating barrier layer have gained large interest due to their potential as sensor elements. The transition from antiparallel to parallel orientation of the two layer magnetizations with increasing applied field causes a large change in the electrical resistance. The junction properties, as there are in particular the sheet resistance and the temperature dependence of the tunneling magnetoresistance (TMR), depend mainly on the insulator quality (low number of impurities and defects), the combination of barrier and electrode materials and the roughness of the electrodes. Therefore the crucial step in MTJ fabrication is the preparation of the insulating barrier. It must be made pinhole free and homogeneous over the full junction area. Al_2O_3 is mostly used as the barrier material. The barrier is usually obtained by depositing a thin metallic Al layer onto a magnetic electrode followed by an oxidation step.

Ion beam oxidation is a good candidate for producing high quality tunnel barriers. In our studies an exited electron cyclotron wave resonance controlled plasma reactor (COPRA 160, CCR Technology) [1] was used. The reactor allows one to control independently the ion current density, the ion energy and the ionization and dissociation degree of the beam. The ion energy is varied between 30 eV and 100 eV with a constant ion current flux from 0.005 up to 2 mA/cm^2 and a dissociation degree of more than 80%. The ion beam consists mainly of collimated ionized oxygen atoms (O^+) with an energy distribution width of less than ± 3 eV.

The metallic layers are deposited in a multi chamber MBE system with a base pressure less than 10^{-10} mbar using e-beam evaporation through shadow masks. The complete tunnel junction with a size of 0.25 mm^2 has the composition $Si/SiO_2/Ni_{81}Fe_{19}$ (15 nm)/Al_2O_3 (1-2 nm)/Co (1.0 nm) /Pt or Au (5 nm). The deposited Al layer was oxidized in a separate reaction chamber without breaking the vacuum.

For the online monitoring of the oxidation process, optical reflection and four-probe resistance measurements were performed *in-situ* [2]. Optical reflectivity provides easy access to the thickness of the remaining metallic Al layer due to the strong thickness dependence of the reflectivity and the large difference in the dielectric constants between metallic Al and Al_2O_3. The linear change of the reflection as a function of the layer thickness observed for Al films thinner than 2.2 nm is used for calibrating the reflection curves recorded on Al films with a constant thickness during the oxidation process. For the additional *in-situ* four-probe resistance measurements, 10 to 30 nm thick Al stripes were deposited onto Si/SiO_2 and their resistance was recorded during the oxidation process. To derive the oxidized Al layer thickness from the measured stripe resistance a calibration was performed on non-oxidized Al stripes. The calibration shows that, for the stripes with a thickness larger than 10 nm, the Fuchs-Sondheimer model [3] assuming inelastic electron scattering at the surface is applicable.

Figure 1 shows the oxidized Al thickness as a function of the ion dose determined from reflection (solid line) and resistance (dashed lines) measurements during oxidization with 30 eV and 62 eV O^+-ions. Both methods show nearly identical behaviors of the oxidation process. For low

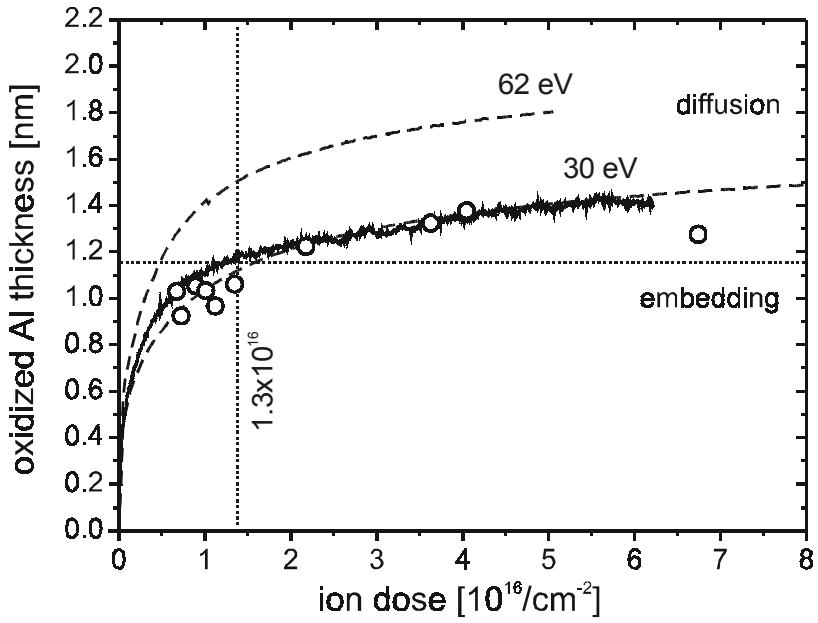

Fig. 1: Oxidized Al thickness determined by optical reflection (solid line) and resistance (dashed line) measurements during the oxidation process. The energies of the ions are indicated. The open circles (°) correspond to the effective barrier width of MTJs determined by I(V)-curves, scaled to the oxidized Al thickness.

ion doses (< $1.3 \cdot 10^{16} cm^{-2}$) the Al-film oxidizes rapidly with the rate depending on the ion energy. For higher doses the oxidation process slows down and becomes independent of the ion energy. At very high doses the oxidation saturates.

The effective barrier width shown in Fig. 1 by open circles (°) is derived from measured I(V)-curves using Brinkman's model [4] for asymmetric tunnel barriers. As it is seen from Fig. 1 the fitted values of the barrier width, scaled to the oxidized Al thickness, follow the behavior which is expected from the oxidation measurements on metallic Al.

In order to study the penetration of oxygen ions into Al, Monte-Carlo simulations were performed by using the TRIM-code [5]. The penetration of low energetic O^+-ions in metallic Al is simulated. Even if TRIM does not take into account the correct molecular interactions for low ion energies, it is applicable for single atomic target materials. Comparing the experimental data for the oxidation depth to the results of simulations, two different oxidation mechanisms are revealed: ion-embedding and diffusion. For low doses almost every incoming O^+-ion finds an incompletely oxidized Al atom as a reaction partner near its stopping point and forms directly AlO_x. An Al-AlO_x film is formed. The oxide is spread statistically in the Al film, with a higher penetration depth for higher ion energies. The very low ion dose (~ $10^{16} cm^{-2}$) needed to oxidize the first nanometer of Al is a clear indication for the high efficiency of the ion-embedding mechanism.

For higher oxygen doses the dominating oxidation mechanism is diffusion. The incoming O^+-ions find less and less non- or incompletely oxidized Al partners near their stopping points. To form a chemical bond with Al, either O or Al ions needs to diffuse through Al_2O_3. Thus, the oxidation depth is determined by the penetration depth of the ions and the diffusion. The oxidation rate in this stage is independent of the initial ion energy. Note that an electrical field effecting the diffusion is changing with growing Al_2O_3 thickness [6].

It is necessary to mention, that an ion assisted diffusion mechanism is discussed in the literature [7, 8]. Here the collisions of the incoming ions produce vacancies or defects in the material, which enhance the diffusion coefficients for oxygen and metallic atoms in the oxide. To check the importance of this mechanism the following experiment was carried out: the plasma reactor was filled with inert Ar, producing the same ion beam current as in our standard experimental conditions for ion oxidation, whereas non-ionized oxygen with the same flow rate as for the

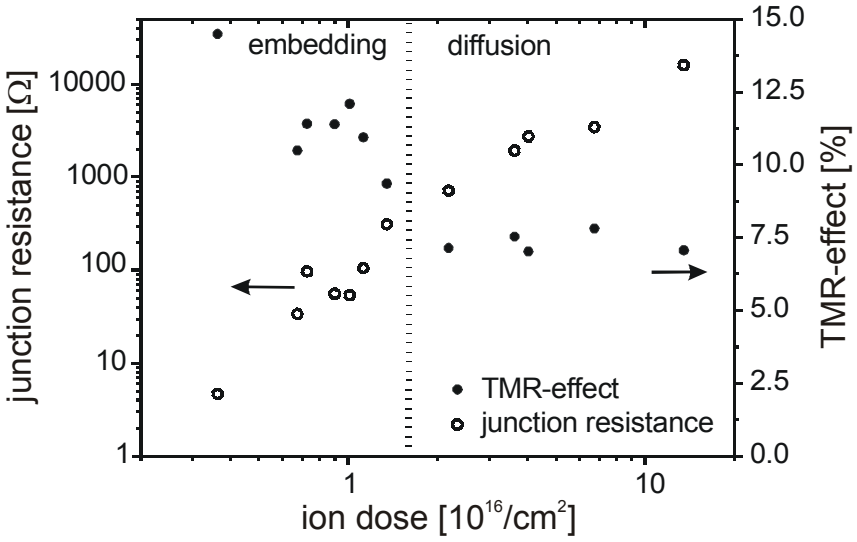

Fig. 2: Junction resistance (°) and TMR values (•) as a function of the oxygen ion dose.

standard experiment was let into the oxidation chamber. Thus the oxidizing Al film was simultaneously effected by the inert ion beam and the oxygen atmosphere. The obtained oxidation depth of about 0.6 nm is higher than the value observed in thermal oxidation, but it is still much smaller than the oxidation depth determined by ion-embedding followed by diffusion.

Figure 2 shows the junction resistance and the TMR-effect for different MTJs, all prepared using 30-eV-ions with an initial Al layer of 1.8 nm thickness and at various ion doses. The junction resistance is strongly increasing with the ion dose. The barrier parameters derived [9] from I(V) measurements show an increasing barrier width (see Fig. 1) with a nearly constant barrier height of about 2.1 eV. This fact corroborates the high quality of the obtained barriers.

The TMR-values measured at low applied voltages reach 14% for low ion doses, and they are reduced to about 7.5% at high doses. The decrease takes place at about the dose where the transition from ion-embedding as the dominating oxidation mechanism to diffusion occurs. After the transition to diffusion no further TMR reduction occurs. The origin of this behavior is not clear yet, but it might be connected with structural effects in the formed Al_2O_3-layer. In fact, the ion-embedding oxidation should occur more or less homogeneously over the Al-layer, whereas the diffusion process would take place mainly along the crystallite grain boundaries.

The work was supported by the Deutsche Forschungsgemeinschaft. The authors would like to thank D. Ozkaya and M. Rickart for performing TEM and STM measurements, respectively. Technical assistance of CCR GmbH and discussions with W. Maas are gratefully acknowledged.

References

[1] M. Weiler, K. Lang, E. Li, J. Robertson, Appl. Phys. Lett. **72**, 1314 (1998).
[2] B.F.P. Roos, P A. Beck, S.O. Demokritov, B. Hillebrands, D. Ozkaya, J. Appl. Phys. **89**, 6656 (2001).
[3] K. Fuchs, Proc. Camb. Phil. Soc. **34**, 100 (1938); E.H. Sondheimer, Advan. Phys. **1**, 1 (1952).
[4] W.F. Brinkman, R.C. Dynes, J.M. Rowell, J. Appl. Phys. **41**, 1915 (1970).
[5] SRIM 2000 code, J.F. Ziegler, J.P. Biersack, U. Littmark, *The Stopping and Range of Ions in Solids*, Pergamon, New York, Oxford (1985).
[6] A.T. Fromhold, *Theory of metal oxidation*, Volume I-*Fundamentals*, North-Holland, Amsterdam (1976).
[7] A.H. Eltoukhy, J.E. Greene, J. Appl. Phys. **51**, 4444 (1980).
[8] H. Metiu, A.E. DePristo, J. Chem. Phys. **91**, 2735 (1989).
[9] E. Girgis, H. Boeve, J. De Boeck, J. Schelten, P. Rottlander, H. Kohlstedt, P. Grünberg, J. Mag. Mag. Mat. **222**, 133 (2000).

6.2 Surface smoothing by low energy ion bombardment

S.O. Demokritov, B.F.P. Roos, M. Rickart, and B. Hillebrands

The preparation of perfect smooth surfaces is a superior goal of many thin film technologies. There are several ways to approach this goal. One route is epitaxial layer-by-layer growth of the film on an appropriate substrate. A second route is to smooth the surface after the growth. If thin films and microscopic roughness on the nanometer scale are considered there are very few ways to smooth the surface, since standard techniques (mechanical and chemical polishing) are not appropriate due to obvious reasons. The only ways to improve the nano-roughness are to anneal the surface in ultra high vacuum (UHV) [1] or in special atmosphere [2], or to bombard the surface with different species. Middle energy electrons were used to smooth surfaces of metallic Cr [3] and Co [4] films. Recently it was reported that bombardment of different films in magnetic tunnel junction stacks with gas clusters may cause an essential improvement of their tunnel magnetoresistance characteristics [5]. Here we report on the application of low energy ionized atoms. As an example, smoothing of an insulating surface (MgO(001)) and a metallic surface (Fe(001)) are discussed. We show that in the case of MgO the ion beam treatment not only smoothes the surface, but also removes carbon contaminations [6].

The surface of commercially available MgO substrates (10×10 mm^2) is contaminated by water and carbon and it is relatively rough. To prepare clean MgO(001) surfaces, the samples are pre-heated in UHV at a moderate temperature of 150^{o}C for 30 min to remove water from the surface and then treated with an atomic oxygen ion beam at room temperature, as described below. Metallic Fe(001) films with a thickness of 5 nm are grown on MgO in UHV at 200^{o}C using an electron beam evaporator with a deposition rate of about 0.01 nm/s. To improve the roughness of the Fe-films they are first annealed at 400^{o}C and then treated with an argon ion beam. The surface topography is studied with a commercial Park Scientific Instruments Autoprobe VP 2 UHV device, which is a combined atomic force (AFM) and scanning tunneling microscope (STM). AFM with a typical lateral resolution of 3 nm is used for investigations of insulating MgO.

The ion beam treatment is performed using a novel type of an excited electron cyclotron wave

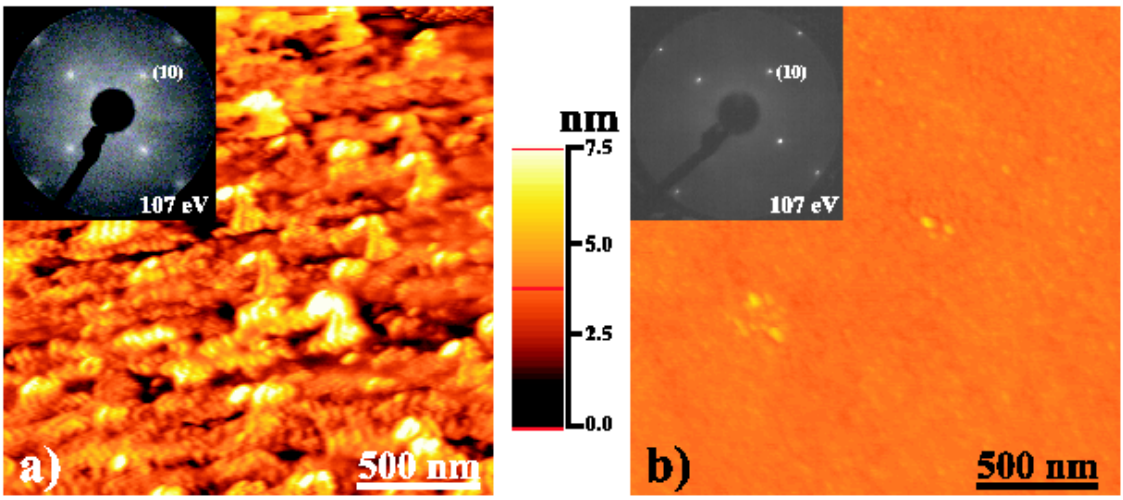

Fig. 1: AFM images of a MgO surface, a) before the treatment, RMS = 0.7 nm , b) after the ion beam treatment, RMS 0.1 nm. The insets show the corresponding LEED patterns at an energy of 107 eV.

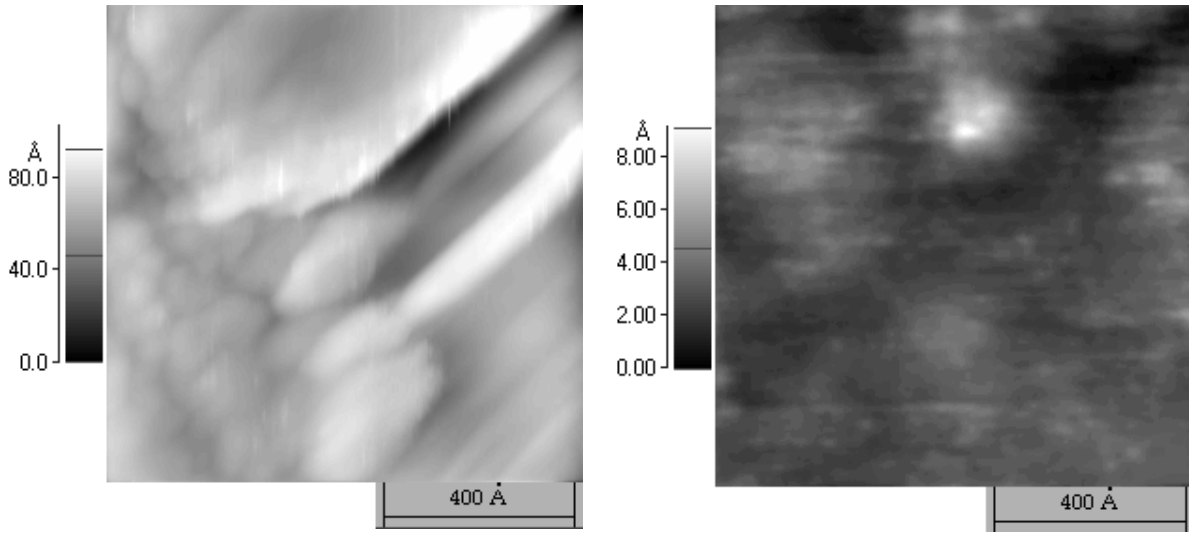

Fig. 2: STM images of an Fe(001) surface, a) before the treatment, RMS = 2.5 nm , b) after the ion beam treatment, RMS 0.175 nm. Note the change in the gray scales between both panels.

resonance (ECWR) controlled plasma reactor (COPRA 160, CCR Technology). The reactor is a high frequency, low pressure plasma source with an inductive excitation. A crucial advantage of the source is its ability to produce low energy (20-100 eV) ion beams. The ion beam is automatically neutralized by a corresponding electron current, thus minimizing charging effects on the substrate. The filament free design of the source allows one to perform the ion treatment without contamination of the surface by the filament material. The source produces an oxygen beam with a dissociation degree of up to 80 %. The ion current density is chosen to be 0.1 mA/cm^2 and a process time of 2 min, providing an ion dose of 6×10^{16} ions/cm^2. Ions with the nominal energy of 30–50 eV and an energy distribution width below 10 % of the nominal energy are used for the ion beam treatment. The ion current density and the ion energy are monitored using a Faraday cup. A detailed technical description of the source can be found elsewhere [7].

Figure 1 shows AFM topography images of a MgO(001) sample before and after the ion beam treatment with 35 eV O^+-ions. The measured root mean square (RMS) roughness before the treatment is 0.7 nm. As seen in Fig. 1 the ion-beam treated surface is much smoother showing a measured RMS roughness as small as about 0.1 nm. Note here, that due to averaging over the finite lateral resolution of the AFM (typically 3 nm) monatomic steps on MgO cannot be resolved. Auger electron spectroscopy (not shown) indicates that the carbon contamination with the effective thickness of 0.4 ML is completely removed after the bombardment.

Similar results are also obtained for smoothening of Fe(001) films. Unlike MgO, the bombardment of the Fe film is performed with Ar^+-ions instead of oxygen to avoid oxidation of Fe. Figure 2 presents STM images of Fe the surface before and after the ion beam treatment with 45 eV Ar^+-ions. The essential smoothing of the surface is obvious from a comparison of Figs. 2a and 2b. The measured RMS value of the untreated films is 2.5 nm, while that of the treated film is below 0.18 nm.

It is necessary to note that the energy of the ions is a very important parameter of the treatment. For the used energies the sputtering rate is found to be negligible.

Support by the Deutsche Forschungsgemeinschaft is gratefully acknowledged.

References

[1] S.M. Jordan, J.F. Lawler, R. Schad, H. van Kempen, J. Appl. Phys. **84** 1499 (1998).
[2] L.W. Guo, T. Hanada, H.J. Ko, Y.F. Chen, H. Makino, T. Yao, Surf. Sci. **445**, 151 (2000).
[3] S.O. Demokritov, J.A. Wolf, P. Grünberg, Appl. Phys. Lett. **63**, 2147 (1993).
[4] R. Allenspach, A. Bischof, U. Dürig, P. Gütter, Appl. Phys. Lett. **73**, 3598 (1998).
[5] J.J. Sun, K. Shimazawa, N. Kasahara, K. Sato, S. Saruki, S. Araki, M. Matsuzaki, , J. Appl. Phys. **89**, 6653 (2001).
[6] M. Rickart, B.F.P. Roos, T. Mewes, J. Jorzick, S.O. Demokritov, B. Hillebrands, Surf. Sci. in press.
[7] M. Weiler, K. Lang, E. Li, J. Robertson, Appl. Phys. Lett. **72**, 1314 (1998).

B. Dynamic Magnetic Phenomena

6.3 Spin wave wells in non-ellipsoidal micrometer size magnetic stripes

S.O. Demokritov, J. Jorzick, and B. Hillebrands[1]

We report on the study of dynamic excitations in long, thin magnetic stripes magnetized in the stripe plane and perpendicular to their axes. Due to demagnetizing effects, the internal field of these stripes is intrinsically inhomogeneous. A novel, strongly spatially localized spin wave mode is observed. This mode appears near those edges of the stripes that are perpendicular to the applied magnetic field. The spatial localization takes place due to the high inhomogeneity of the internal field in these regions, which creates a potential well for the spin waves.

The investigated samples were prepared from $d = 30 - 35$ nm thick permalloy ($Ni_{80}Fe_{20}$) films, which were grown by thermal evaporation on chemically cleaned Si(111) substrates at room temperature in UHV. Patterning was performed by means of e-beam lithography, reactive ion etching and argon ion etching using photoresist/germanium layers as intermediate masks. Stripe arrays with a width of $w = 1$ μm, a length of 90 μm, and a distance between the stripes of 0.3 – 1 μm were prepared. Thermally excited spin waves were investigated in backscattering geometry using a Brillouin light scattering (BLS) spectrometer described in [1].

It has been recently shown [2, 3] that the intensity of light inelastically scattered from laterally confined spin wave modes for a given transferred wavevector Q is proportional to the Fourier component of the mode profile squared, m_Q^2, of the dynamic magnetization. Thus, by measuring the BLS intensity as a function of Q one can derive the spatial profile $m(r)$. The interval in Q, in which a significant BLS intensity is observed, is inversely proportional to the confinement width of the mode in the real space, $\Delta Q \approx 2\pi / \Delta r$.

For reference, Fig 1a shows the dispersion of spin wave modes in the Damon-Eshbach (DE) geometry, in which the external field $\mathbf{H}_e = 500$ Oe is perpendicular to $\mathbf{Q}$ and is along the stripe axis. Demagnetizing effects are negligible in this geometry. The results clearly demonstrates the lateral quantization of the DE spin waves, resembling a typical "staircase"-dispersion [2, 4]. The interval of the observation of each mode in the Q-space $\Delta Q \approx (0.8-1)\cdot 10^5\, cm^{-1}$ is in agreement with the width of the stripe $w = 1$ μm, giving $2\pi / w = 0.63 \cdot 10^5\, cm^{-1}$. The frequency of the perpendicular standing spin wave mode (PSSW) coincides with that of the PSSW mode for the unpatterned film and corresponds to an internal field of $H = H_e = 500$ Oe, thus corroborating negligible demagnetizing effects in the stripes magnetized along their long axes. The frequencies of the observed modes are calculated as described below. The results of the calculations are shown in Fig. 1a by horizontal solid lines.

Fig. 1b shows the results for $\mathbf{H}_e$ perpendicular to the stripe axis, i.e., demagnetizing effects are large. The dispersion, obtained in the so-called backward volume magnetostatic spin wave (BWVMS) geometry ($\mathbf{H}_e \parallel \mathbf{Q}$), differs completely from that shown in Fig. 1a. First, the PSSW mode is splitted into two modes, with frequencies corresponding to internal fields of $H = 300$ Oe and $H = 0$ Oe, respectively. This confirms the fact, that in such a geometry the internal field is determined by an essential demagnetizing effect in the center region of the stripe, and can be zero near the edges, where the external field enters and exits the stripe [5]. Second, a broad peak is seen in the spectra in the frequency range 5.5 – 7.5 GHz. The shape of the peak varies with Q,

[1] In collaboration with M. Bailleul and C. Fermon, CEA Saclay, France; and K. Guslienko and A.N. Slavin, Oakland University, USA.

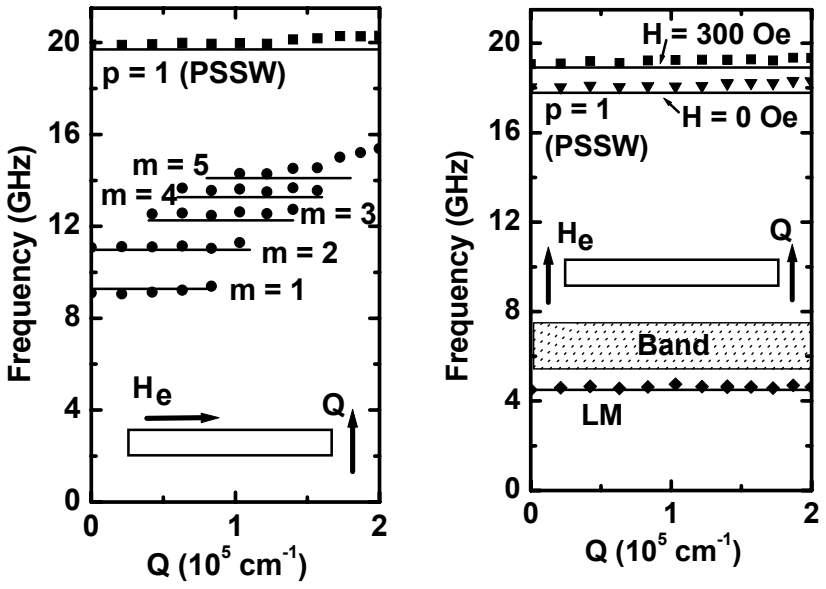

Fig. 1: Spin wave dispersion of the wire array measured at $H_e = 500$ Oe for (a) the DE-geometry, (b) the BWVMS-geometry. The solid lines represent the results of calculation.

thus indicating different contributions of unresolved modes to the scattering cross section at different Q. Third, a separate, low frequency, dispersionless mode with a frequency near 4.6 GHz (indicated as "LM" in Fig. 1b) is observed over the entire accessible wavevector range $Q_{\max} \approx 2.5 \cdot 10^5 cm^{-1}$ with almost constant intensity. This is a direct confirmation of a strong lateral localization of the mode within a region with the width $\Delta r < 2\pi / Q_{\max} = 0.25$ μm. From the low frequency of the mode one can conclude that it is localized near the edges of the elements, since these are the field-free regions [5, 6].

A quantitative analytical description of the spin wave modes observed in the stripes can be found elsewhere [7]. We will illustrate the main ideas in the following. The profile of the internal field H over the stripe is shown in the inset of Fig. 2. For $H > 0$ the magnetization is parallel to $\mathbf{H}_e$. Near the edges, however, regions with $H = 0$ and regions with continuously rotating magnetization are formed. Since the rotation of the static magnetization dramatically changes the dispersion of spin waves, regions with zero internal field will reflect spin waves propagating from the middle of the stripe towards these regions. On the other hand, a spin wave of a given frequency propagating in an inhomogeneous field might encounter a turning point even if the magnetization is uniform. In fact, for large enough values of the internal field there are no allowed real values of Q, consistent with the spin wave dispersion [8]. Thus, the inhomogeneous internal magnetic field creates a potential well with two turning points for propagating spin waves. This well can severely restrict the spatial region of spin wave existence. Similar to the potential well in quantum mechanics, the conditions determining the frequencies ν_r of possible spin wave states in the well created by the inhomogeneous internal field are determined by the equation: $\int Q(H(z),\nu)dz = r\pi$, where $r = 1,2,3,...$ and $Q(H(z),\nu)$ is found from the spin wave dispersion. The calculated dispersion curves for spin wave with $\mathbf{Q} \parallel \mathbf{H}$ are presented in Fig. 2. Different curves correspond to different constant values of the field as indicated. A solid horizontal line presenting the frequency of the lowest spin wave mode $\nu_1 = 4.5$ GHz obtained from the integral equation for $r = 1$ is in a good agreement with the experiment. It is seen from Fig. 2, that for $H > 237$ Oe there are no real values of Q for which the frequency $\nu_1 = 4.5$ GHz lies in the spectrum of spin waves. Therefore, the lowest mode can only exist in the spatial regions in the magnetic stripe where the internal field satisfies the condition $0 \text{ Oe} < H < 237$ Oe. The corresponding turning points are indicated in the inset in Fig. 2 by the vertical dash lines. Thus, the lowest mode is localized in the narrow region Δz near the lateral edges of the stripe where

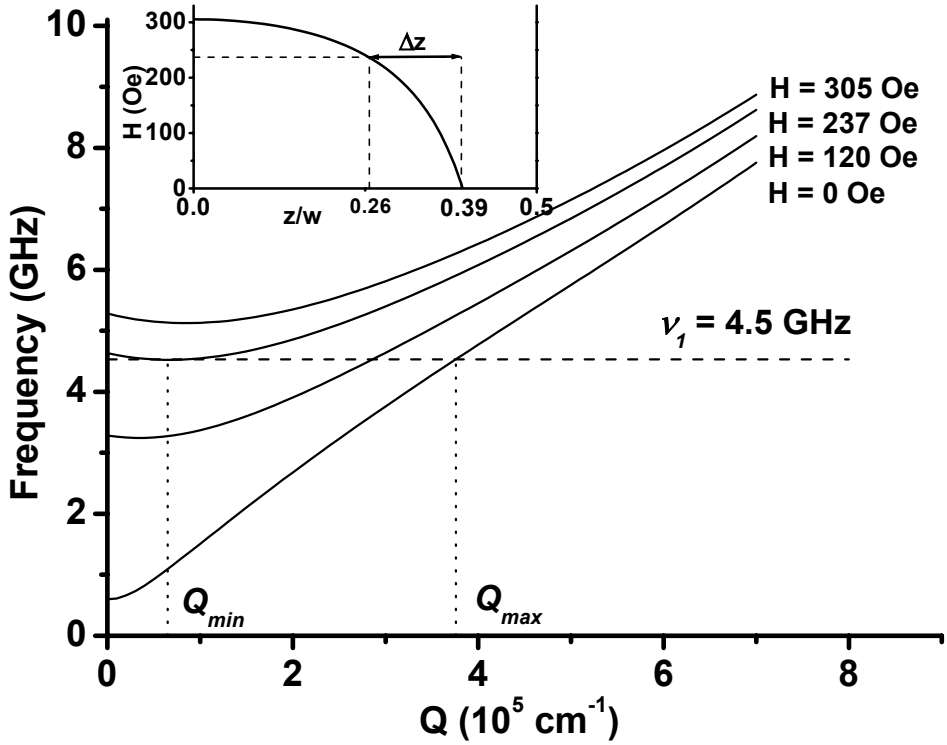

Fig. 2: Dispersion of plane spin waves in the BWVMS-geometry at constant internal fields as indicated. Inset: the profile of the internal field in a wire. Δz shows the region of the lowest mode localization**.**

$0.26 < |z/w| < 0.39$. The mode is composed of plane waves with $Q_{min} < Q < Q_{max}$, as indicated in Fig. 2.

Finally, we would like to point out a very peculiar feature of this localized mode. Being the lowest mode in the spectrum, it is in fact an exchange-dominated mode, since the dispersion of the contributing plane waves is mainly determined by the exchange interaction.

Support by the Deutsche Forschungsgemeinschaft and the Stiftung für Innovation of the state of Rhineland Palatinate is gratefully acknowledged.

References

[1] B. Hillebrands, Rev. Sci. Instr. **70**, 1589 (1999).
[2] J. Jorzick, S.O. Demokritov, B. Bartenlian, C. Chappert, F. Rousseaux, A.N. Slavin, B. Hillebrands, Phys. Rev. B **60**, 15194 (1999).
[3] J.F. Cochran, J. Mag. Mag. Mat. **212**, 40 (2000).
[4] C. Mathieu, J. Jorzick, A. Frank, S.O. Demokritov, B. Hillebrands, A.N. Slavin, B. Bartenlian, C. Chappert, D. Decanini, F. Rousseaux, E. Cambril, Phys. Rev. Lett. **81**, 3968 (1998).
[5] P. Bryant and H. Suhl, Appl. Phys. Lett. **54**, 2224 (1989).
[6] R.I. Joseph, E. Schloemann, J. Appl. Phys. **36**, 1679 (1965).
[7] J. Jorzick, S.O. Demokritov, B.Hillebrands, M. Bailleul , C. Fermon, K. Guslienko, A.N. Slavin, D.V. Berkov, and N.L. Gorn, *Spin wave wells in non-ellipsoidal micrometer size magnetic elements*, submitted to Phys. Rev. Lett.
[8] E. Schlomann, R.I. Joseph, J. Appl. Phys. **35**, 167 (1964).

6.4 Spin wave localization in micrometer size magnetic rectangular elements

S.O. Demokritov, J. Jorzick, and B. Hillebrands[1]

In the previous contribution (Section 6.3) we discussed the observation of a novel, strongly spatially localized spin wave mode in long magnetic stripes. Here we report a theoretical and experimental study of a similar localized mode in micrometer size rectangular elements. The spatial localization of the mode also takes place due to the high inhomogeneity of the internal field near the edges of the elements. Unlike to the stripes, however, the mode is observed in all in-plane orientations of the applied field, since for a rectangular element one can always find edges of the element, which are not parallel to the applied magnetic field.

The investigated samples were prepared from $d = 33$ nm thick permalloy ($Ni_{80}Fe_{20}$) films, which were grown by thermal evaporation on chemically cleaned Si(111) substrates at room temperature in UHV. Similar to the stripe samples patterning of the rectangular elements was performed by means of e-beam lithography, reactive ion etching and argon ion etching using germanium layers as intermediate masks. The elements have lateral dimensions of $1\times(1–2)$ μm^2. The spacing $\delta = 0.1 – 1$ μm between the elements was always chosen the same in both lateral directions. The elements were arranged in arrays with dimensions of 500×500 μm^2. The high quality of the patterning process is evident from Fig. 1a, where a scanning force microscope image of an array is shown.

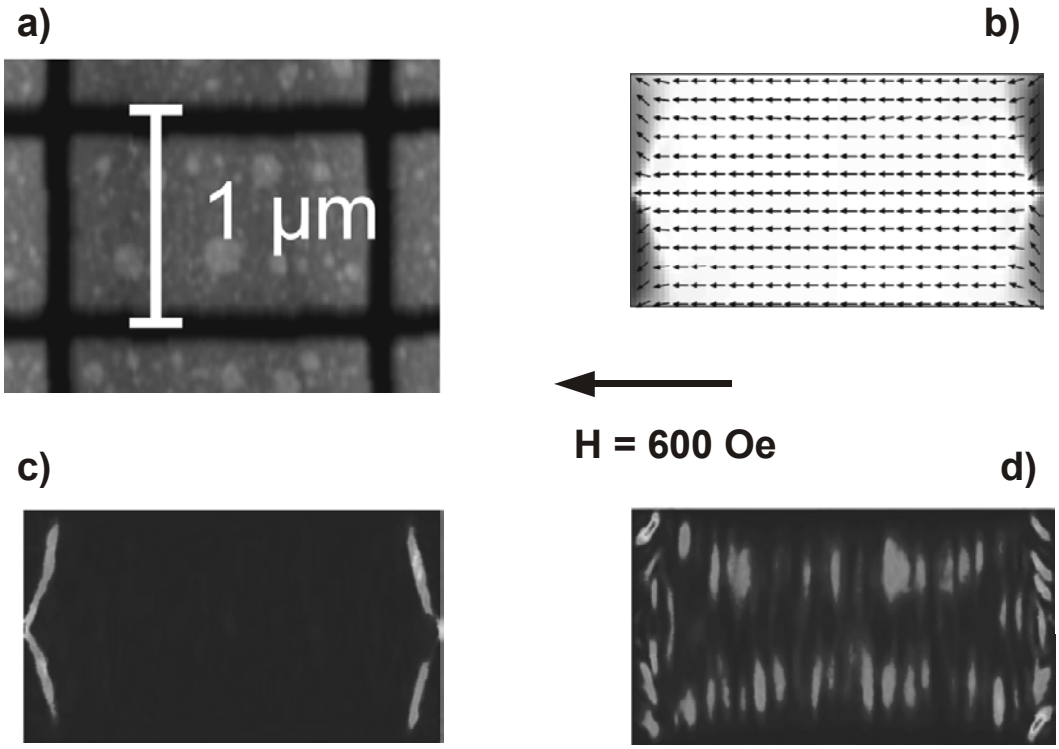

Fig. 1: a) AFM-image of rectangular elements; b) calculated distribution of static magnetization in an element; c) mode profile of a low frequency spin wave mode with $\nu = 5.3$ GHz. Note the mode localization near the edges; d) mode profile of a spin wave mode with $\nu = 12.2$ GHz**.**

[1] In collaboration with M. Bailleul and C. Fermon , CEA Saclay, France; K. Guslienko and A.N. Slavin, Oakland University, USA; and D.V. Berkov and N.L. Gorn, Innovent Jena, Germany.

Studies of thermally excited spin waves using a Brillouin light scattering spectrometer have shown the existence of a localized, low frequency mode in the rectangular elements. For example, the frequency of the mode for the array of rectangular elements with the lateral sizes $1\times1.75\ \mu m^2$ and the distance between the elements $\delta = 0.2\ \mu m$ at the external magnetic field $H_e = 600$ Oe applied along the long edge of the elements is 5.3 GHz.

Since the analytical approach presented in the preceding Section is essentially a one-dimensional one, it cannot be applied directly to rectangular elements. Instead, micromagnetic simulations of the equilibrium thermodynamic properties of magnetic excitations in such elements were performed. The method is based on the Langevin-dynamics approach [1]. The time evolution of the magnetization distribution of the element discretized into cells with magnetic moments $\boldsymbol{\mu}_i$ is simulated using the Landau-Lifshitz-Gilbert (LLG) equation. The effective field $\mathbf{H}_i^{eff}$ acting on the *i*-th moment includes a deterministic part $\mathbf{H}_i^{det}$ and a fluctuating part $\mathbf{H}_i^{fl}$. The former comprises the external field and the effective fields due to exchange and dipolar interactions between different cell moments. The second effective field, simulating thermal fluctuations, has Cartesian components with well known statistical properties [2]. The LLG-equation with a fluctuating field was considered in the Stratonovich interpretation [3], and has been solved using the improved version of the Bulirsch-Stoer method specially adapted and optimized for solving stochastic differential equations.

The starting state (Fig. 1b) for the simulation is obtained by solving the LLG equation without any fluctuating fields. Next, the field $\mathbf{H}_i^{fl}$ is turned on. After the thermodynamic equilibrium state of the system is reached (i.e., the system energy did not exhibit any systematic change with time), the values of all cell moments obtained during the simulation are recorded as functions of time. Afterwards, using Fourier analysis, the oscillation spectrum of the total magnetic moment of the element is obtained. In the frequency interval 3 – 20 GHz this Fourier spectrum demonstrates several maxima. The Fourier components of each cell magnetization $\boldsymbol{\mu}_{i,\omega}$ corresponding to these maxima are calculated and squared, to compare them with the measured spin wave intensities. As an example, the spatial distributions of spin wave modes with the frequencies $\nu = 5.3$ GHz and $\nu = 12.2$ GHz are presented in Figs. 1c and 1d. It is clear from Fig. 1c that the low-frequency mode is strongly localized in the narrow regions near the edges of the elements that are perpendicular to the applied field in accordance with the experiment and with the result of the analytical analysis performed for the stripes. In contrast, the mode with $\nu = 12.2$ GHz shown in Fig. 1d is not localized, but is a result of a complicated two-dimensional lateral quantization of spin waves in the element.

Finally, we have demonstrated that the eigenmode spectrum of magnetic rectangular elements includes a low frequency, spatially localized spin wave mode of exchange nature. Similar to the stripes, the localization of the mode is caused by the inhomogeneity of the internal field. These modes must be taken into account for yielding a better understanding of, e.g., the fast magnetic switching properties in magnetic memory elements.

Support by the Deutsche Forschungsgemeinschaft and the Stiftung für Innovation of the state of Rhineland Palatinate is gratefully acknowledged.

References

[1] J.L. Garcia-Palacios, F.J. Lazaro, Phys. Rev. B **58**, 14937 (1998).
[2] W.F. Brown, Jr., Phys. Rev. **130**, 1677 (1963).
[3] P.E. Kloeden, E. Platen, *Numerical Solution of Stochastic Differential Equations*, Springer, Berlin, 1995.

6.5 Excitation and propagation of spin wave packets in thin garnet films by a short field pulse studied by space- and time-resolved magneto-optic Kerr effect magnetometry

M. Bauer, R. Lopusnik, J. Fassbender, and B. Hillebrands

Linear and nonlinear wave phenomena (e.g. self-focusing, solitons, bullets, etc.) are important subjects in both basic research and applications. Nonlinear wave effects have been experimentally observed in a large number of different physical systems. Specifically, for investigations of excitation and propagation of wave packets in linear as well as in nonlinear media, thin magnetic garnet films with very low damping have proven to be a nearly perfect laboratory test system. By variation of the propagation direction and wavelength of the spin waves and/or the strength and direction of the applied magnetic field a large parameter space (e.g., group- and phase velocity, dispersion, diffraction, non-linearity, damping) is accessible with the same sample. Recently, we have developed an advanced Brillouin light scattering (TRBLS) setup, which allows one to map the spatial spin wave intensity distribution across the sample with time resolution [1].

It is also advantageous to test spin wave excitations by a short field pulse and the propagation by an independent method, working directly on the time scale, which is the subject of this report. Utilizing a newly developed space- and time-resolved magneto-optic Kerr effect vector magnetometer setup [2] the excitation and propagation of spin wave packets in a thin bismuth substituted lutetium iron garnet (BiLuIG, $Bi_{0.96}Lu_{2.04}Fe_5O_{12}$) film grown on a gadolinium gallium garnet substrate have been investigated [3].

Figure 1 shows the experimental setup. A 8 mm long, 2 mm wide and 1.5 µm thin BiLuIG film was saturated by a static magnetic field of H_{stat} = 40 Oe along the *y*-direction, the short dimension of the film. A narrow, 50 µm wide microstrip transmission line was used for the pulse excitation. Magnetic field pulses of about 3 ns duration, 100 ps rise time, 200 ps fall time and $H_{pulse} \approx 1$ Oe field amplitude were applied along the *x*-direction with a repetition rate of 100 kHz. The magneto-optic (MO) response of the generated spin waves was measured with an angle of light incidence of 55 deg.

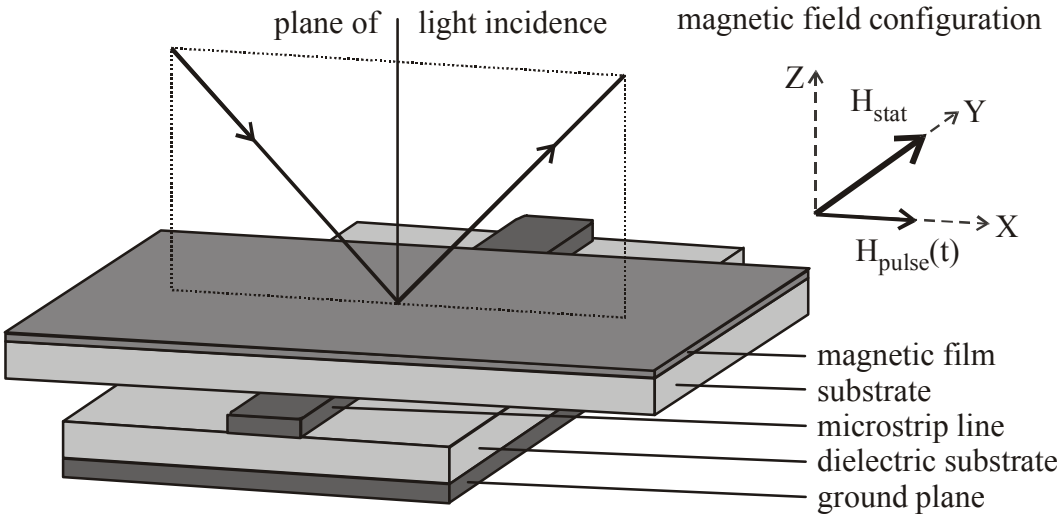

Fig. 1: Sample geometry, plane of light incidence, and magnetic field configuration used in the experiment.

Figure 2 shows the time evolution of the excitation and propagation of spin wave packets in a grayscale representation of the MO signal at different times t. At $t = 1$ ns the pulse excitation starts. For $t = 1.4$ ns the maximum deflection of the magnetization is reached on the microstrip

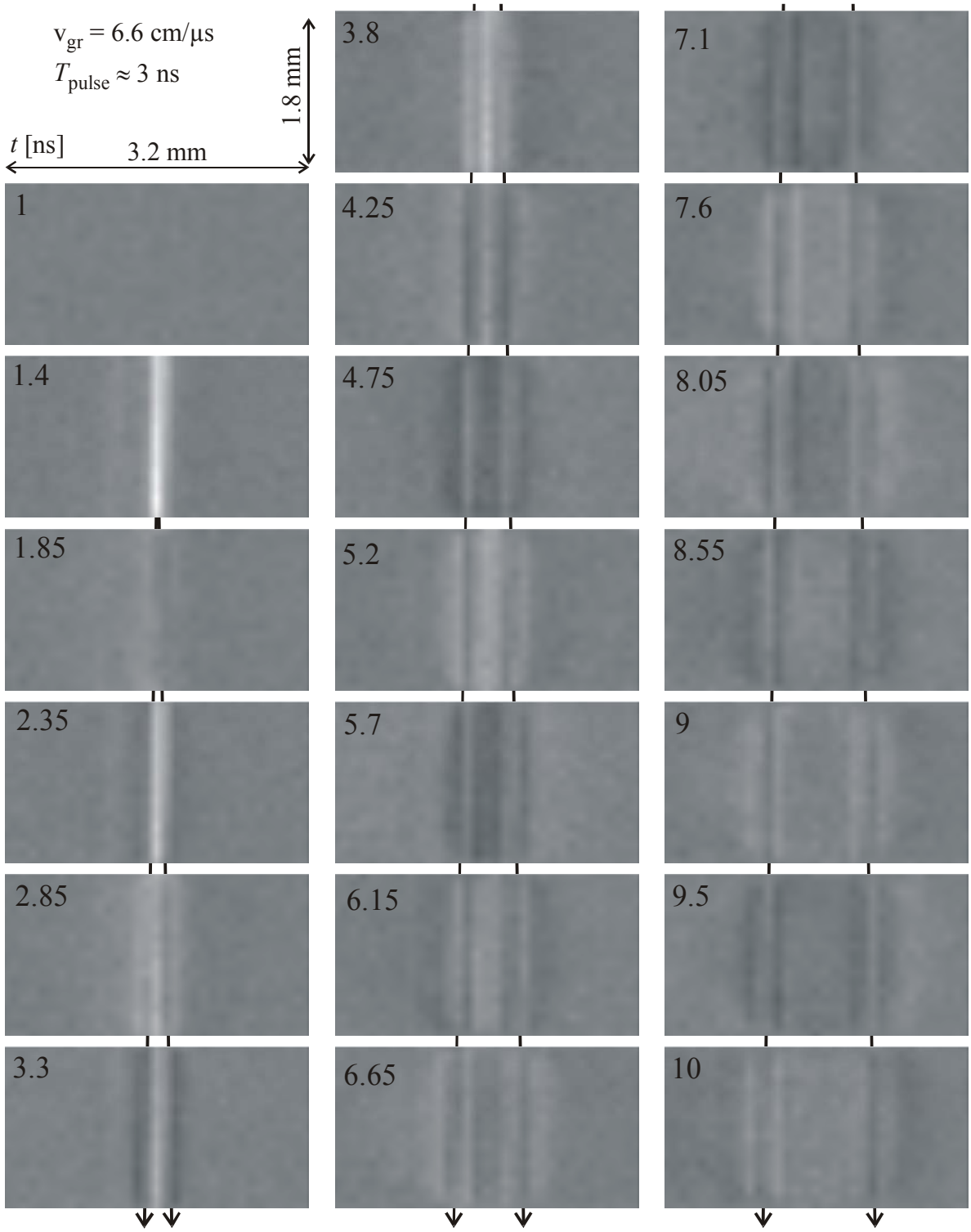

Fig. 2: Time evolution of the excitation and propagation of spin wave packets. Shown here is a sequence of the mapped magneto-optic signal in a grayscale representation at different times t. Bright (dark) areas indicate a positive (negative) deflection of the magnetization from the equilibrium direction. The field pulses of ≈3 ns duration start at $t = 1$ ns. The arrows indicate the propagation of the wave packets with a group velocity of $v_{gr} = 6.6$ cm/µs.

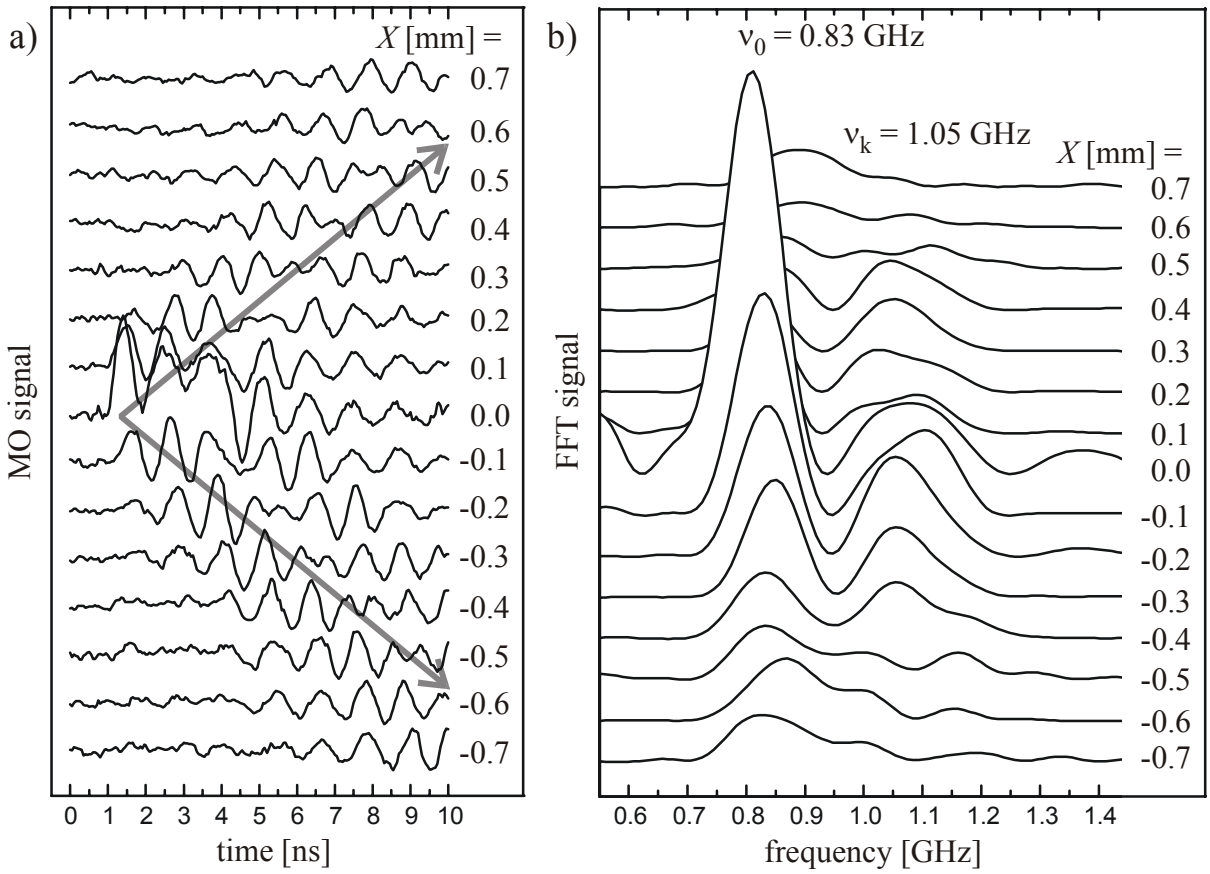

Fig. 3: Response of the MO signal in time (a) and frequency space (b) for different distances to the microstrip transmission line. The frequency of the uniform and the propagating spin wave mode were determined to be $\nu_0 = 0.83$ GHz and $\nu_k = 1.05$ GHz, respectively.

indicated by the white strip. Two spin wave packets begin to form on each side of the strip, and they propagate from the localized field region near the microstrip away to both sides. The propagation of the spin wave packets is clearly noticeable. From the data a group velocity of $v_{gr} = 6.6$ cm/µs is determined.

In Fig. 3 the response of the MO signal is shown as a function of time (a) and frequency (b) for different distances to the microstrip. The frequency spectra (b) are calculated from the time response data (a) by means of a fast Fourier transformation. At the microstrip position two peaks in the frequency spectra are clearly visible. They have been identified as the uniform precession mode (index '0') and the propagating spin wave mode (index 'k') with frequencies of $\nu_0 = 0.83$ GHz and $\nu_k = 1.05$ GHz, respectively. Note that, first, the intensity of the uniform precession mode decreases very rapidly in *x*-direction. Thus this mode is localized near the microstrip. Second, the intensity of the propagating mode is nearly constant. This mode carries energy away from the microstrip area. In Fig. 3b the intensity of this mode breaks down because the MO response in a too short time range of 10 ns only has been recorded. During this time the spin wave packet did not pass completely the points at large distances form the microstrip.

Figure 4 shows the MO signal averaged over the *y*-direction as a function of the distance *x* from the microstrip for different times. The dotted arrows indicate points with constant phase. From their slope the phase velocity has been determined to $v_{ph} = 34$ cm/µs. The distance between consecutive arrows in *x*-direction at a constant time corresponds to a wavelength of $\lambda = 0.03$ cm and a wave vector of $k_x = 210$ cm^{-1}, respectively. The gray arrow on the left represents the center of gravity of the spin wave packet. It moves with the group velocity, which is much slower than

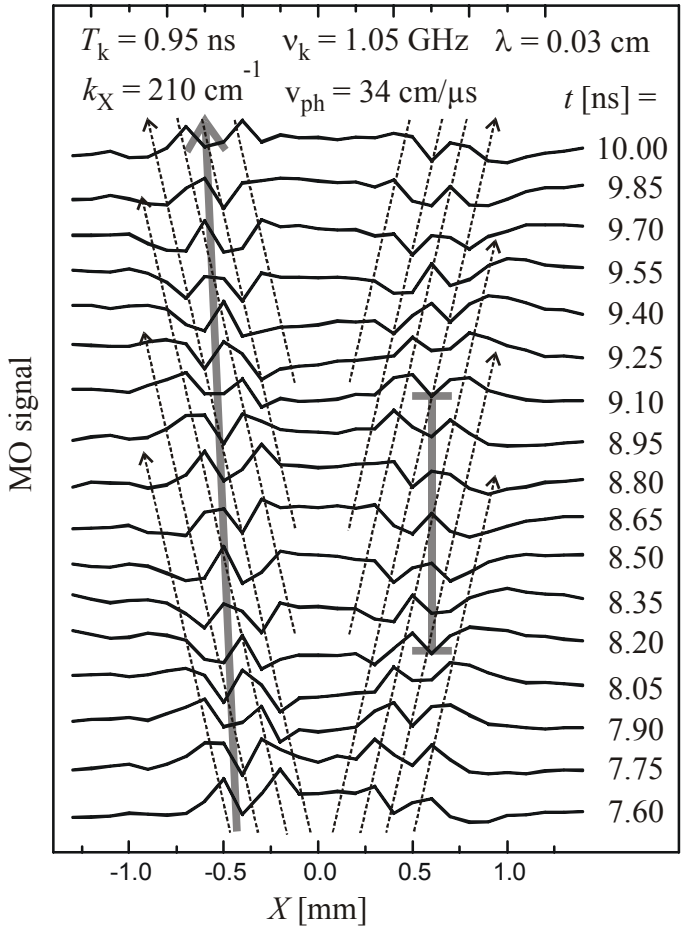

Fig. 4: Determination of phase velocity v_{ph} = 34 cm/µs, wave length λ = 0.03 cm, wave vector k_X = 210 cm^{-1}, precession period T_k = 0.95 ns, and frequency ν_k = 1.05 GHz of the propagating spin wave mode.

the phase velocity. The marker on the right is used to determine the carrier precession period to T_k = 0.95 ns and the frequency to ν_k = 1.05 GHz.

Finally, the measured parameters presented above are compared to a simple model calculation. In the present case the propagating spin wave mode is a magneto-static surface wave (MSSW) mode, since both the direction of the magnetic field and the wave vector lie perpendicular to each other in the film plane. From the dispersion relation of the MSSW mode

$$\omega_k = |\gamma| \sqrt{H_{stat}\left(H_{stat} + 4\pi M_S\right) + \left(2\pi M_S\right)^2 \left(1 - \exp\left(-2k_X d\right)\right)} \tag{1}$$

the phase and group velocities are calculated as

$$v_{gr} = \left.\frac{\partial \omega_k}{\partial k_X}\right|_{k_X} = 6.3\,\mathrm{cm/\mu s} \tag{2}$$

and

$$v_{ph} = \frac{\omega_k}{k_X} = 31\,\mathrm{cm/\mu s}\,, \tag{3}$$

respectively. $|\gamma|$ = 0.0176 (Oe ns)$^{-1}$ denotes the gyromagnetic ratio, H_{stat} = 40 Oe is the applied static magnetic field, k_X = 210 cm^{-1} is the wave vector and d = 1.5 µm is the film thickness.

	experiment	model
frequency of the uniform mode	$\nu_0 = 0.83$ GHz	$\nu_0 = 0.79$ GHz
frequency of the propagating mode	$\nu_k = 1.05$ GHz	$\nu_k = 1.04$ GHz
phase velocity	$v_{ph} = 34$ cm/µs	$v_{ph} = 31$ cm/µs
group velocity	$v_{gr} = 6.6$ cm/µs	$v_{gr} = 6.3$ cm/µs

Tab. 1: Comparison between measured and calculated values.

Only the saturation magnetization has been adjusted to $4\pi M_S = 1950$ Oe. Table 1 shows a comparison between the measured and calculated values. Within the limits of this model there is a good agreement between the measured and calculated values.

The presented method has several advantages compared to measurements with conventional microwave techniques utilizing miniaturized pickup coils. The lateral resolution is better and it is practically free of cross talk, i.e., a direct electromagnetic coupling between the microstrip and a pickup coil. Compared to space- and time-resolved Brillouin light scattering, where the intensity is measured, the phase of the spin waves is directly accessible. The time resolution is improved by two orders of magnitude. Furthermore all three components of the magnetization can be measured [4]. On the other hand, a much longer acquisition time and the loss of direct wave vector selectivity must be taken into account.

Work supported by the Deutsche Forschungsgemeinschaft, the BMBF (Leitprojekt Magnetoelektronik) and the EC-TMR program "DYNASPIN" No. FMRX-CT97-0124.

References

[1] M. Bauer, O. Büttner, S.O. Demokritov, B. Hillebrands, V. Grimalsky, Yu. Rapoport, A.N. Slavin, Phys. Rev. Lett. **81**, 3769 (1998).
[2] M. Bauer, R. Lopusnik, J. Fassbender, B. Hillebrands, Appl. Phys. Lett. **76**, 2758 (2000).
[3] M. Bauer, Ph.D. thesis, Universität Kaiserslautern (2001).
[4] R. Lopusnik, Ph.D. thesis, Universität Kaiserslautern (2001).

6.6 Excitation and propagation of spin wave packets in thin garnet films by a short field pulse using space- and time-resolved Brillouin light scattering spectroscopy

M. Bauer and B. Hillebrands[1]

Spin waves have been observed using the space- and time-resolved magneto-optic Kerr effect, as discussed in the preceding Section 6.5. Subject of this report is the demonstration that spin waves excited by a single current pulse can be detected by a spectroscopic technique like Brillouin light scattering with space and time resolution (TRBLS). New for this approach is the non-resonant excitation of spin waves, as opposite to the excitation with a harmonic microwave driving field.

In the experiment a thin single-crystalline yttrium iron garnet (YIG) film (thickness 7 µm, width 18 mm, length 26 mm, saturation magnetization 1750 Oe, FMR line width FWHM 0.6 Oe at 4 GHz) is saturated by a static magnetic field of 800 Oe parallel to the long film side. A 50 µm wide and 2 mm long microstrip transmission line antenna is aligned perpendicular to the applied static field. Thus the spin wave packets will propagate parallel to the applied static field. This spin wave mode is known as the magnetostatic backward volume wave (MSBVW) mode. The

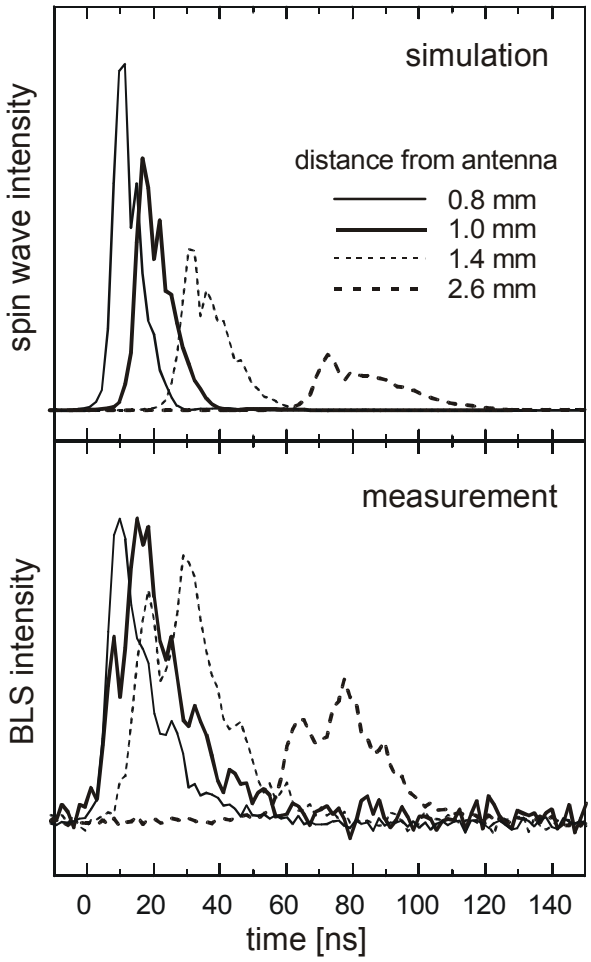

Fig. 1: Excitation and propagation of spin wave packets. Shown is the simulated (top) and measured (bottom) time response of the spin wave intensity for different distances from the excitation antenna from 0.8 mm to 2.6 mm.

[1] In collaboration with V. Tyberkevich, Radiophysics Faculty, National Taras Shevchenko University of Kiev, Ukraine; and A. Slavin, Department of Physics, Oakland University, USA.

antenna is connected to a pulse generator able to create field pulses of about 5 Oe magnitude, 280 ps pulse duration, 100 ps rise time (10% – 90%), and 200 ps fall time (90% – 10%).

First, the excitation and propagation of spin wave packets have been investigated. Figure 1 shows the simulated (top) and measured (bottom) time response of the spin wave intensity for different distances from the excitation antenna from 0.8 mm to 2.6 mm. The data have been taken with the TRBLS technique in forward scattering geometry. The acquisition time for each time response curve was about 10 hours compared to a few seconds in the case of a microwave driving field. In order to compensate different acquisition times the intensity is normalized to the large residual background noise. The main issue is demonstrated clearly: single current pulses excite spin waves which are clearly detected in the TRBLS experiment.

In order to understand the results we have made simulations of the expected spin wave response. Most of the qualitative features of the experiment can be seen in the simulation. The experimentally obtained times of arrival of the spin wave packet at the point of observation is well reproduced by the model calculation, as well as the profile of the excited pulse. In the simulations trapezoidal pulses with a duration of 280 ps, a rise time (0% – 100%) of 132 ps, a fall time (100% – 0%) of 266 ps, and a cosine lateral current distribution in the antenna have been used.

It is remarkable that, although the duration of the excitation pulse is chosen equal to about one FMR precession period, the duration of the propagating spin wave packet is about 15 ns, thus 50 times larger, as measured at a distance of 2.6 mm from the antenna. This can be understood by the fact, that these short pulses excite spin waves over a very wide frequency spectrum range. Since spin waves with different frequencies have different group velocities due to the dispersing character of the medium, the spin wave packet grows in width very fast after its generation.

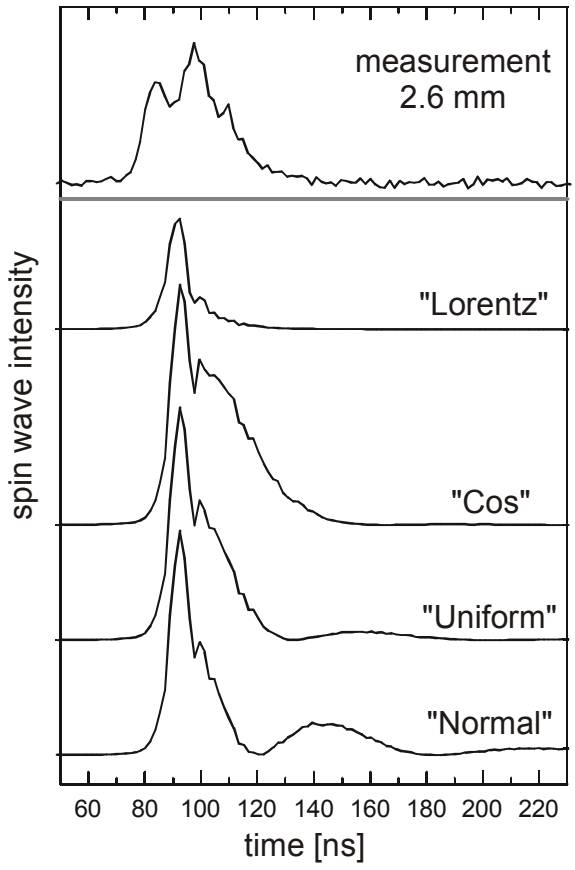

Fig. 2: Comparison of the simulated time response of the spin wave intensity for different lateral current distributions across the excitation antenna with the experiment for a distance of 2.6 mm from the antenna. For the expressions of the current distributions see Eqs. (1) – (4).

Second, the excitation pattern is very sensitive to the lateral current distribution across the antenna. Consequently this method has been used to compare different current distributions with the experimental data. Figure 2 shows the time response of the spin wave intensity for a distance of 2.6 mm from the antenna for the experimental data (top) and for different current distributions. The investigated current distributions $A(z)$ and the corresponding Fourier transforms A_k across the antenna of finite width w have the form:

"Normal":	$A(z)=\frac{1}{\sqrt{1-(2z/w)^2}}$	(1a)	$A_k = J_0(kw/2)$	(1b)
"Uniform":	$A(z)=1$	(2a)	$A_k = \frac{\sin(kw/2)}{kw/2}$	(2b)
"Cos":	$A(z)=\cos(\pi z/w)$	(3a)	$A_k = \frac{\cos(kw/2)}{1-(kw/\pi)}$	(3b)
"Lorentz":	$A(z)=\frac{1}{1+(2z/w)^2}$	(4a)	$A_k = \exp(-kw/2)$	(4b)

$J_0(x)$ is the Bessel function of zero order. The "Normal" distribution is referred to the current distribution according to the Maxwell electrodynamics theory.

The different excitation patterns observed in Fig. 2 can be understood as follows. The sensitivity of the current distribution across the antenna strongly influences the wave vector spectrum of the excited spin waves. Since spin waves with different wave vectors have different group velocities due to the dispersing character of the medium, the excitation and evolution of the spin wave packet depends very sensitively to the current distribution. It seems that the experimental data can be best described by a cosine like current distribution. Thus the method is well suited to study the effects of current distribution in the exciting antenna structure.

6.7 Extraction of magnetization components from magneto-optical studies of magnetization dynamics

R. Lopusnik, J. Fassbender, and B. Hillebrands[1]

Magneto-optics, compared to other methods, has among many advantages also disadvantages. One of them is that the measured magneto-optical (MO) signal is not directly proportional to the magnetization. The MO response of a system consists of a mixture of the polar and longitudinal Kerr effects if *s*-polarized light is used. If *p*-polarized light is used the situation becomes even more complicated since in this case all three magnetization components may contribute to the total MO signal. It is of principal importance for the understanding of the magnetization dynamics to measure all three magnetization vector components independently [1-4]. In order to extract useful information from MO studies of the magnetization dynamics a detailed analysis of the MO response is necessary.

First, analytical expressions for the MO response *linear in the magnetization* of the system with the magnetization pointing in an arbitrary direction have been derived. In order to describe the interaction of light with a layered media consisting of a stack of layers the formalism developed by Yeh for non-absorbing media [5] and extended by Visnovsky for absorbing media displaying magneto-optical effects [6] was used. The MO Kerr rotation θ_K is proportional to the real part of the ratio between off-diagonal and diagonal elements of the reflection matrix, $\Re(r_{ps}/r_{ss})$. For *s*-polarized light used in experiment this ratio can be expressed as

$$\theta_K \approx R\left(\frac{r_{ps}}{r_{ss}}\right) = \frac{r_{ps}^{(pol)} \cos\theta_M + r_{ps}^{(lon)} \sin\theta_M \sin\varphi_M}{r_{ss}} = \theta_K^{(pol)} m_z + \theta_K^{(lon)} m_y, \qquad (1)$$

m_z and m_y denote the direction cosines or normalized magnetization components in *z* and *y* directions, and $\theta_K^{(pol)}$ and $\theta_K^{(lon)}$ denote the polar and longitudinal Kerr effect amplitude, respectively. The exact form of this expression can be found in [7].

From Eq. (1) it follows that three complementary measurements allow one to separate the magnetization components from the total MO signal. The experimental procedure is similar to that described in [8] used for a separation of longitudinal and polar magnetization components from static hysteresis loop measurements. The separation of the in-plane magnetization components uses the principle of the vector Kerr magnetometer presented in [9]. Note that the model is valid for *linear magneto-optical effects* only. If one considers second-order MO effects in addition, the situation is considerably more complicated.

A series of three independent measurements shown in Fig. 1 allows one to separate the contribution to the total MO effect. Both the static field and the magnetic field pulses will be kept fixed with respect to the sample, and the whole system, i.e., the magnetic fields and the sample will be simultaneously rotated about the normal of the sample surface by 0, 90, and 180 degrees, respectively. A summation of the measurements for 0 degree and 180 degrees yields the polar magnetization components

$$\theta_K^{(pol)} m_z = \frac{1}{2}\left(\theta_K(0°) + \theta_K(180°)\right),$$

and their difference the longitudinal components

[1] In collaboration with S. Visnovsky, Charles University, Prague, Czech Republic.

$$\theta_K^{(pol)} m_z = \frac{1}{2}\left(\theta_K(0°) - \theta_K(180°)\right).$$

With the knowledge of the polar component the transverse magnetization component can be obtained from the measurement for the 90 degree rotation geometry

$$\theta_K^{(lon)} m_x = \theta_K(90°) - \theta_K^{(pol)} m_z .$$

In order to express a magnetization motion in terms of magnetization components, the time response of the MO signal has to be normalized to the amplitudes of the longitudinal and the polar Kerr effect. These can be obtained from quasi-static hysteresis loop measurements. The procedure has been proven to be valid for a system with linear MO effects only. If MO effects of higher order are present a more complicated procedure must be used [10].

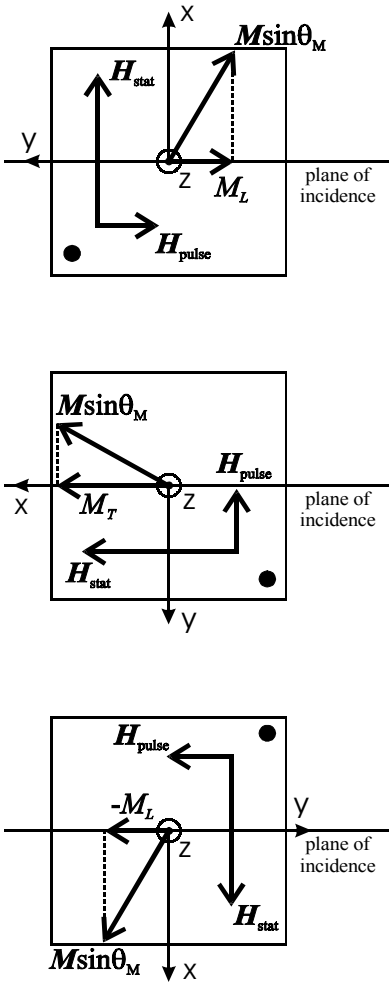

Fig. 1: Sketch of the three sample-field geometries, which are required to separate the different magnetization components

In order to demonstrate the applicability of Eq. (1) the MO response of a $Bi_{0.96}Lu_{2.04}Fe_5O_{12}$ film on a gadolinium gallium garnet substrate is evaluated numerically. The optical and magneto-optical data for $Bi_{1.07}Y_{1.86}Pb_{0.07}Fe_{4.962}Pt_{0.038}O_{12}$ film and the $Gd_3Ga_5O_{12}$ (GGG) substrate, given in [11] and [12], are collected in Table 1. They reasonably represent the $Bi_{0.96}Lu_{2.04}Fe_5O_{12}$ system investigated experimentally. Note that in the simulations the permittivity of GGG has been assumed to be smaller than the value given in [12]. If there is a back reflection from the interface GGG/air the effective permeability of the substrate is smaller. The constant has been chosen in such a way, that the simulated and measured longitudinal Kerr effect amplitudes in the saturation are the same. Using this value in the calculation of the amplitude of the polar Kerr effect, one obtains $\theta_K^{(pol)} = 340$ mdeg. This value is in good agreement with the measured value.

In order to compare the model with experimental data the Landau-Lifshitz-Gilbert (LLG) equation has been used to simulate the magnetization motion for two different field pulse duration

Material	ε_1	ε_2
vacuum	1	0
$Bi_{1.07}Y_{1.86}Pb_{0.07}Fe_{4.962}Pt_{0.038}O_{12}$	5.831 – i 0.011527	-0.0081042 + i 0.0008045
$Gd_3Ga_5O_{12}$ [11]	3.8064	0
$Gd_3Ga_5O_{12}$ this work	1.73	0

Tab. 1: Permittivity tensor elements used for the calculation.

times. The method used to solve the LLG equation is described in [13]. The parameters for the simulations have been chosen to be the same as those in the experiments. The static field was chosen H_{stat} = 91 Oe, the magnetic field pulse H_{pulse} = 2 Oe, and the duration times T_{pulse} = 3.32 ns and 3.75 ns. For values close to these field pulse durations ringing suppression and a very pronounced ringing have been found. A rectangular pulse shape has been chosen in the LLG simulations. The results for both field pulse duration times are shown in Fig. 2. The symbols display the experimental results. The agreement in the shape and amplitude between simulation and experiments is excellent.

References

[1] M. R. Freeman, W.K. Hiebert, A. Stankiewicz, J. Appl. Phys. **83**, 6217-6222 (1998).

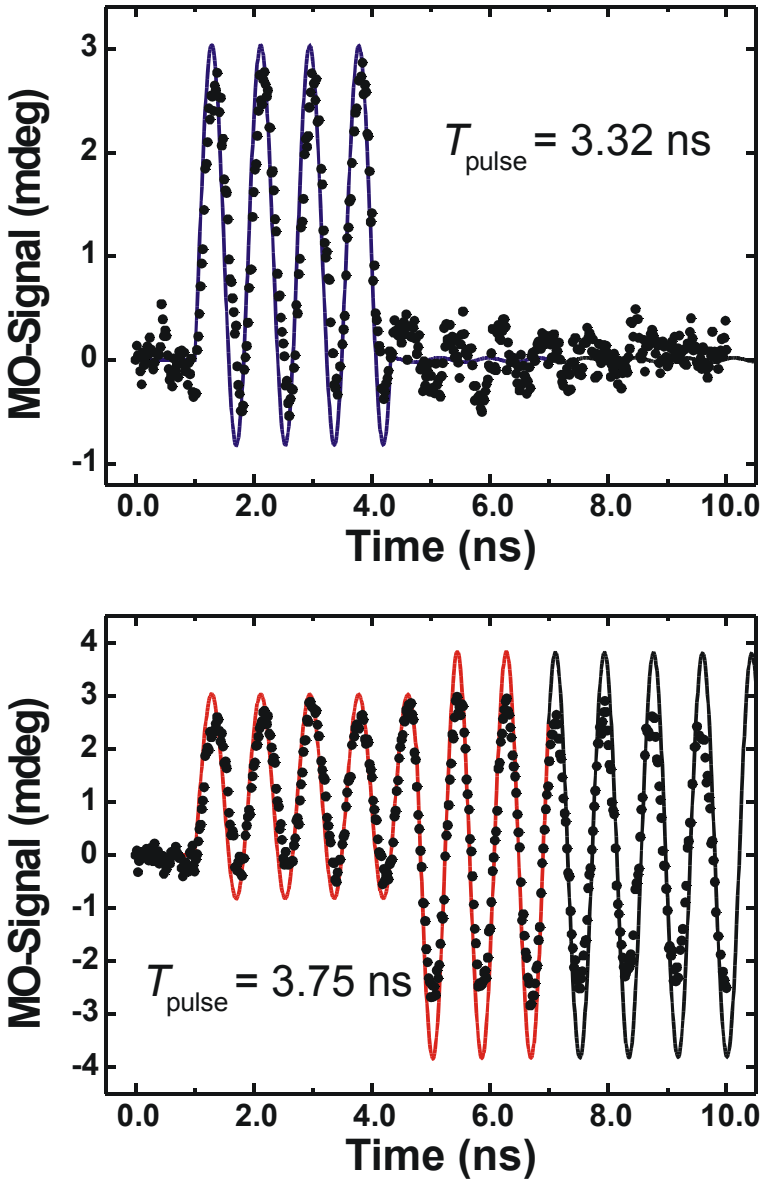

Fig. 2: MO signal as a function of time calculated using Eq. (1) for a $Bi_{0.96}Lu_{2.04}Fe_5O_{12}$ film on a GGG substrate (solid line). Two different field pulse duration times have been chosen corresponding to the ringing suppression and most pronounced ringing situations. The symbols display the experimental results.

[2] B.C. Choi, M. Belov, W.K. Hiebert, G.E. Ballentine, M.R. Freeman, Phys. Rev. Lett. **86**, 728-731 (2001).
[3] T.M. Crawford, C.T. Rogers, T.J. Silva, Y.K. Kim, Appl. Phys. Lett. **68**, 1573-1575 (1996).
[4] P. Kabos, A.B. Kos, T.J. Silva, , J. Appl. Phys. **87**, 5980-5982 (2000).
[5] P. Yeh, Surf. Sci. **96**, 41-53 (1980).

[6] S. Visnovsky, Czech. J. Phys. B **36**, 625-650 (1986).
[7] S. Visnovsky, R. Lopusnik, M. Bauer, J. Bok, J. Fassbender, B. Hillebrands, Opt. Express **9**, 121-135 (2001).
[8] H.F. Ding, S. Pütter, H.P. Oepen, J. Kirschner, J. Magn. Magn. Mater. **212**, L5-L11 (2000).
[9] C. Daboo, J.A.C. Bland, R.J. Hicken, A.J.R. Ives, M.J. Baird, M.J. Walker, Phys. Rev. B **47**, 11852-11859 (1993).
[10] R. Lopusnik, Ph.D. thesis, Kaiserslautern (2001).
[11] V. Doormann, J.-P. Krumme, H. Lenz, J. Appl. Phys. **68**, 3544-3553 (1990).
[12] W. Gunsser, U. Wolfmeier, J. Fleischhauer, in *Landolt-Börnstein Numerical Data and Functional Relationship in Science and Technology, vol. 12a (Magnetic and Other Properties of Oxides and Related Compounds)*, K.-H. Hellwege and A.M. Hellwege *Eds*., Springer Verlag, Berlin, Heidelberg, New York, 1978, p. 307.
[13] M. Bauer, J. Fassbender, B. Hillebrands, R.L. Stamps, Phys. Rev. B **61**, 3410-3416 (2000).

6.8 Write endurance of magnetic tunnel junctions

M. Bauer, J. Fassbender, and B. Hillebrands[1]

Since the experimental realization of tunnel magnetoresistance (TMR) junctions with a high amplitude of the TMR signal at room temperature [1], magnetic random access memory (MRAM) devices [2,3] have attracted a lot of attention. The two main advantages of this technology are the simple cross-point architecture [3] capable to increase the storage density with current lithography techniques and the nonvolatile character which reduces the power consumption to a large degree. Thus device cooling aspects are minor and applications in mobile devices are easier to achieve.

Devices based on magnetic tunnel junctions (MTJ) consist of a hard magnetic layer with a reference magnetization and a free soft magnetic layer separated by an isolating tunnel barrier [3]. The soft magnetic layer exhibits two easy magnetization directions, i.e., parallel and antiparallel to the magnetization direction of the pinned layer representing the two states of information. The stored information is read out by a resistance measurement. In order to compete with semiconductor based dynamic random access memory devices the information writing speed and the read/write endurance become important parameters. The device writing speed will be addressed in Section 6.9.

The MTJ sample consisting of the storage element and a write line was prepared by sputtering the different materials onto a Si(001) substrate followed by optical lithography and Ar dry etching. First, 5 nm Ru and 50 nm Cu were deposited to provide a highly conductive layer to be used as a write line. Then the hard magnetic layer system comprising a CoFe/Ru based artificial antiferromagnet (AAF) [4] was deposited. As the tunnel barrier 1.5 nm Al was sputtered and plasma oxidized. Next, as the soft magnetic layer, 6 nm of $Ni_{80}Fe_{20}$ (FM) was deposited. Finally the whole layer system was protected by a 10 nm Cu and a 3 nm Cr cap layer. The second write line was omitted in order to provide optical access to the soft magnetic layer. After deposition

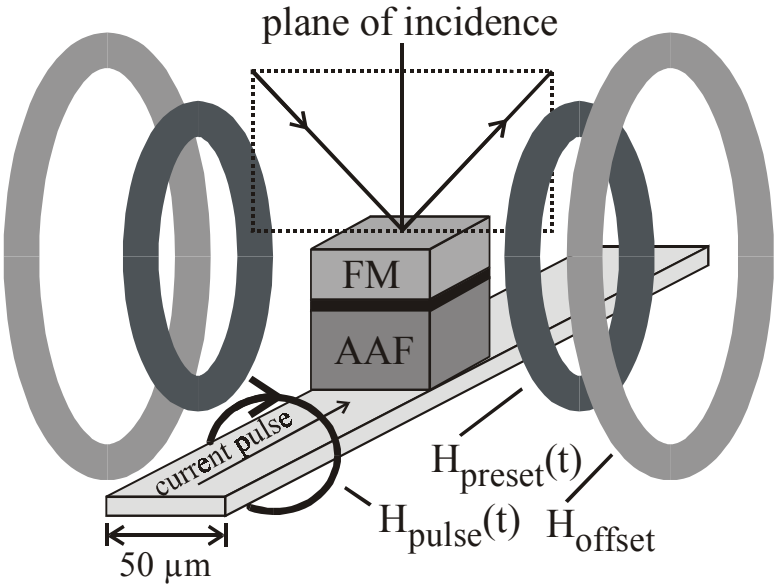

Fig. 1: Sketch of the MTJ structure and the magnetic fields configuration. The MTJ structure consists of an artificial antiferromagnet (AAF) separated from a soft magnetic layer (FM) via a tunnel barrier. The capping layers have been omitted in the sketch for clarity. The whole stack is located on top of a 50 µm wide strip line. In addition two pairs of Helmholtz coils are used to generate a preset and a static offset fields. The plane of light incidence for the magneto-optic Kerr effect is indicated.

[1] In collaboration with J. Bangert, J. Wecker, Siemens AG, Corporate Technology CT MM 1, 91050 Erlangen, Germany.

the stack was patterned into 50 µm wide and 230 µm long elements each between two bond pads. The magnetic material was removed from the bond pads and a part of the write line leaving an MTJ element of the dimension 50 µm by 220 µm. Finally the element was covered with a 60 nm thick SiO_x protection layer. A sketch of the MTJ structure is shown in Fig. 1.

The magnetization response of the soft magnetic layer was investigated by means of a time resolved magneto-optic (MO) Kerr magnetometer [5]. Time resolution is achieved by a stroboscopic technique. The magnetization response is sensed by the MO Kerr effect of the light pulses and averaged over the laser spot size of 47 µm by 21 µm. The magnetization of the pinned layer and the two magnetization states of the soft layer are oriented perpendicular to the strip line and parallel to the plane of incidence. Note that all fields used in the experiments were small compared to the saturation field of the hard magnetic layer, and thus the hysteresis loop of the soft layer was investigated only.

In Fig. 2a the static hysteresis loop of the soft magnetic layer is shown using a slow sweep of the offset field. Two features are observed: i) the hysteresis loop is shifted by a value of –10 Oe with respect to zero applied field. ii) the squareness of the hysteresis loop is reduced compared to a single infinite permalloy. The shift of the hysteresis loop can simply be attributed to a Néel-type orange-peel coupling [6–8] due to the correlated roughness of both magnetic layers. The corresponding ferromagnetic coupling strength is 5 merg/cm^2. A possible magnetostatic coupling due to uncompensated poles near the edges can be excluded since the sample area is rather large. The grain size distribution, the shape anisotropy and a possible slight misalignment of the pinning direction are responsible for the reduced squareness of the hysteresis loop leading to a remanent magnetization of about 70% of the saturation value. Consequently, the magnetization vector averaged over the laser beam spot shows an in-plane tilt with respect to the direction of the field pulse as proven by a complementary magneto-optic measurement of the transverse magnetization component. It is likely, that here a domain structure has evolved with the mean magnetization direction along this tilt direction.

Figure 2b shows the hysteresis loop which is obtained by cycling the preset field at 50 kHz with a field range of ±10 Oe (≡ 2 MOe/s). The field range is sufficient to measure the minor loop without perturbing the magnetization state of the pinned layer. An offset field of 10 Oe was superimposed in order to compensate the Néel coupling field and to center the hysteresis loop.

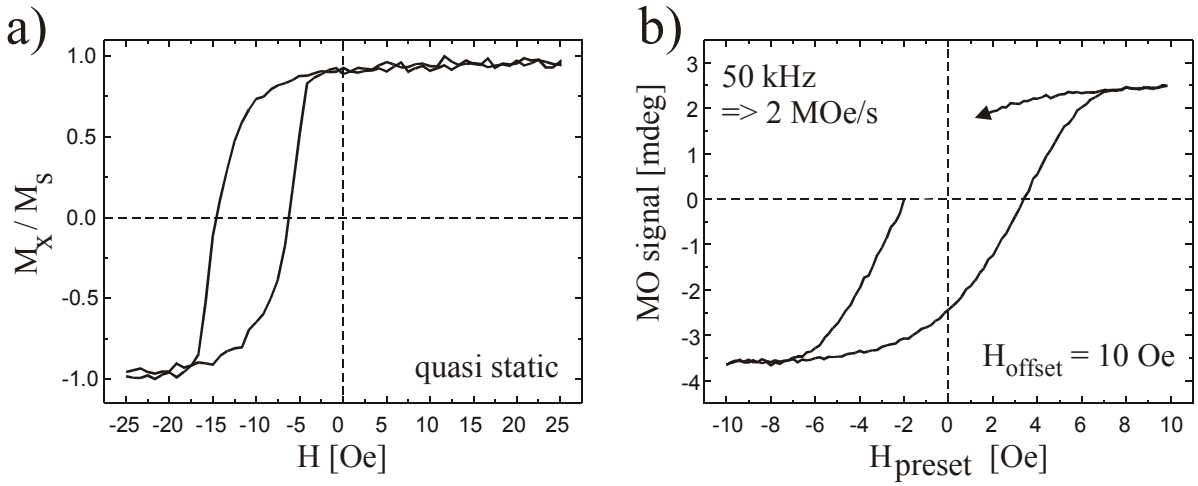

Fig. 2: Quasi static (a) and dynamic (b) hysteresis loops of the soft magnetic layer of the MTJ structure (minor loop). In order to center the hysteresis loop for the dynamic measurements an offset field of 10 Oe has been applied.

Since our detection system is low pass filtered the hysteresis loop at 50 kHz has been accumulated in the stroboscopic mode. Due to technical restrictions of the delay generator the time evolution of the magnetization has been determined only for the first 18 μs. This leads to a gap in the 20 μs = 1/(50 kHz) full loop. Since the temporal magnetic field profile of the Helmholtz coils is well known the time axis of the measurement can be rescaled into a magnetic field axis and thus a hysteresis loop with a sweep rate of 50 kHz is obtained (see Fig. 2b). No significant difference with respect to coercivity and remanence is found compared to the static magnetization reversal. For high speed switching experiments described in Section 6.9 this 50 kHz loop will be used to re-establish the magnetization configuration after application of each magnetic field pulse.

Recently it was demonstrated, that the magnetization reversal of the soft magnetic layer via domain wall motion can lead to a demagnetization of the magnetically pinned layer [9, 10]. It was shown that if the reference layer is formed by an exchange biased structure its magnetization remains stable at least for 10^7 cycles whereas in hard magnetic structures the magnetization decays logarithmically with the number of field cycles. In our experiment the reference layer consists of an AAF [4]. The write endurance was tested at least at 10^{11} cycles with a current induced switching field. The cycling experiments have shown an unaffected hysteresis loop of the soft magnetic layer after more than 10^{11} field cycles with an amplitude of ±10 Oe.

Work supported by the BMBF (Leitprojekt Magnetoelektronik) and the EC-TMR program "DYNASPIN" No. FMRX-CT97-0124. We thank J. Wecker and J. Bangert for supplying the samples.

References

[1] J.S. Moodera, L.R. Kinder, T.M. Wong, R. Meservey, Phys. Rev. Lett. **74**, 3273 (1995).
[2] S. Tehrani, E. Chen, M. Durlam, M. DeHerrera, J.M. Slaughter, J. Shi, G. Kerszykowski, J. Appl. Phys. **85**, 5822 (1999).
[3] S.S.P. Parkin, K.P. Roche, M.G. Samant, P.M. Rise, R.B. Beyers, R.E. Scheuerlein, E.J. O'Sullivan, S.L. Brown, J. Bucchigano, D.W. Abraham, Y. Lu, M. Rooks, P.L. Trouilloud, R.A. Wanner, W.J. Gallagher, J. Appl. Phys. **85**, 5828 (1999).
[4] H.A.M. van den Berg, W. Clemens, G. Gieres, G. Rupp, M. Vieth, J. Wecker, S. Zoll, J. Magn. Magn. Mater. **165**, 524 (1997).
[5] M. Bauer, R. Lopusnik, J. Fassbender, B. Hillebrands, Appl. Phys. Lett. **76**, 2758 (2000).
[6] L. Néel, Comptes Rendus Acad. Sci. **255**, 1676 (1962).
[7] B.D. Schrag, A. Anguelouch, S. Ingvarsson, G. Xiao, Yu Lu, P.L. Trouilloud, A. Gupta, R.A. Wanner, W.J. Gallagher, P.M. Rice, S.S.P. Parkin, Appl. Phys. Lett. **77**, 2373 (2000).
[8] J. Fassbender, M. Bauer, Europhys. Lett. **55**, 119 (2001).
[9] S. Gider, B.-U. Runge, A.C. Marley, S.S.P. Parkin, Science **281**, 797 (1998).
[10] L. Thomas, M.G. Samant, S.S.P. Parkin, Phys. Rev. Lett. **84**, 1816 (2000).

6.9 Switching dynamics of magnetic tunnel junctions

M. Bauer, J. Fassbender, and B. Hillebrands[1]

In magnetic random access memory (MRAM) magnetic tunnel junctions (MTJ) are used to sense the value of a logical bit stored in a memory element. The effect is based on the fact, that the electrical resistance of a MTJ depends on the relative orientation of the magnetization of a storage layer with respect to a reference layer in the cell. Since the preparation of these devices becomes more and more standard the research concentrates now on the aspects of read/write endurance and information writing speed.

The preparation, the quasi-static magnetic characterization and the write endurance of MTJs is described in the preceding Section 6.9. Here the magnetization switching on the picosecond time-scale is addressed. The magnetization response of the soft magnetic layer of the MTJ was sensed by means of a time resolved magneto-optic (MO) Kerr effect magnetometer based on a stroboscopic technique [1]. Magnetic field pulses are generated by the launch of current pulses provided by an electronic pulse generator. The pulses were 0.25 – 4.15 ps wide and with 0.1 ns rise time and 0.2 ns fall time. Since a stroboscopic technique is used the initial magnetization direction must be re-initialized in each measurement cycle in order to provide the same initial state prior to the application of the field pulse. For this purpose a periodic 50 kHz sweep field of 10 Oe field amplitude and symmetric triangular shape was applied. In Section 6.8 it is reported that this 50 kHz hysteresis cycle shows no significant difference to a quasi-static loop concerning saturation magnetization and coercivity and can thus be used for the re-initialization. The fast time-resolved magneto-optic Kerr effect measurements were performed at the zero crossing of the sweep field. The field pulse is applied in either of the two directions perpendicular to the strip line. Note that all fields used in the experiments were small compared to the saturation field of the hard magnetic layer, and thus the hysteresis loop of the soft layer was investigated only.

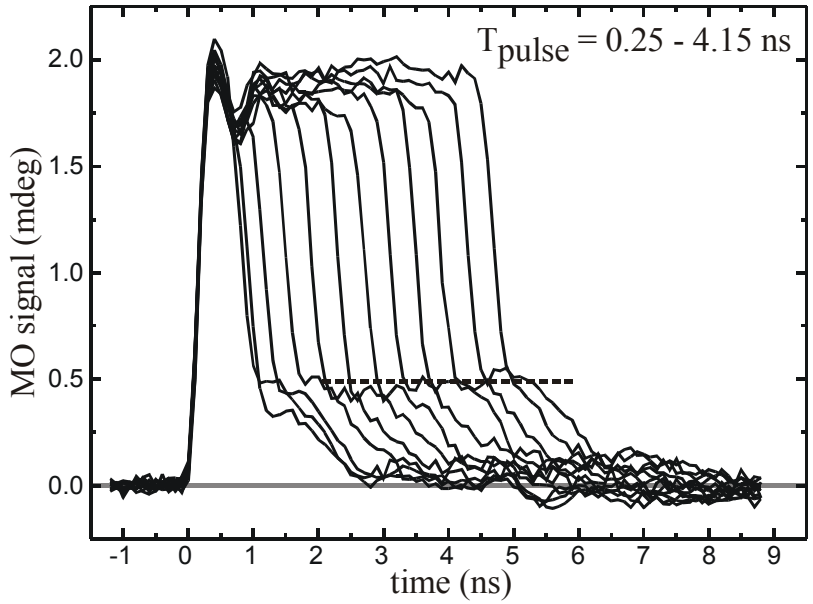

Fig. 1: Time evolution of the magnetization response upon application of a magnetic field pulse of 0.25 – 4.15 ns duration (10 V magnitude) in the case of writing without change of the storage content. The magnetic field amplitude is 15 Oe. An offset field of +10 Oe has been applied in order to compensate the Néel coupling field. The dashed line indicates the transition of the two different magnetization reversal behaviors at the falling edge of the pulse.

[1] In collaboration with J. Bangert, J. Wecker, Siemens AG, Corporate Technology CT MM 1, 91050 Erlangen, Germany.

Since the information status of a MTJ structure is not known a priori, two different write processes must be considered: i) writing without change of the storage content and ii) writing with change of the storage content. Figure 1 shows the time evolution of the magnetization response upon field pulse application in case i). The pulse duration is varied between 0.25 and 4.15 ns. The magnetic field pulses amplitude is 15 Oe (10 V pulse amplitude). At the leading edge of the magnetic field pulse a fast response of the magnetization is found. A rise time of 0.25 ns is observed. The fast response is followed by a heavily damped precession of the magnetization. The magnetization is equilibrated after about one precessional period. At the falling edge of the field pulse two different regimes in magnetization dynamics are observed. At first the magnetization follows the magnetic field pulse rapidly until the amplitude is diminished by about 75 %. Afterwards a gradual decrease is found. The magnetization relaxes to the final state within the next 2 ns. No difference between initial and final states is found. The transition between both regimes is indicated by the dashed line in Fig. 1. For a pulse duration longer than half a precessional period the onset of the gradual decrease is independent of the pulse duration. For shorter pulse durations the magnetization reversal behavior is slightly different because the precession is still present at the time the field pulse terminates.

The magnetization reversal behavior in case ii), i.e., writing with change of the storage content, is shown in Fig. 2 for different field pulse durations between 0.25 and 3.15 ns. Similar to the previous case a fast response of the magnetization at the leading edge of the pulse and a heavily damped precession is found. However, instead of the plateau in the MO signal observed in case i), the longer the field pulse lasts the larger the MO signal grows. Although the field pulse magnitude is larger than the saturation field expected from quasi-static hysteresis measurements the magnetization is not saturated in this dynamic case. Since the precessional motion of the magnetization is completely damped, the increase in the MO signal indicates that magnetic aftereffects could play a significant role on that time scale. This interpretation is further supported by the fact that the final magnetization state depends on the field pulse duration as evidenced by the different levels of the Kerr rotation at 8.5 ns. At the falling edge of the field pulse two different reversal regimes are observed. In contrast to case i) the transition between both regimes (dashed line in Fig. 2) depends on the field pulse duration. In fact, the onset of the gradual decrease as a function of pulse duration matches the evolution of the final MO signal prior to field pulse termination.

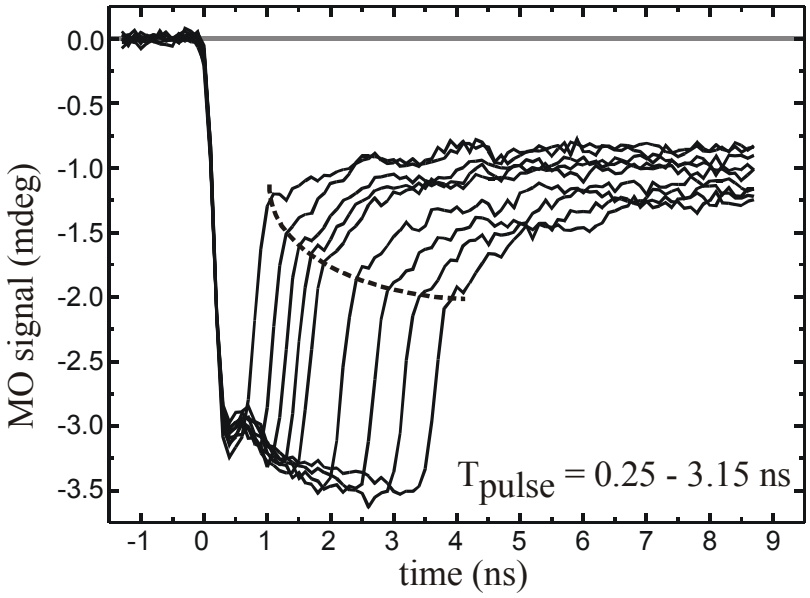

Fig. 2: Time evolution of the magnetization response upon application of a magnetic field pulse of 0.25 – 3.15 ns duration (10 V magnitude) in the case of writing with change of the storage content. The magnetic field amplitude is 15 Oe. An offset field of +10 Oe has been applied in order to compensate the Néel coupling field. The dashed line indicates the transition of the two different magnetization reversal behaviors at the falling edge of the pulse.

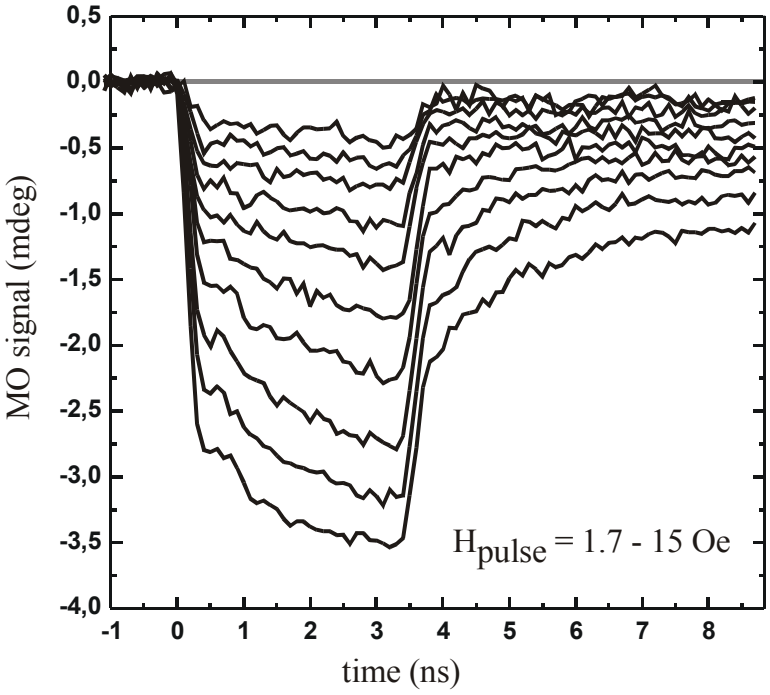

Fig. 3: Time evolution of the magnetization response upon application of a magnetic field pulse of 3.15 ns duration in the case of writing with change of the storage content. The magnetic pulse amplitude is varied between 1.7 and 15 Oe. An offset field of +10 Oe has been applied in order to compensate the orange-peel coupling field.

The data for varying pulse amplitude in case ii) is presented in Fig. 3. The field pulse duration of 3.15 ns is kept constant and the magnetic field pulse amplitude is varied between 1.7 and 15 Oe. The features are similar to those observed for a variation of pulse duration (cf. Figs. 2 and 3). The MO signal at 8.5 ns decreases with decreasing field pulse magnitude. Since no change in this behavior is observed it is likely that the maximum available field pulse magnitude is too small to completely saturate the magnetization of the sample. The difference between the initial and final magnetization state decreases with decreasing field pulse amplitude.

Work supported by the BMBF (Leitprojekt Magnetoelektronik) and the EC-TMR program "DYNASPIN" No. FMRX-CT97-0124. We thank J. Wecker and J. Bangert for supplying the samples.

Reference

[1] M. Bauer, R. Lopusnik, J. Fassbender, B. Hillebrands, Appl. Phys. Lett. **76**, 2758 (2000).

6.10 Self-generation of spin wave bullets in magnetic films

A.A. Serga, S.O. Demokritov, and B. Hillebrands[1]

Recently new two-dimensional non-linear wave objects – spin wave bullets – have been discovered in our group [1]. Here we report self-generation of spin wave bullets in an active ring based on an yttrium-iron garnet (YIG) film.

The experiment is performed using the time and space resolved Brillouin light scattering technique which provides access to the two-dimensional intensity distribution of the spin wave packets $I(y,z)$ as a function of time. Spin waves propagate in a high quality ($2\Delta H_0 = 0.6$ Oe) single crystal YIG (111) film with thickness of 7 μm. The lateral sizes of the sample (26×18 mm^2) are much large than all possible characteristic length of non-linear packet formation [2, 3], thus realizing two-dimensional propagation conditions of the waves. The YIG sample was placed on top of a microstrip structure which consists of two microstrip antennae of 50 μm width and 2.5 mm length spaced 6.5 mm apart. The bias magnetic field $H_0 = 1735$ Oe was applied in the plane of the film perpendicular to the antennae. Thus, the microstrip structure together with the YIG film forms a transmission line for backward volume magnetostatic waves (BVMSW). This transmission line was connected to a microwave switch and combined amplifier forming a closed ring. The peak power of self generated pulses at the input antenna of the spin wave transmission line, P, was varied in the experiments from 1 mW to 300 mW by tuning the total gain of the amplifier. As a result the spin wave amplitude was also changed significantly. The amplifier

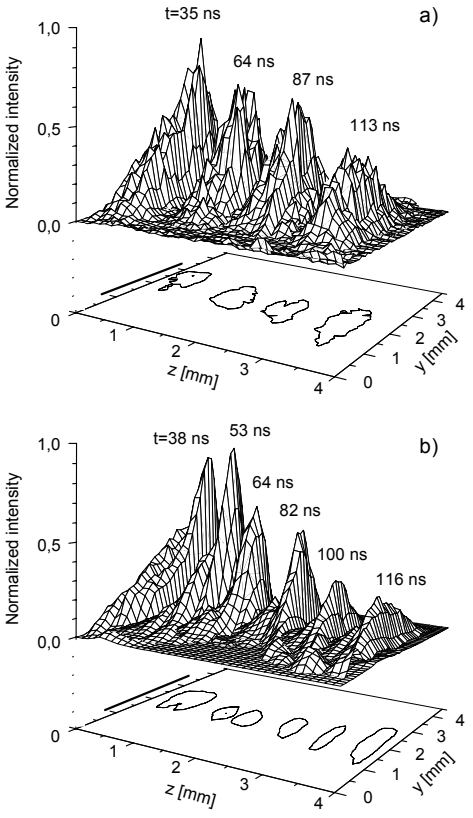

Fig. 1: Spin wave bullet formation from a two-dimensional self-generated BVMSW packet. The upper part of each panel shows the spin wave intensity distribution in the film, created by the BVMSW propagating pulse at successive instants of time after the launch of the packet. The lower part of each panel shows the cross sections of the propagating pulse at half maximum power. Panels (a) and (b) correspond to quasi-linear ($P = 1$ mW) and strongly nonlinear ($P = 220$ mW) spin wave packets, respectively. The black stripes in the lower frames indicate the position of the antennae.

[1] In collaboration with A.N. Slavin, Oakland University, U.S.A.

used in this work has a very broad dynamic range (above 25 dB between 4 and 10 GHz) and a peak power well above the working power. Thus the nonlinear properties of the ring are determined solely by the YIG film. The role of the switch (driven by an external pulse generator) was to periodically interrupt the feedback in the ring for suppression of parasitic oscillations. The described microwave setup allows one to generate a train of short (about 20 ns duration) two-dimensional spin wave packets with the carrier frequency from 6.98 to 7.03 GHz and with the carrier wavenumber $k_{nz} = 150$ rad/cm. The time interval between pulses in the train of about $T_0 = 190$ ns was determined by the total delay time in the ring. For small amplifier gains the synchronization of the switch with the ring is crucial: by deviation of the switch modulation period from T_0 for more than ±3 ns the self-generation of the microwave pulses breaks down. The observed phenomenon can be considered as a two-dimensional analog of the soliton self-generation in quasi-one-dimensional systems [4].

The two-dimensional propagation of single packets of the train is illustrated in Fig. 1. As it is clear from Fig. 1, the dynamics of quasi-linear ($P = 1$ mW) and strongly nonlinear ($P = 220$ mW) spin wave packets are essentially different. The intensity of a quasi-linear packet monotonically decreases with propagation time due to losses and diffraction widening of the packet (Fig. 1a). In contrast, a strongly nonlinear packet demonstrates its sharpening during the first 50 ns of its propagation, as it is seen in Fig. 1b. That is the result of nonstationary spatiotemporal self-focusing of the 2D spin wave packet in the nonlinear medium with dispersion and diffraction [1].

To investigate the properties of the self-generated spin wave bullets in detail, the dependence of the transverse packet width L_y was determined as a function of the propagation time, as shown in Fig. 2. For quasi-linear packets ($P = 1$ mW) one can see that up to $t = 80$ ns L_y does not change noticeably. This process of stable propagation is followed by a diffraction spreading. For more intensive packets ($P = 10$ mW) a clearly observable compression of the packet ($t \le 50$ ns) and a strongly pronounced bullet formation and its propagation $50 \text{ ns} \le t \le 70$ ns is observed. The transverse width of the bullet decreases here up to 85 % as compared to that of

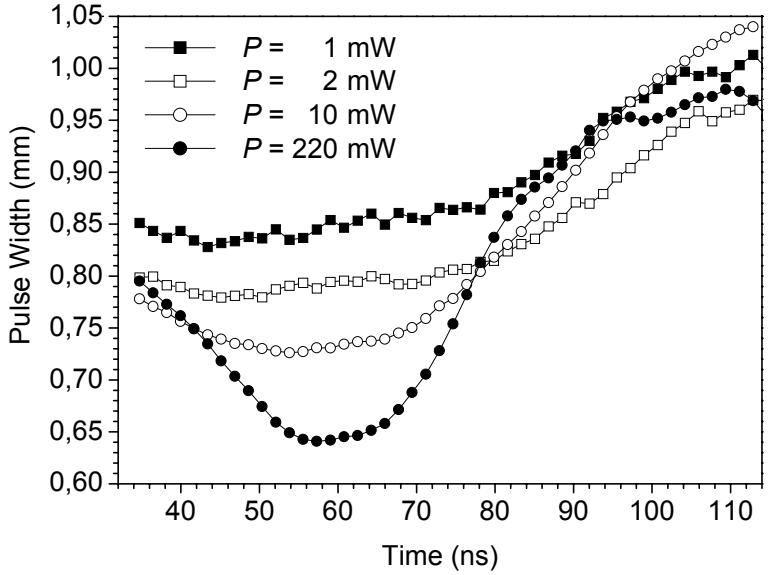

Fig. 2: Evolution of the transverse width of the spin wave packet L_y with propagation time t.

the quasi-linear packet. Finally, in a strong nonlinear regime ($P = 220$ mW) the situation is close to a collapse scenario: the width L_y decreases up to 76 % in comparison with that for the quasi-linear packet, the time of stable bullet propagation is reduced to 15 ns, and strong diffraction spreading follows for $t \geq 70$ ns .

Thus, Figs. 1 and 2 clearly demonstrate that there are profound regions of propagation times where the transverse sizes of the self-generated wave packets are almost constant, i.e., where propagation of self-generated bullets is observed.

The self-generated bullets turned out to be very similar to those created by means of an external microwave source [1]. As the parameters of the bullets do not relay to the method of their excitation (external source or self-generation) they can be classified as two-dimension eigenmodes of nonlinear medium with dispersion and diffraction.

This work was supported by the Deutsche Forschungsgemeinschaft, by the National Science Foundation (Grant No. DMR-0072017), and by the Civilian Research and Development Foundation (Grant No. UP1-2120).

References

[1] M. Bauer, O. Büttner, S.O. Demokritov, B. Hillebrands, V. Grimalsky, Yu. Rapoport, and A.N. Slavin, Phys. Rev. Lett. **81**, 3769 (1998).
[2] R. A. Staudiner, P. Kabos, H. Xia, B.T. Faber, and C.E. Patton, IEEE Transactions on Magnetics **34**, 2334 (1998).
[3] O. Büttner, M. Bauer, S.O. Demokritov, B. Hillebrands, Y. S. Kivshar, V. Grimalsky, Yu. Rapoport, and A.N. Slavin, Phys. Rev. B **61**, 11576 (2000).
[4] B. A. Kalinikos, N.G. Kovshikov, and C.E. Patton, Phys. Rev. Lett. **80**, 4301 (1998).

C. Epitaxial Growth

6.11 Non-monotone step-induced magnetic anisotropy of Fe films prepared on vicinal Au(001) surfaces with different step orientations

M. Rickart, S.O. Demokritov, and B. Hillebrands

Magnetocrystalline anisotropies of ultrathin ferromagnetic films play a key role in the design of new materials for applications in research and technology. A break of the lattice symmetry at the surface generates uniaxial magnetic anisotropies which do not exist in the bulk [1, 2]. An additional excellent testing ground is provided by vicinal films due to the break of the translational crystalline symmetry along the in-plane direction perpendicular to the miscut tilt axis. Two main mechanisms are believed to cause the step induced uniaxial anisotropy: the missing bonds of atoms at the surface (Néel's model) and strain within the film [3]. The dependence of the effective anisotropy strength on the film thickness d helps to determine the surface contribution to the anisotropy, since the $1/d$ dependence of the anisotropy strength is a characteristic feature of surface anisotropies [4] under the assumption that the strain is independent of thickness. We report on a study of the step-induced uniaxial in-plane anisotropy vs. the step density for the Fe/Au(001) system with the average orientation of step edges perpendicular to the [100]- as well as to the [110]-direction. The thickness dependent and independent contributions to the anisotropies are determined. We show that for one orientation of the steps the anisotropy changes its sign with increasing miscut angle.

The Fe films studied in this work were grown on vicinal MgO(001) substrates covered with a Au buffer layer. All samples were prepared in an ultra high vacuum (UHV) multi-chamber molecular beam epitaxy system. The films were deposited by an electron beam evaporator onto vicinal MgO(001) substrates (vicinal miscut angle varied between 0.5° and 7°) with deposition rates between 0.01 and 0.1 nm/s as monitored by a quartz microbalance. Structural analysis was carried out with LEED, RHEED and STM. For improved growth of the subsequent metallic layers it is necessary to remove the carbon contamination at the MgO surface. This was made by treating the substrates with a low energy atomic oxygen ion beam at room temperature [5]. Surfaces were judged clean if the Auger analysis with a sensitivity of better than 0.01 ML detected no remaining carbon contamination. Epitaxially grown Au buffers on vicinal to the (001) MgO surface were used as a base for the preparation of ultrathin bcc Fe films. MgO(001) with its lattice spacing of 0.421 nm is a good substrate for epitaxial growth of fcc Au(001) films (lattice constant 0.408 nm). Au films with the thickness of 150 nm were grown on MgO at a deposition rate of 0.5 ML/s and a substrate temperature of 120°C. The surface of the grown buffer reproduces the average orientation of the steps on MgO. Similar to our earlier studies [6], the obtained miscut of the Au-buffer surface differs slightly from that of the MgO surfaces due to a small difference of the layer-to-layer distances between Au(001) and MgO(001). Figure 1a shows a STM image of a 1.5° vicinal Au(001) surface with step edges perpendicular to the [110] direction showing regular monatomic steps. For the average step orientation perpendicular to the [100]-direction the steps have a zig-zag like shape as shown in Fig. 1b. Fe(001) grows in the bcc phase with a 45° rotation of its lattice on fcc Au(001) with a corresponding in-plane lattice mismatch of less than 1 %. Thus, the step edges of the Au(001) surface perpendicular to the [100]-direction correspond to step edges perpendicular to the [110] of the Fe film (in the following noted as $[110]_{Fe}$).

The magnetic anisotropies of the Fe films were derived at room temperature from the frequencies of the spin waves determined by means of Brillouin light scattering spectroscopy (BLS) [7, 8] and from the evaluation of hysteresis loops obtained with the magneto-optical Kerr effect

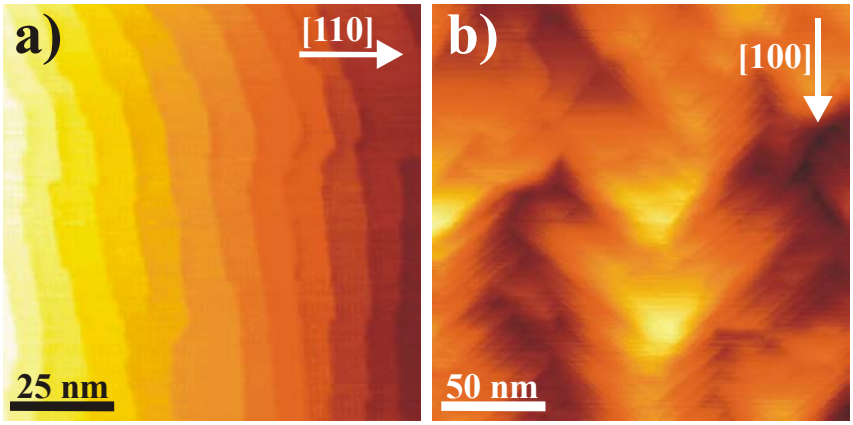

Fig. 1: a) STM image of a 4° vicinal Au layer with the miscut along the [100]-direction. b) STM image of a vicinal Au layer with a nominal miscut of 1.5° demonstrating monatomic steps perpendicular to the miscut orientation [110].

(MOKE) [9]. The Fe films were grown in the shape of a wedge, having the advantage that a large range of Fe thicknesses (typically 5 to 50 ML) is available on one sample by scanning the laser beam along the wedge. Due to the extremely small slope of the edge (2-3 ML mm^{-1}) the wedge shape of the Fe films does not influence the obtained results.

The total magnetic anisotropy energy density of a vicinal (001) film can be expressed by $E_{\mathrm{Ani}} = -K^{(2)}_{\mathrm{s,eff}} \cos^2\vartheta + K^{(4)}_{\mathrm{p,eff}} \sin^4\vartheta\cos^2\varphi\sin^2\varphi + K^{(2)}_{\mathrm{p,eff}} \sin^2\vartheta\cos^2(\varphi-\varphi_0)$ where $K^{(2)}_{\mathrm{p,eff}}$, $K^{(2)}_{\mathrm{s,eff}}$ and $K^{(4)}_{\mathrm{p,eff}}$ are the effective constants of the in- and out-of-plane uniaxial anisotropies and the in-plane fourfold anisotropy, respectively; ϑ and φ are the polar and the azimuthal angles of the magnetization, and φ_0 determines the orientation of the uniaxial in-plane easy axis with respect to those of the fourfold anisotropy. For $\varphi_0 = 0°$ both easy axes coincide, for $\varphi_0 = 45°$ the uniaxial easy axis is along one of the fourfold hard axes. In fact, all anisotropy constants can be determined by fitting the spin wave frequencies measured as a function of the in-plane angle of the applied external field H [6, 10]. In this investigation we will concentrate on the uniaxial in-plane anisotropy $K^{(2)}_{\mathrm{p,eff}}$, since the other two contributions do also exist in (001) films.

The second method for the determination of $K^{(2)}_{\mathrm{p,eff}}$ is to measure static magnetization loops with the magnetic field applied perpendicular to the easy axis [9]. This technique, however, becomes very insensitive, if the easy axis of the induced anisotropy does not coincide with one of the strong fourfold anisotropy of Fe ($[100]_{\mathrm{Fe}}$ or $[010]_{\mathrm{Fe}}$). This is the case for the samples with the average step orientation perpendicular to $[110]_{\mathrm{Fe}}$. For these samples BLS was only used for the determination of $K^{(2)}_{\mathrm{p,eff}}$. For the step orientation perpendicular to $[100]_{\mathrm{Fe}}$ both techniques have provided the same results within their error margins. The easy axis of the induced uniaxial anisotropy is either parallel or perpendicular to the steps, depending on the miscut angle, i.e, $\varphi_0 = 0°$ and $K^{(2)}_{\mathrm{p,eff}}$ is either negative or positive. Figure 2a shows the obtained results for $K^{(2)}_{\mathrm{p,eff}}$ as a function of the vicinal miscut angle for different thicknesses of the Fe films, illustrating the above fact. For small miscut angles $K^{(2)}_{\mathrm{p,eff}}$ is negative, and with increasing angle its absolute value first increases, reaches its maximum and then decreases, crossing zero at a critical miscut angle, α_c, which is almost independent of the film thickness. For higher miscut angles $K^{(2)}_{\mathrm{p,eff}}$ is positive and increases with α for small Fe film thicknesses. For thick films a maximum value for $K^{(2)}_{\mathrm{p,eff}}$ is reached at $\alpha \sim 4°$. To understand this fact the dependence of $K^{(2)}_{\mathrm{p,eff}}$ on the Fe film thickness was studied in detail. It is presented in Fig. 2b as a function of $1/d$ for a film with the miscut in the [100]-direction. For small miscut angles the measured dependence can be fitted by

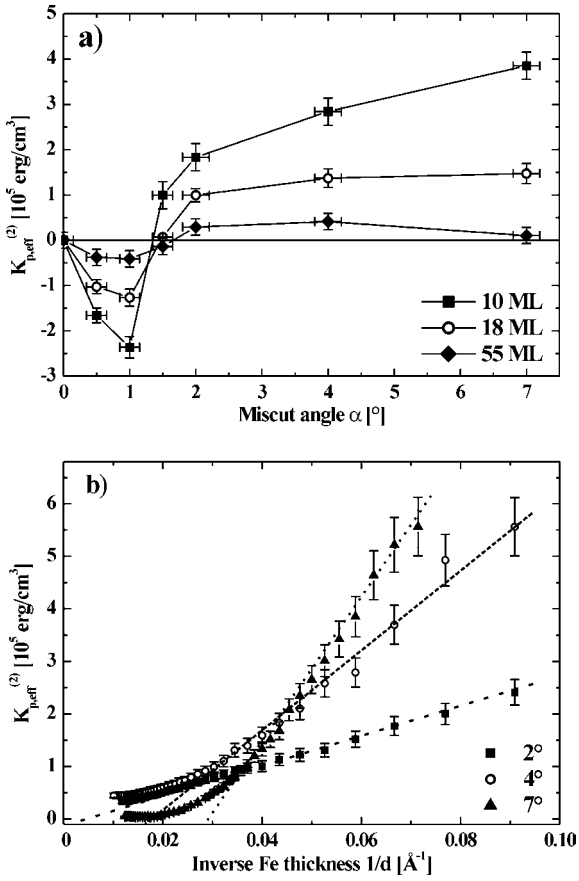

Fig. 2: a) $K_{\mathrm{p,eff}}^{(2)}$ vs. the vicinal miscut angle for different Fe thicknesses. Negative (positive) values of $K_{\mathrm{p,eff}}^{(2)}$ indicate an easy axis parallel (perpendicular) to the step edges. b) $K_{\mathrm{p,eff}}^{(2)}$ vs. the Fe thickness as a function of 1/*d* for a film with miscut in [100]-direction.

the usual expression $K_{\mathrm{p,eff}}^{(2)} = K_{\mathrm{p}} + \frac{2k_{\mathrm{p}}}{d}$, where K_{p} and k_{p} describe the quasi-volume and quasi-surface contributions, respectively. The curves obtained for higher miscut angles, however, indicate a clear critical thickness d_c, at which the above expression is not valid. It is also seen from Fig. 2b that d_c depends on the miscut angle. The existence of the critical thickness is apparently connected with the stress relaxation of the growing Fe film. In fact, due to a high out-of-plane mismatch of 42 % between the lattices of fcc Au and bcc Fe the Fe film grows at the beginning with an essential stress, which is relaxed for thicker films.

The obtained dependencies of K_{p} and k_{p} on the miscut angle are presented in Fig. 3 for both investigated orientations of the steps. For the Fe films with the average step orientation perpendicular to $[110]_{\mathrm{Fe}}$ the value of K_{p} increases proportionally to the miscut angle and thus the step density, reflecting a linearly growing stress in the films. The thickness independent (surface) contribution k_{p} is negligible. For the other orientation of the steps, i.e., the steps perpendicular to $[100]_{\mathrm{Fe}}$ K_{p} is roughly proportional to α^2 with the exception of the interval $\alpha < 1.5°$, where it is negative.

For a microscopic understanding of the uniaxial anisotropy both the relaxation of the in-plane mismatch of 1% by misfit dislocation formation and the relaxation of the perpendicular misfit of 42% must be taken into account. It is interesting to note, that the perpendicular misfit cannot be released by formation of a dislocation network. It is likely, that the interplay between both the in-plane and the out-of-plane relaxation causes the observed properties of the uniaxial anisotropy. Detailed numerical simulation are highly needed to clarify this point.

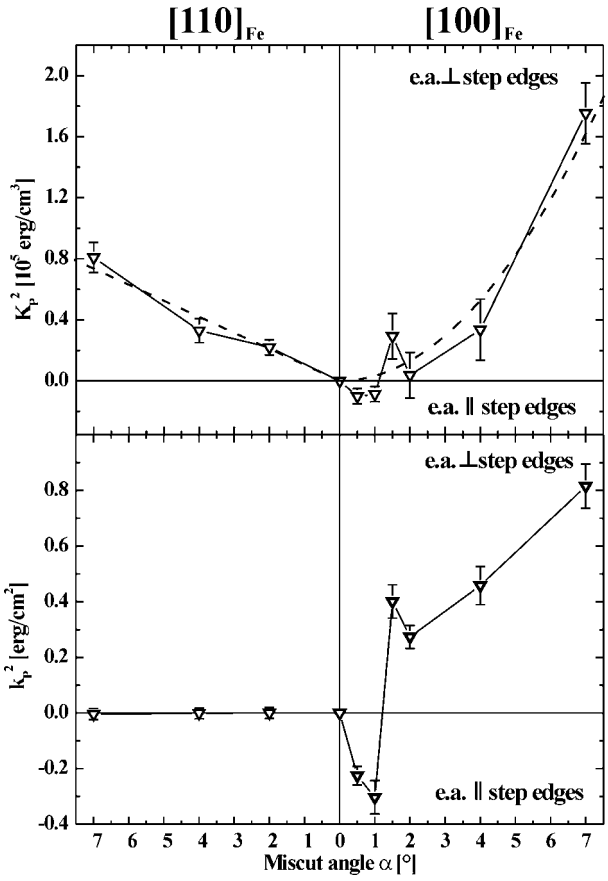

Fig. 3: Surface-like and volume-like contribution of the uniaxial in-plane anisotropy $K_{\mathrm{p,eff}}^{(2)}$ for $[100]_{\mathrm{Fe}}$- (right) and $[110]_{\mathrm{Fe}}$-orientation (left). Positive (negative) values of the anisotropy constant indicate an easy axis orientation perpendicular (parallel) to the step edges.

Support by the Deutsche Forschungsgemeinschaft and the ESF program NANOMAG is gratefully acknowledged.

References

[1] B. Heinrich, K.B. Urquhart, A.S. Arrott, J.F. Cochran, K. Myrtle, S.T. Purcell, Phys. Rev. Lett. **59**, 1756 (1987).
[2] B. Schulz, K. Baberschke, Phys. Rev. B **50**, 13467 (1992).
[3] D.S. Chuang, C.A. Ballentine, R.C. O'Handley, Phys. Rev. B **49**, 15084 (1994).
[4] M.L. Néel, J. Phys. Rad. **15**, 376 (1954).
[5] M. Rickart, B.F.P. Roos, T. Mewes, J. Jorzick, S.O. Demokritov, B. Hillebrands, Surf. Sci. in press.
[6] A. R. Frank, J. Jorzick, M. Rickart, M. Bauer, J. Fassbender, S.O. Demokritov, B. Hillebrands, M. Scheib, A. Keen, A. Petukhov, A. Kirilyuk, Th. Rasing, J. Appl. Phys. **87**, 6092 (2000).
[7] S.O. Demokritov, E. Tsymbal, J. Phys.: Cond. Mat. **6**, 7145 (1994).
[8] B. Hillebrands, *Brillouin light scattering from layered magnetic structures*, in: *Light scattering in Solids VII*, M. Cardona, G. Güntherodt (eds), Springer, Topics in Applied Physics, **75** (2000).
[9] W. Weber, R. Allenspach, A. Bischof, Appl. Phys. Lett. **70**, 520 (1997).
[10] B. Hillebrands, Phys. Rev. B **41**, 530 (1990).

6.12 Preparation and magnetic anisotropies of epitaxial Co(110) films on MgO(110) substrates

T. Mewes, H. Nembach, J. Fassbender, and B. Hillebrands

The demand for epitaxial films grown on non-conducting substrates becomes increasingly important. One issue is the preparation of smooth Cu films to be used as a growth template for ultrathin magnetic films. In contrast to the use of single crystalline Cu substrates, MgO substrates offer a number of advantages for the planned experiments in our laboratory: i) We plan to study the modification of anisotropies upon light-ion irradiation. Single crystalline Cu substrates would be damaged in these experiments so that a multiple usage of the substrate is not possible. ii) Time resolved Kerr effect investigations need a Cu buffer on an insulating substrate in order to fabricate strip lines on the sample by patterning, which are used to generate pulsed magnetic fields. The preparation of epitaxial films on non-conducting substrates is therefore a prerequisite for these investigations.

Recently a recipe for the growth of Cu buffer layers on MgO substrates has been developed by us for the (001)-orientation [1]. A similar method for the preparation of the (110)-orientation is the subject of this Section. The MgO(110) substrate was cleaned in isopropyl alcohol, and, after introduction in the ultrahigh vacuum system, it was heated to 400 K. In order to achieve a carbon free MgO(110) surface the substrate was exposed to a gas mixture of highly dissociated 40 % argon and 60 % oxygen ions with energies of 30 ± 3 eV. First, a 5 nm thick Pt layer was deposited at 725 K in order to mediate between the in-plane lattice spacings of the MgO substrate and the following Cu buffer layer. Then a 100 nm thick Cu layer is deposited at room temperature. A short annealing cycle at 920 K is performed to further increase the film quality. In order to avoid interface interdiffusion Co films of different thicknesses were deposited at room temperature. For protection purposes a 1.5 nm thick Cu and a 1.5 nm thick Cr capping layer were used.

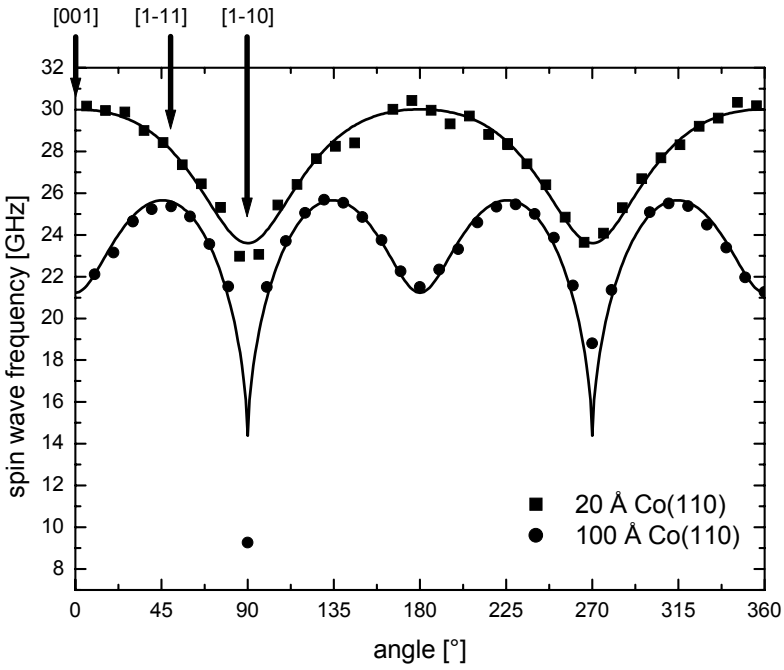

Fig. 1: Spin wave frequency as a function of the in-plane angle of the applied magnetic field for two different Co film thicknesses. The crystallographic in-plane directions are indicated. The solid lines are the result of a model fit described in the text.

Co film thickness [nm]	K_1 [erg/cm^3]	$K_{\text{in-plane}}$ [erg/cm^3]	$K_{\text{out-of-plane}}$ [erg/cm^3]
2	$-0.58 \pm 0.09 \times 10^5$	$-3.78 \pm 0.11 \times 10^5$	$9.50 \pm 0.11 \times 10^6$
10	$-8.32 \pm 0.65 \times 10^5$	$-6.17 \pm 0.95 \times 10^5$	$-3.08 \pm 0.23 \times 10^6$

Tab. 1 : Anisotropy values for two different Co film thicknesses determined by Brillouin light scattering spectroscopy.

The magnetic anisotropies were determined by means of Brillouin light scattering spectroscopy. In the crystallographic reference frame the free anisotropy energy is expressed as

$$F_{\text{ani}} = K_1\left(\alpha_{x'}^2\alpha_{y'}^2 + \alpha_{y'}^2\alpha_{z'}^2 + \alpha_{z'}^2\alpha_{x'}^2\right) + K_{\text{in-plane}}\alpha_x^2 - K_{\text{out-of-plane}}\alpha_z^2, \quad (1)$$

with K_1 representing the fourth order magnetocrystalline anistropy constant, and $K_{\text{in-plane}}$ and $K_{\text{out-of-plane}}$ representing two additional uniaxial anisotropy contributions of second order. $\boldsymbol{\alpha}$ is the direction unit vector of magnetization with components α_x, α_y and α_z expressed in the film coordinate system and $\alpha_{x'}$, $\alpha_{y'}$ and $\alpha_{z'}$ expressed in the crystallographic reference frame. All anisotropy constants contained in Eq. (1) are determined from dipolar spin waves propagating along the film plane (Damon-Eshbach modes) [2, 3].

The spin wave frequencies are measured as a function of the crystallographic in-plane direction of an applied field of 2 kOe, which is high enough to saturate the magnetization in the hard in-plane magnetization direction. The angular dependence of the spin wave frequencies for two different Co film thicknesses is shown in Fig. 1. The maxima and minima correspond to the easy and hard magnetization directions, respectively. In the case of the 2 nm thick Co film a clear twofold behavior is observed due to the magneto-elastic anisotropy contribution. For a 10 nm thick Co film the magneto-crystalline anisotropy contribution is dominant and therefore a pseudo-fourfold behavior is observed. As a function of Co thickness the easy magnetization direction changes from the [001]- to the [1-11]-direction. Thus the [001]-direction becomes magnetically an intermediate (middle hard) axis. For the two different Co film thicknesses the obtained anisotropy values are listed in Tab. 1. These values are in excellent agreement with those observed for Co(110) films deposited on Cu single crystal substrates [3]. The quality of the films and the resulting magnetic behavior of both types of films is therefore on the same high level. This allows the usage of MgO substrates for the investigation of epitaxial Co films.

T.M. acknowledges support by the Studienstiftung des deutschen Volkes.

References

[1] T. Mewes, M. Rickart, A. Mougin, S.O. Demokritov, J. Fassbender, B. Hillebrands, *Improved growth of smooth Cu(001) films on MgO(001)*, in: *Annual Report 2000*, B. Hillebrands (Ed.) page 51 (2000).
T. Mewes, M. Rickart, A. Mougin, S.O. Demokritov, J. Fassbender, B. Hillebrands, M. Scheib, Surf. Sci. **481**, 87 (2001).
[2] B. Hillebrands, Phys. Rev. B **41**, 530 (1990).
[3] J. Fassbender, G. Güntherodt, C. Mathieu, B. Hillebrands, R. Jungblut, J. Kohlhepp, M.T. Johnson, D.J. Roberts, G.A. Gehring, Phys. Rev. B **57**, 5870 (1998).

6.13 Growth of epitaxial NiFe/FeMn exchange coupled bilayers

T. Mewes, M. Rickart, H. Nembach, S.O. Demokritov, J. Fassbender, and B. Hillebrands

Since the exchange bias effect is an interfacial effect the structure of the interface between the ferromagnetic and antiferromagnetic layer is of large importance. In the case of polycrystalline layered systems the situation is further complicated by the presence of different grain sizes and grain orientations. Therefore, in order to gain a deeper understanding of the underlying microscopic origin of the exchange bias effect, well characterized epitaxial layered systems are needed.

By using the buffer layer system Fe(0.5 nm)/Pt(5 nm)/Cu(100 nm) on MgO(001) substrates it is possible to obtain a Cu(001) surface with a large lateral correlation length, low RMS-roughness and a small mosaicity suitable for growth of NiFe [1]. The quality of this Cu-surface can be further improved by carefully annealing the buffer layer at 900 K. A STM-image of the resulting atomically flat Cu(001) surface with large terraces and monoatomic steps in between is shown in Fig. 1.

In order to quantify the STM images the height-height correlation function $H(\mathbf{r}) = \langle[h(\mathbf{r})–h(\mathbf{0})]^2\rangle$ has been determined from the data using a procedure described in Ref. [2]. Here $h(\mathbf{r})$ is the surface height at position $\mathbf{r}$ of the surface. For a self-affine and isotropic surface $H(\mathbf{r})$ can be expressed as $H(r) = 2w^2[1 – \exp(–(r/\xi)^{2\alpha})]$, where α is the roughness exponent describing the texture of roughness, ξ is the lateral correlation length defining a typical lateral size of the roughness pattern, and w is the root-mean square (RMS) roughness [3]. The corresponding RMS roughness of the 0.2×0.2 μm^2 scan area of the Cu(001) surface shown in Fig. 1 is 0.14 nm. The roughness exponent α was determined from larger STM-images to be $\alpha = 0.7 \pm 0.1$, which corresponds to a smooth surface. Even for the largest possible scan area of 1×1 μm^2 the yielded value for the correlation length ξ is above the scan size.

A 5 nm thick NiFe(001) layer was subsequently grown at 370 K on top of the annealed Cu(001) layer. The LEED spots of this layer are rather narrow, indicating the good crystallographic structure of the surface. The morphology of this surface measured by STM (see Fig. 2) mainly consists of small islands, a fact which is also reflected in a small correlation length $\xi = 25$ nm.

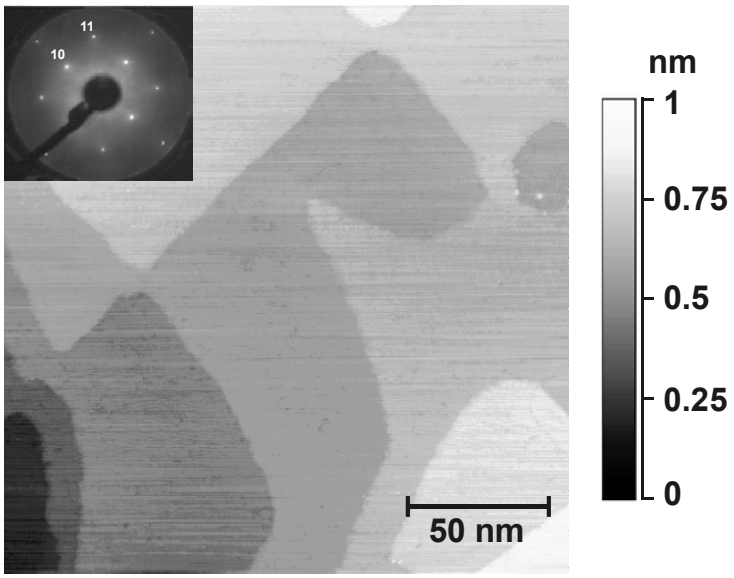

Fig. 1: STM image of MgO/Fe(0.5 nm)/Pt(5 nm)/Cu(100 nm), with a scan area of 0.2×0.2 μm^2. The inset shows the LEED pattern for a primary energy of 165 eV.

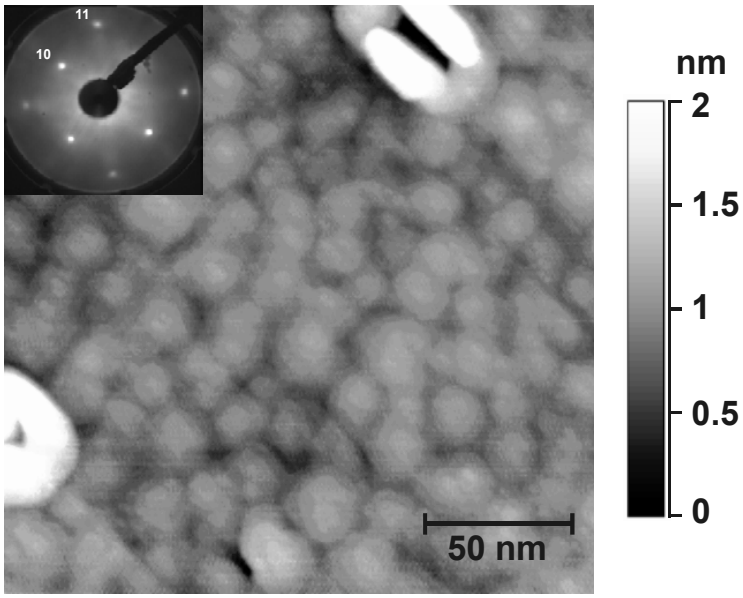

Fig. 2: STM image of MgO/Fe(0.5 nm)/ Pt(5 nm)/Cu(100 nm)/NiFe(5 nm), with a scan area of 0.2×0.2 μm^2. The inset shows the LEED pattern for a primary energy of 112 eV.

The RMS roughness of the 0.2×0.2 μm^2 scan area as shown in Fig. 2 is 0.3 nm. The low value of the roughness exponent $\alpha = 0.5 \pm 0.1$ determined from larger STM images is caused by the relatively jagged surface of NiFe. The characteristic volcano-like features, also referred to as 'pinholes', that can be seen in Fig. 2, are similar to those observed for the growth of Co on Cu(001) [4].

Subsequently a 10 nm thick FeMn(001) layer was deposited using a growth temperature of 370 K. The good crystallographic structure is evidenced by the LEED patterns shown in the inset of Fig. 3. The RMS roughness for a 0.2×0.2 μm^2 scan area of this layer is 0.7 nm (see. Fig. 3), which is larger than that of the NiFe layer. But the correlation length $\xi = 50 \pm 5$ nm as well as the roughness exponent $\alpha = 0.6 \pm 0.1$ are also increased compared to the NiFe surface, i.e., the surface of FeMn has a higher RMS roughness but is less jagged and consists of larger islands than its interface with NiFe. Therefore special caution has to be taken when the properties of interfaces are extrapolated from the properties of the corresponding surfaces of layered systems, as it is often done in the literature.

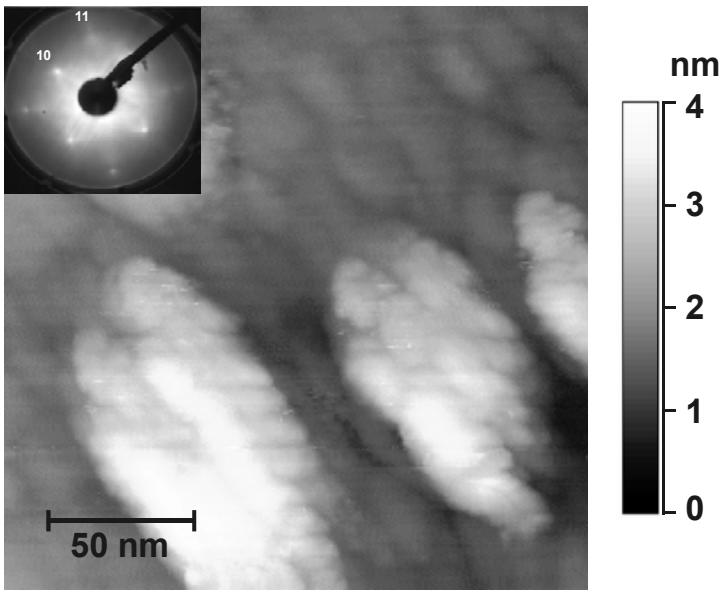

Fig. 3: STM image of MgO/ Fe(0.5 nm)/Pt(5 nm)/Cu(100 nm)/ NiFe(5 nm)/FeMn(10 nm), with a scan area of 0.2×0.2 μm^2. The inset shows the LEED pattern for a primary energy of 115 eV.

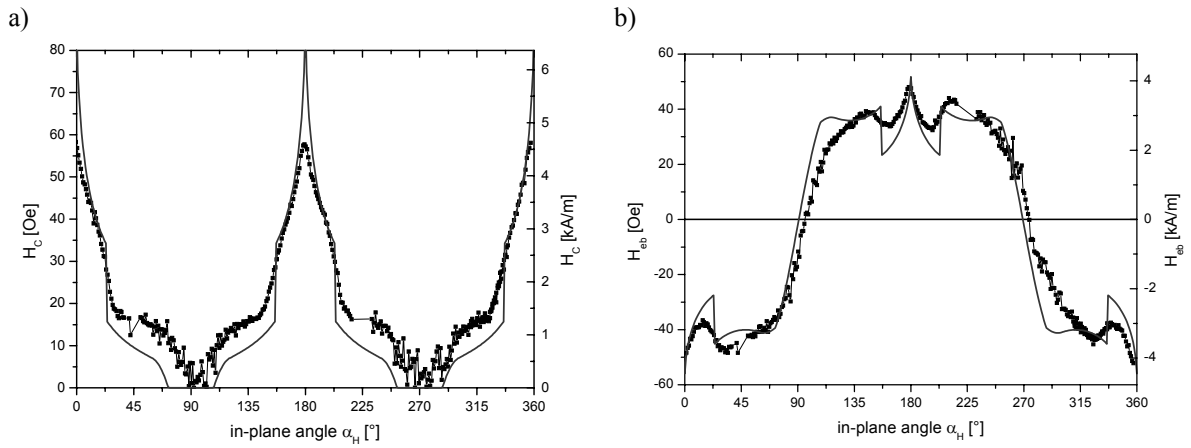

Fig. 4: Angular dependence of the coercivity field, H_C, a) and of the exchange bias field, H_{eb}, b) as derived from MOKE-measurements. In both plots the measured values (symbols) and fitted the curves, obtained using a free energy expression with unidirectional and fourfold anistropy constants, (lines) are shown.

From MOKE-measurements in longitudinal geometry the coercive fields for the decreasing and increasing field branch, $H_{C,\,left}$ and $H_{C,\,right}$ respectively, can be deduced. By varying the in-plane angle α_H of the applied field the angular dependence of the coercive field $H_C = (H_{C,\,right} - H_{C,\,left})/2$ and the exchange bias field $H_{eb} = (H_{C,\,right} + H_{C,\,left})/2$ can be derived. The corresponding data are shown in Fig. 4. The solid line represents a fit to the data using a free energy density assuming that only a unidirectional and fourfold anisotropy contribution is present:

$$f = -K_1 \cos(\alpha_M) + K_4 \sin^2(\alpha_M) \cos^2(\alpha_M)\,, \qquad (1)$$

where the in-plane angle α_M defines the orientation of the magnetization with respect to the [110]-direction of NiFe. K_1 and K_4 are the anisotropy constants of the unidirectional and four-fold anisotropy, respectively. The fit results in $K_1 = (4.6 \pm 0.1)\times 10^4$ erg/cm^3 and $K_4 = (3.8 \pm 0.1)\times 10^4$ erg/cm^3. Thus the easy axes of both anisotropies coincide. Both anisotropy contributions have the same order of magnitude. A quantitative comparison of the magnetization reversal data with a Stoner-Wohlfarth model is presented in Section 6.14.

T.M. acknowledges support by the Studienstiftung des deutschen Volkes.

References

[1] T. Mewes, M. Rickart, A. Mougin, S.O. Demokritov, J. Fassbender, B. Hillebrands, M. Scheib, Surf. Sci. **481**, 87-96 (2001).
[2] H.-N. Yang, Y.-P. Zhao, A. Chan, T.-M. Lu, G.-C. Wang, Phys. Rev. B **56**, 4224 (1997).
[3] S.K. Sinha, E.B. Sirota, S. Garoff, H.B. Stanley, Phys. Rev. B **38**, 2297 (1988).
[4] A.K. Schmid, D. Atlan, H. Itoh, B. Heinrich, T. Ichinokawa, J. Kirschner, Phys. Rev. B **48**, 2855 (1993).

D. Exchange Bias Effect

6.14 Phase diagrams of epitaxial exchange coupled NiFe/FeMn bilayers in the framework of the Stoner-Wohlfarth model

T. Mewes, H. Nembach, S.O. Demokritov, J. Fassbender, and B. Hillebrands

Epitaxial NiFe/FeMn exchange coupled bilayers have been prepared on MgO(001) substrates using the procedure described in detail in Section 6.13. To characterize the magnetic properties, often only the quantities coercive field, H_C, and exchange bias field, H_{eb}, are discussed which are inferred from only two points of the hysteresis curve, namely $H_{C,\,left}$ and $H_{C,\,right}$. Here we choose a detailed data representation for the longitudinal component of the magnetization taking the full information into account which is contained in the hysteresis loop. Examples are displayed in Figs. 1a and 1c. The data is represented in a two-dimensional graph with the angle of the applied field plotted along the *x*-axis and the strength of the field plotted along the *y*-axis. The gray value of each point is chosen proportional to the magnitude of the magnetization component parallel to the field, with the limiting values of white (black) indicating that the magnetization points exactly along the positive (negative) field direction. For both the decreasing and increasing field branch of the hysteresis curve a grayscale image is constructed. For the in-plane angles marked with the arrows A and B in Figs. 1a and 1c the hysteresis loops are shown in Fig. 2 to

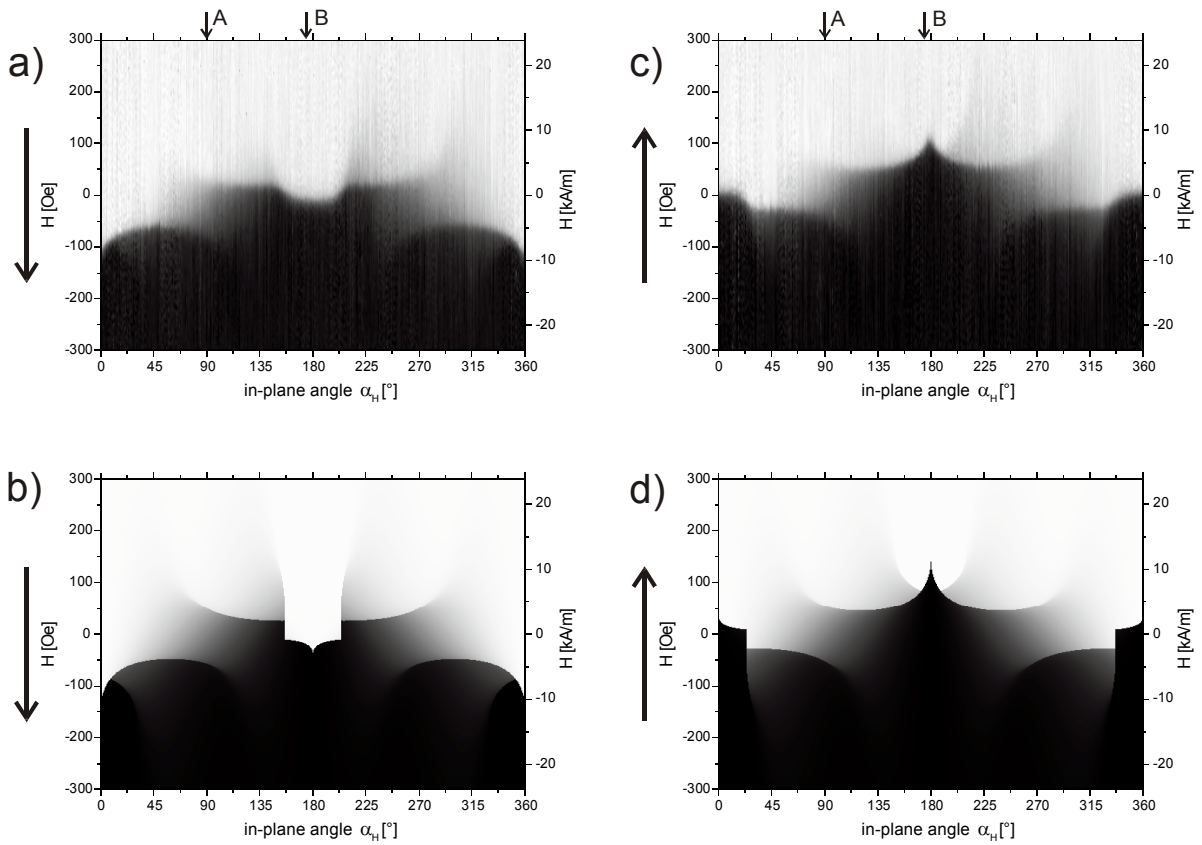

Fig. 1: Angular dependence of the longitudinal component of the magnetization for decreasing (a) and b)) and increasing field branch (c) and d)) of the hysteresis loop obtained experimentally (a) and c)) and theoretically within the Stoner-Wohlfarth model (b) and d)). The direction of the external field is plotted along the *x*-axis, and the field strength along the *y*-axis. The gray value is proportional to the value of the magnetization component parallel to the applied field. A detailed description is given in the text.

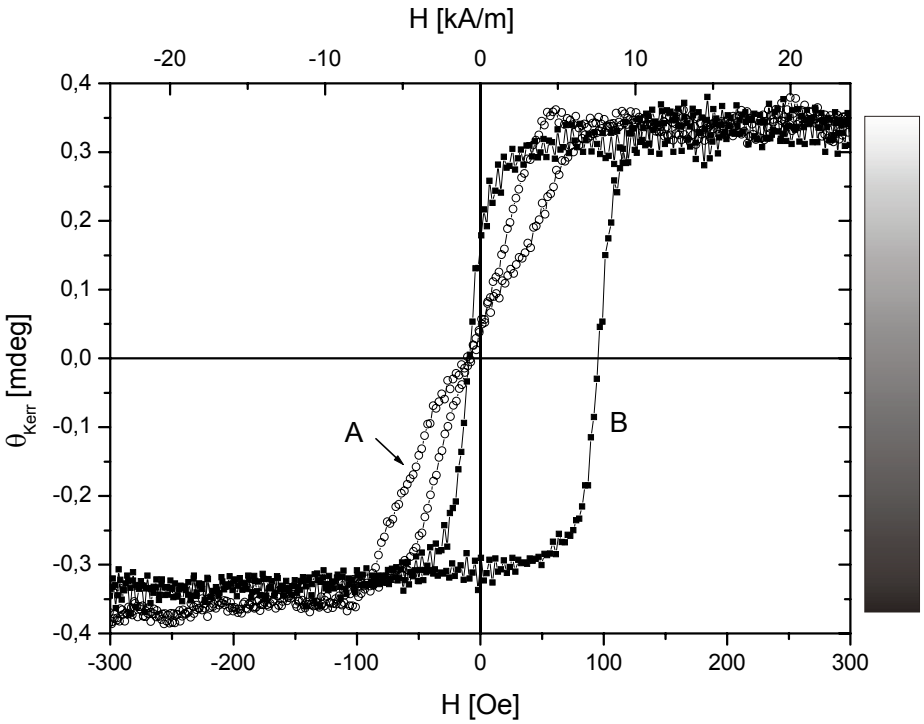

Fig. 2: Longitudinal component of the magnetization during magnetization reversal obtained experimentally by MOKE-measurements and corresponding gray scale values as used in Figs. 1 and 3. The in-plane angle is $\alpha_H = 175°$ for the closed symbols and $\alpha_H = 90°$ for the open symbols.

gether with the grayscale. The calculated angular dependencies predicted by the Stoner-Wohlfarth model using the so-called perfect delay convention [1] are displayed in Figs. 1b and 1d as a grayscale image as well. Here the free energy density is assumed to consist of a unidirectional and a four fold contribution only:

$$f = -K_1 \cos(\alpha_M) + K_4 \sin^2(\alpha_M) \cos^2(\alpha_M) , \tag{1}$$

where α_M is the angle of the magnetization with respect to the easy axis of the unidirectional anisotropy. The determination of the values of the in-plane uniaxial anisotropy constant $K_1 = (4.6 \pm 0.1) \times 10^4$ erg/cm^3 and the fourfold anisotropy constant $K_4 = (3.8 \pm 0.1) \times 10^4$ erg/cm^3 has been described in Section 6.13. By comparing Fig. 1a with Fig. 1b and Fig. 1c with Fig. 1d it is obvious that the overall angular dependence of the longitudinal component of the magnetization during magnetization reversal is very well described by Eq. (1). In Fig. 3 the results obtained from MOKE measurements for the transversal component of the magnetization are presented in a similar manner as in Fig. 1, but here the gray value is proportional to the magnitude of the magnetization component perpendicular to the applied field.

By comparing the experimental results with the theoretical predictions of the Stoner-Wohlfarth-type simulation it can be concluded that the overall angular dependence of the transverse component of the magnetization during magnetization reversal is correctly described within the Stoner-Wohlfarth model. The main differences that appear between experiment and the predictions are: i) Sharp edges occurring in the simulation are somewhat rounded out in the experiment. ii) The peak-like structure present in the decreasing (increasing) field branch at 180° (0°), that appears in Figs. 1b and 3b (Figs. 1d and 3d) is not observed in the experiment as can be seen in Figs. 1a and 3a (Figs. 1c and 3c). Interestingly this deviation appears in the regions near about 180° ± 20° and 0° ± 20° for which the Stoner-Wohlfarth model predicts a magnetization reversal for which the direction of rotation is the same for the increasing and decreasing field branch, i.e.,

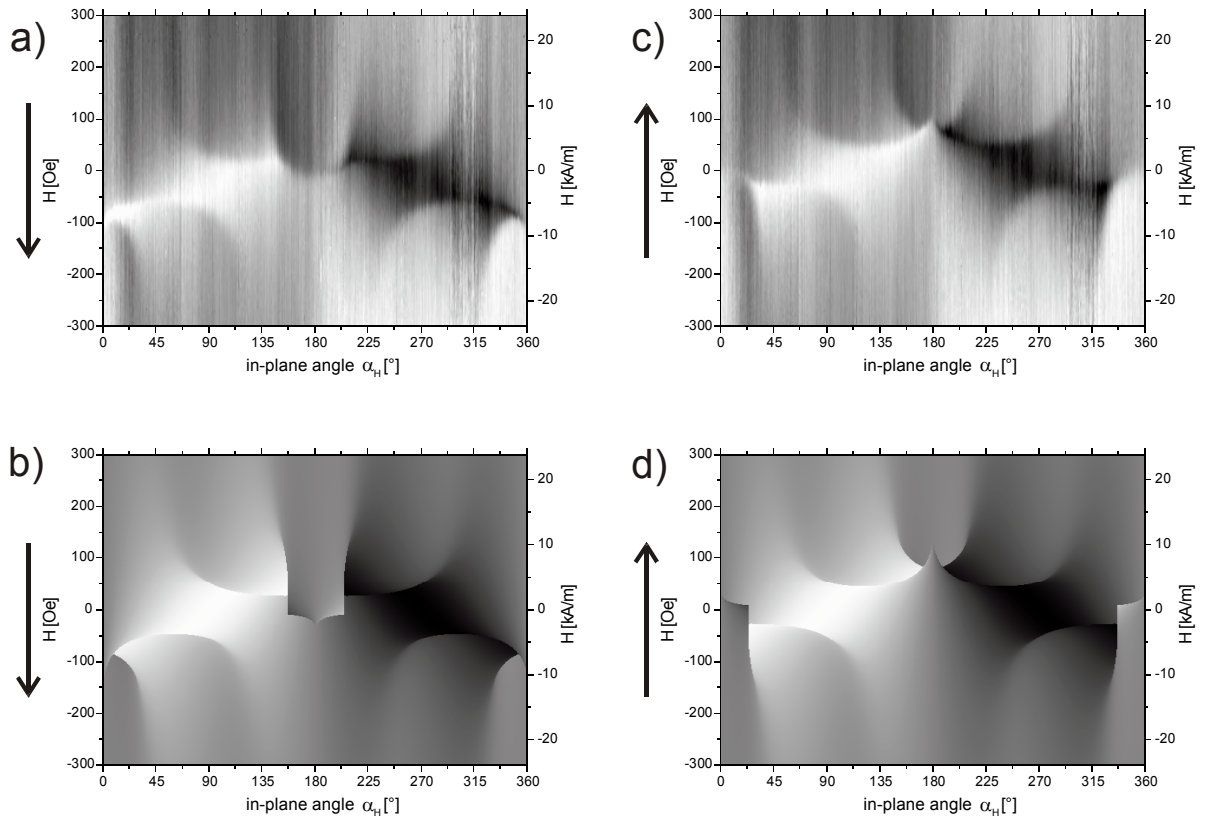

Fig. 3: Angular dependence of the transversal component of the magnetization for decreasing (a) and b)) and increasing field branch (c) and d)) of the hysteresis loop obtained experimentally (a) and c)) and theoretically within the Stoner-Wohlfarth model (b) and d)). The direction of the external field is plotted along the *x*-axis, and the field strength along the *y*-axis. Contrary to Fig. 1 the gray value here is proportional to the value of the magnetization component *perpendicular* to the applied field. Further description is given in the text.

the magnetization would rotate by 360° during a complete hysteresis loop. However, this kind of behaviour is not observed in the experiment.

The angular dependence shown in Fig. 1 and Fig. 3 can be summarized in a phase diagram as displayed in Fig. 4a. This representation is similar to the phase diagrams discussed for uniaxial ferromagnets [2, 3] but focused on the angular dependence. In the phase diagram of Fig. 4a the grayscale represents the direction of the magnetization in the global minimum of the free enthalpy. This direction together with the direction for all other minima of the free enthalpy is a indicated by small arrows in Fig. 4a. In order to better distinguish between the different regions of the phase diagram where one, two, three or even four minima exist in the free enthalpy, different gray values are used for these regions in the schematic phase diagram in Fig. 4b, and the regions are labeled A, B, C and D accordingly. By comparing the angular dependence of the longitudinal and transversal component of the magnetization during reversal (Figs. 1 and 3) with the phase diagram given in Fig. 4 the crucial role of the phase boundaries separating the regions with different numbers of minima of the free enthalpy becomes obvious.

T.M. acknowledges support by the Studienstiftung des deutschen Volkes.

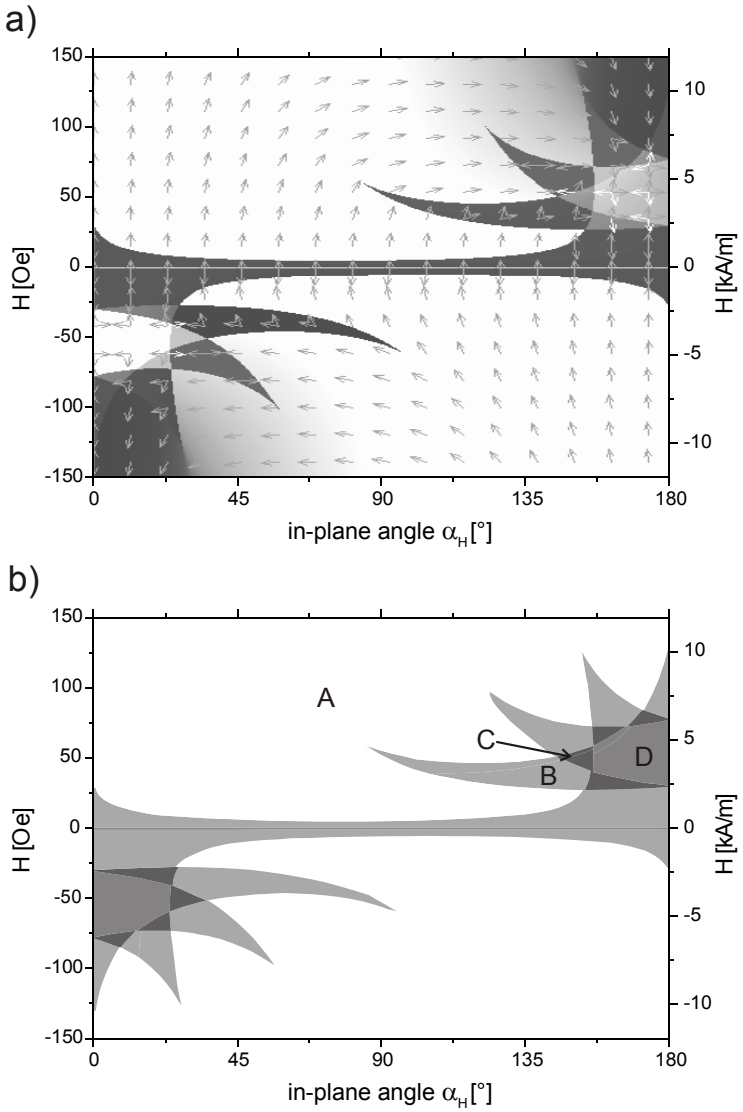

Fig. 4: Phase diagram for a system with unidirectional and four fold anisotropy contribution, ($K_1 = 4.63\times10^4$ erg/cm^3 and $K_4 = 3.76\times10^4$ erg/cm^3) to the free energy. The arrows in a) indicate the direction of the magnetization in the minima of the free enthalpy. In b) the regions for which there exist one, two, three or four minima have been labeled A, B, C and D, respectively.

References

[1] S. Nieber, H. Kronmüller, Phys. Stat. Sol. (b) **165**, 503 (1991).
[2] Y.T. Millev, H.P. Oepen, J. Kirschner, Phys. Rev. B, **57**, 5837 (1998).
[3] Y.T. Millev, H.P. Oepen, J. Kirschner, Phys. Rev. B, **57**, 5848 (1998).

6.15 Tuning exchange bias and coercive fields in ferromagnet/antiferromagnet bilayers with ion irradiation

J. Juraszek, S. Poppe, T. Mewes, J. Fassbender, and B. Hillebrands[1]

Recently, He ion irradiation was used to tune both magnitude and direction of the exchange bias field in NiFe/FeMn bilayers [1, 2]. Exchange bias in general results from the exchange coupling at the interface between a ferromagnetic (F) and an antiferromagnetic (AF) layer. If the sample is grown in a magnetic field, or field cooled from above the Néel temperature, a unidirectional anisotropy can be induced. This anisotropy acts as an internal field, the so-called exchange bias field H_{eb}, shifting the magnetization curve from $H = 0$ along the field axis. In addition an increase of the coercive field H_c is usually found. One of the main applications of the exchange bias effect is to provide a pinned magnetic layer in magnetic memory cells or magnetoresistive sensors.

In the present study, the sensitivity to light ion irradiation of different metallic Mn-based antiferromagnets is investigated. Thin permalloy ($Ni_{81}Fe_{19}$) films are exchange coupled to both structurally disordered (FeMn and CrMn) and ordered (PtMn) AF alloys. FeMn is one of the most extensively studied AF materials, but its low corrosion resistance and low thermal stability impedes its application in sensor devices. Better corrosion resistance is obtained with CrMn, but large thicknesses are required to induce an exchange bias field due to the weak anisotropy [3]. A small amount of metallic additives (e.g. Pt) can be used to improve the exchange bias properties in this system [4]. Finally, PtMn has a good corrosion resistance [5], high Néel temperature and large exchange coupling for small layer thicknesses. However, thermal processes are necessary to obtain long range chemical ordering of the antiferromagnetic γ-phase [6, 7].

All samples were prepared by thermal evaporation in an UHV system with background pressure of 5×10^{-10} mbar. Thermally oxidized Si(111) substrates with a 15 nm thick Cu buffer layer are used as growth templates. The $Ni_{81}Fe_{19}$ layer (5 nm) and the AF (10 nm) layer were deposited on top, with AF referring to $Fe_{50}Mn_{50}$, $Pt_{50}Mn_{50}$, and $Cr_{50}Mn_{50}$. All AF layers have the same thickness, although this parameter may need to be optimized for applications. $Ni_{81}Fe_{19}$ films were evaporated from the bulk NiFe alloy while the AF films were co-evaporated from elemental sources. The composition of the films and the layer thicknesses were carefully controlled by measuring the deposition rates (0.01 nm/s for all magnetic elements) using calibrated quartz microbalances, and controlled by Auger spectroscopy. All films were grown at room temperature, except PtMn which was deposited at 200 °C. This was found to enhance the exchange bias, presumably because of a higher degree of chemical ordering of the alloy [6]. Finally, a 3 nm thick Cr capping layer was deposited for protection purpose. After completion of growth a field annealing procedure was performed. The FeMn, CrMn and PtMn samples were heated up to 200 °C, 250 °C, and 500 °C, respectively, which is above the respective blocking temperatures. Subsequently they were cooled down to room temperature in an applied field H_{prep} of 500 Oe in order to establish the exchange bias direction. Ion irradiation experiments were performed at room temperature using a 10 keV He^+ beam produced by a Penning type source. A low current density of 6 μA/cm^2 was used in order to avoid sample heating. The dose range 10^{13}–10^{15} ions/cm^2 was achieved by varying the irradiation time. Different ion doses were achieved on the same sample by irradiating several stripes on the sample area. During irradiation, an external field was applied parallel (H_p) or antiparallel (H_{ap}) to the direction of H_{prep}. The magnetic prop

[1] In collaboration with D. Engel, A. Kronenberger, A. Ehresmann, H. Schmoranzer, Fachbereich Physik, Universität Kaiserslautern, Germany.

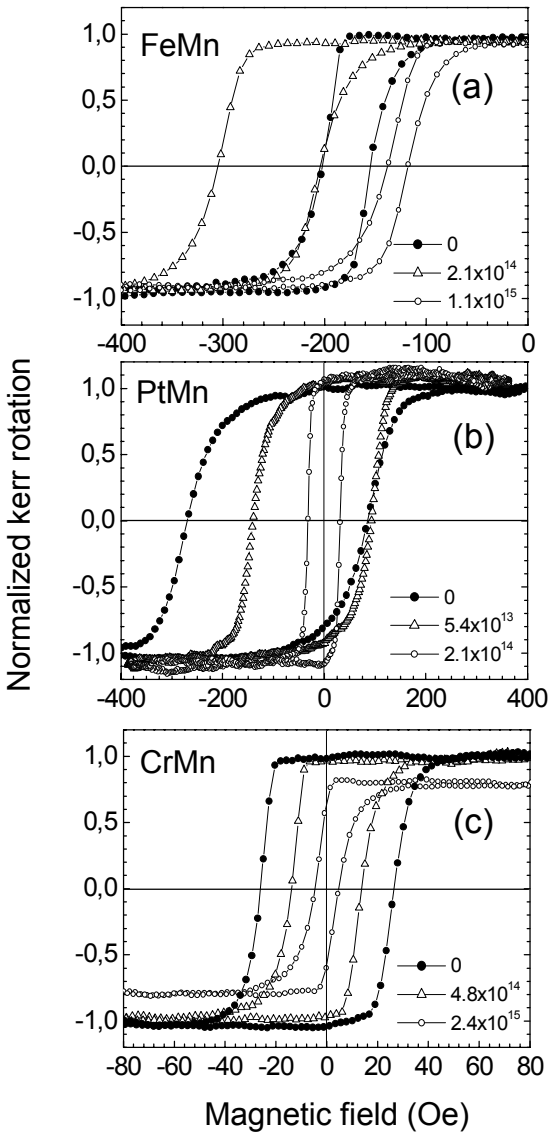

Fig. 1: Hysteresis loops of a NiFe layer exchange coupled to a FeMn (a), PtMn (b) and CrMn (c) layer before and after He ion irradiation. Different irradiation doses are indicated in the figure in units of ions/cm^2. Note the different field-scales.

erties of the samples were investigated before and after irradiation by longitudinal magneto-optical Kerr effect (MOKE) magnetometry at room temperature.

Figure 1 shows MOKE hysteresis curves of the as-deposited and ion irradiated samples in the H_p geometry for various ion doses. The Kerr rotation for the different AF systems is normalized to that of the samples prior to ion irradiation. First, the magnetization reversal for the non irradiated samples are described. The hysteresis curve for NiFe exchange coupled to FeMn exhibits an exchange bias field of -175 Oe and a coercive field of 30 Oe, which is considerably enhanced compared to that of a single permalloy film ($H_c \approx 2 - 3$ Oe). For MnPt an exchange bias field of -95 Oe is found. The corresponding coercivity (195 Oe) is much higher than in the case of FeMn. For CrMn no loop shift is observed. The AF layer thickness in this case is too small to induce an exchange bias field. However, a local exchange coupling across the F-AF interface is evidenced by an enhanced coercivity of $H_c = 26$ Oe of the NiFe film covered with CrMn compared to the single permalloy layer.

After ion irradiation, two distinct features depending on the ion dose are observed for the FeMn system, which were presented in detail in Ref. [2]. For a dose of 2.1×10^{14} ions/cm^2, the loop is shifted towards higher negative fields indicating an enhancement of the exchange bias effect (cf.

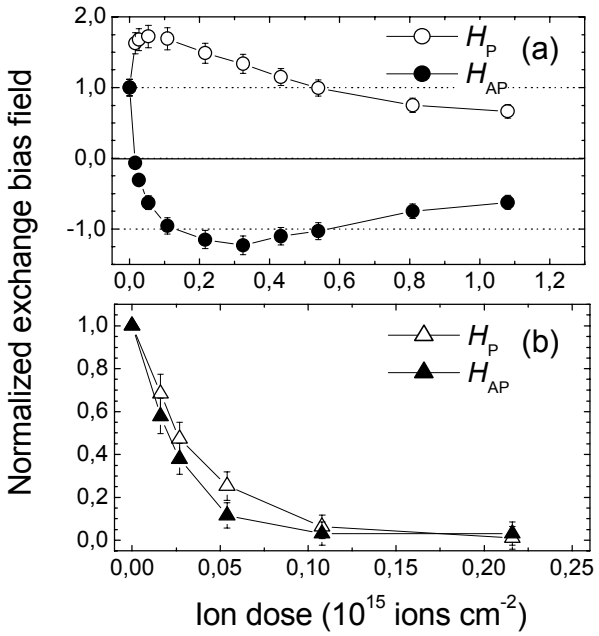

Fig. 2: Exchange bias field H_{eb} normalized to the initial value prior to ion irradiation as a function of ion dose for irradiation in an applied field parallel (H_p, open symbols) and antiparallel (H_{ap}, full symbols) to the preparation field (H_{prep}) direction. In a) FeMn and in b) PtMn is used as the AF material.

Fig. 2 a) as a result of ion irradiation. A maximum enhancement by a factor of 1.8 is observed. For higher ion doses the exchange bias field is decreased and finally completely suppressed. If a magnetic field during irradiation is applied antiparallel to the preparation field direction (H_{ap} geometry), the sign of H_{eb} can be changed. The maximum enhancement of absolute H_{eb} in the H_{ap} geometry is slightly reduced compared to the H_p configuration.

In the case of NiFe exchange coupled to PtMn, only a reduction of the exchange bias field is observed after irradiation (Fig. 2 b). Very low ion doses as small as 1×10^{14} ions/cm^2 are sufficient to completely suppress the exchange bias field. This is the same dose which corresponds to the maximum enhancement observed in the case of FeMn AF layers. In addition the overall course of the exchange bias field as a function of ion dose is not influenced by the applied field during irradiation, i.e., the exchange bias direction cannot be modified. It is clearly demonstrated that the exchange bias field in the PtMn system is very sensitive to light ion irradiation.

The origin of the different behavior in FeMn and PtMn systems can be attributed to the structural ordering in the latter case. For low ion doses defects created in the AF bulk act as pinning sites. Therefore the number of domain walls and domains present for an irradiated sample is increased compared to the non irradiated case which results in an enhancement of the exchange bias field according to Malozemoff's model [8]. This effect governs the low ion dose regime in the case of FeMn. If the field during irradiation is applied antiparallel to the preparation field direction, the creation of AF bulk defects is also responsible for the change of the pinning direction [2]. In the case of PtMn the situation is different. Only the ordered phase of PtMn is antiferromagnetic [9], whereas the disordered phase is ferromagnetic [10]. Hence a structural disordering of the AF material causes a weakening of the AF and therefore a reduction of the exchange bias effect. This effect is much stronger than that observed in the case of the FeMn system. This interpretation is further supported by the fact, that the exchange bias field direction cannot be chosen with the field applied during irradiation. The reduction of the exchange bias field due to structural disordering masks the effect of domain creation.

The ion dose dependence of the coercive fields for the different AF materials is shown in Fig. 3. In the case of the FeMn and the PtMn system the course of the coercive field is similar to that of the exchange bias field. For the FeMn system an initial increase in coercivity is followed by a successive decrease. For the PtMn system the coercive field decreases more rapidly. As for the

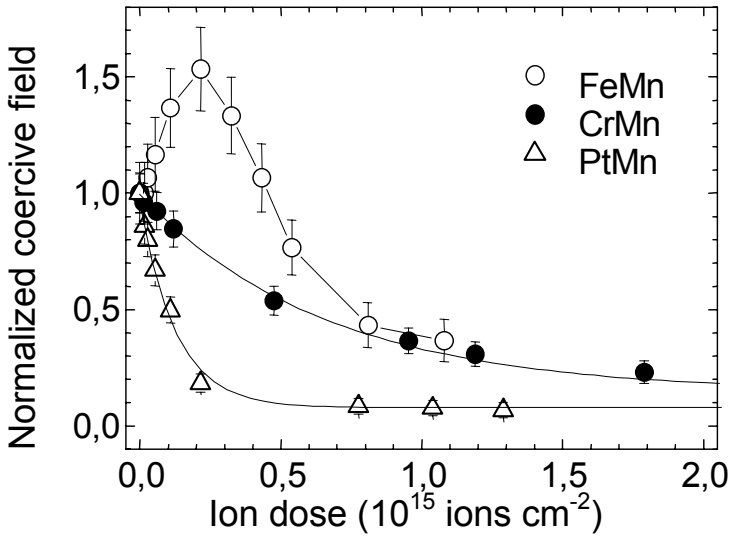

Fig. 3: Normalized coercive field, H_c, as a function of the ion dose for FeMn, CrMn and PtMn as the AF material in contact to FeNi.

exchange bias effect the ion dose required to completely suppress the effect of the AF layer on the coercive field is largely reduced compared to the FeMn system. For the CrMn system the as-prepared coercive field is enlarged although no exchange bias field is observed. This coercive field can then be reduced by ion irradiation. The dose required to completely suppress the AF layer induced coercivity enhancement is comparable to that of the FeMn system. Since CrMn like FeMn are both structurally disordered alloys a similar behavior is to be expected. Nevertheless, an initial increase in coercivity in the case of CrMn has not been observed. The magnetic behavior of the PtMn system however is completely different since it is governed by the crossover from a structural ordered (as-prepared) to a slightly disordered (after ion irradiation) alloy.

Work supported by the Deutsche Forschungsgemeinschaft, the Studienstiftung des deutschen Volkes, the EC-TMR program "DYNASPIN" No. FMRX-CT97-0124 and the UK EPSRC.

References

[1] T. Mewes, R. Lopusnik, J. Fassbender, B. Hillebrands, M. Jung, D. Engel, A. Ehresmann, H. Schmoranzer, Appl. Phys. Lett. **76**, 1057 (2000).
[2] A. Mougin, T. Mewes, M. Jung, D. Engel, A. Ehresmann, H. Schmoranzer, J. Fassbender, B. Hillebrands, Phys. Rev. B **63**, 060409(R) (2001).
[3] S. Soyea, H. Hoshiya, M. Fuyama, S. Tadokoro, J. Appl. Phys. **80**, 1006 (1996).
[4] S. Soyea, H. Hoshiya, R. Arai, M. Fuyama, J. Appl. Phys. **81**, 6488 (1997).
[5] H. Xi, B. Bian, D.E. Laughin, R.M. White, J. Appl. Phys. **87**, 4918 (2000).
[6] R.F.C. Farrow, R.F. Marks, S. Gider, A.C. Marley, S.S.P. Parkin, D. Mauri, J. Appl. Phys. **81**, 4986 (1997).
[7] K.M. Krishnan, C. Nelson, C. J. Echer, R.F.C. Farrow, R.F. Marks, A.J. Kellock, J. Appl. Phys. **83**, 6810 (1998).
[8] A.P. Malozemoff, Phys. Rev. B **35**, 3679 (1987).
[9] *Magnetic properties of metals: d-elements, alloys, and compounds,* H.P.J. Wijn (Ed.), Springer-Verlag, New York, page 79 (1991).
[10] C.S. Severin, C.W. Chen, J. Appl. Phys. **49**, 1693 (1978).

6.16 Magnetization reversal of exchange bias double layers magnetically patterned by ion irradiation

J. Fassbender, S. Poppe, T. Mewes, A. Mougin, and B. Hillebrands[1]

For technological applications a local reversal of the exchange bias direction is very important [1]. In order to investigate the minimum distance between locally reversed exchange bias directions, magnetically patterned samples have been fabricated and inspected by means of Lorentz microscopy.

As a model system polycrystalline $Ni_{81}Fe_{19}$ layers exchange biased by $Fe_{50}Mn_{50}$ layers have been used. The preparation of these bilayers is described in Section 6.15. Instead of SiO_2 substrates, 40 nm thick electron transparent Si_3N_4 membranes (100×100 μm^2) released in a Si wafer especially suited for transmission electron microscopy have been used [2]. After preparation the samples were covered with a 700 nm thick polymethylmethacrylate (PMMA) layer, which stops the He ions during irradiation completely [3]. Nanostructures of different size and geometry were patterned by electron beam lithography in the resist layer. The development of the PMMA resist in combination with homogeneous ion irradiation allows a local modification of the exchange bias layers [4]. In the regions where the PMMA resist is removed the He ions exhibit a penetration depth of 90 nm, i.e., they stop deep in the substrate [3]. After lithography the samples have been irradiated with an ion dose of 8×10^{13} ions/cm^2 in an applied field antiparallel to the preparation field direction. The area which has not been irradiated exhibits an exchange bias field of -105 Oe, whereas an irradiation dose of 8×10^{13} ions/cm^2 corresponds to an exchange bias field of about +175 Oe. The ion dose was chosen to observe a maximum exchange bias field in the opposite direction. The width of both hysteresis curves is about 50 Oe and 80 Oe, respectively. Hence a net magnetization of zero should be expected at –125 Oe and –75 Oe in the case without irradiation and at +135 Oe and +215 Oe in the irradiated area. For magnetization reversal involving the formation of a multi-domain structure, as is the case here, the zero net magnetization state corresponds approximately to the state of highest domain wall density and contrast.

First, Fresnel images of an irradiated square area of size 20×20 μm^2 as displayed in Fig. 1 will be discussed. In an applied magnetic field of –350 Oe the whole film is in a single domain state and a uniform gray level is observed. Increasing the field to –130 Oe a ripple contrast arising from a non uniform magnetization distribution in the non irradiated area is observed. At –70 Oe the high density of high contrast domain walls indicates that the net magnetization of the non irradiated area is close to zero. The irradiated square has not changed so far. At an applied field of +10 Oe no domains but a slight ripple contrast is observed. Both areas are single domain but antiparallel to each other, as indicated by the presence of domain walls on the upper and lower edges of the square area. Increasing the applied field further to +217 Oe a partial magnetization reversal of the irradiated square is observed via maximum domain wall density and contrast. A few non reversed domains remain at +251 Oe, and the image at +460 Oe shows complete saturation. Decreasing the applied magnetic field again the magnetization reversal of the irradiated square takes place at about +131 Oe, whereas that of the non irradiated area lies between –111 and –131 Oe. The magnetization state observed in the Fresnel images are in good agreement with those expected from hysteresis measurements. Thus, on this lateral scale, irradiation in an applied field leads to an enhanced exchange bias field with reversed sign.

[1] In collaboration with D. Engel, M. Jung, A. Ehresmann, H. Schmoranzer, Fachbereich Physik, Universität Kaiserslautern, Germany; G. Faini, Laboratoire de Photonique et de Nanostructures, Bagneux, France; and K.J. Kirk and J.N. Chapman, University of Glasgow, U.K.

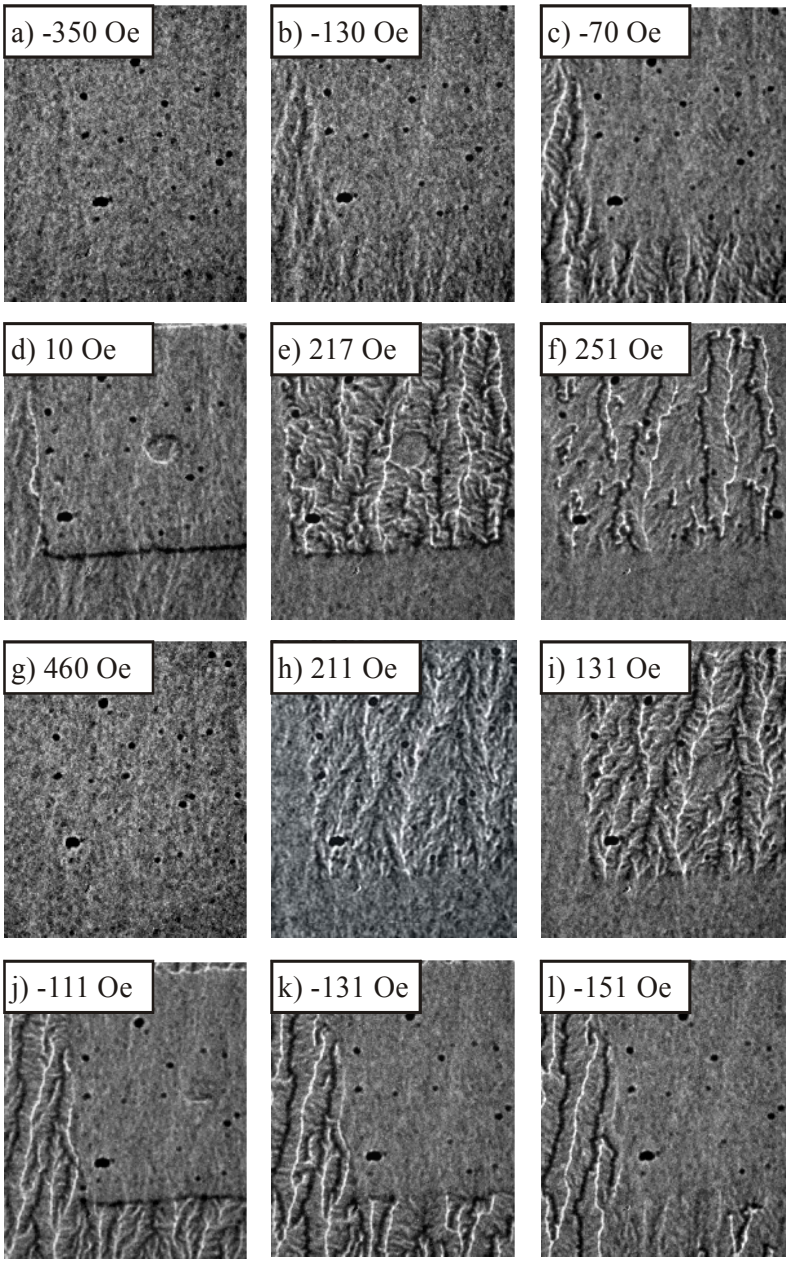

Fig. 1: Fresnel images at different applied fields as indicated in the figure for a full hysteresis cycle (a – l). The square (20×20 μm^2) is irradiated with an ion dose of 8×10^{13} ions/cm^2 in an applied field antiparallel to the preparation field direction. The surrounding area has been protected from the ion irradiation with a PMMA resist and therefore is not altered by the irradiation. The exchange bias direction is along the horizontal border of the square. The magnetic field values excited by a current through the standard objective lens are calibrated by Kerr magnetometry data of the non irradiated area.

In order to study the size and shape dependence of this magnetic patterning process, 0.5 μm wide, 0.5 – 12 μm long rectangles oriented parallel and perpendicular to the exchange bias direction have been fabricated. In addition long isosceles triangles are patterned. An atomic force microscopy image of the whole structure patterned in PMMA is shown in Fig. 2a. The corresponding Fresnel image is shown in Fig. 2b. The applied field of +10 Oe is chosen to have an antiparallel alignment of irradiated and non irradiated areas.

Several remarkable features are observed. First of all, only features with the long axis oriented parallel to the exchange bias direction are clearly visible. These structures are essentially single domain with some additional ripple contrast. The irradiation reproduces the PMMA pattern very well. On initial inspection, before application of an in-plane field, the sample showed magnetic contrast with the patterned features perfectly reproduced. Nevertheless, after application of an in-plane field the magnetic features observed are without sharp edges and show rounded ends. This can be understood as follows. The creation of a domain wall contributes to the free energy of the system due to the exchange coupling within the ferromagnetic layer. Since the domain

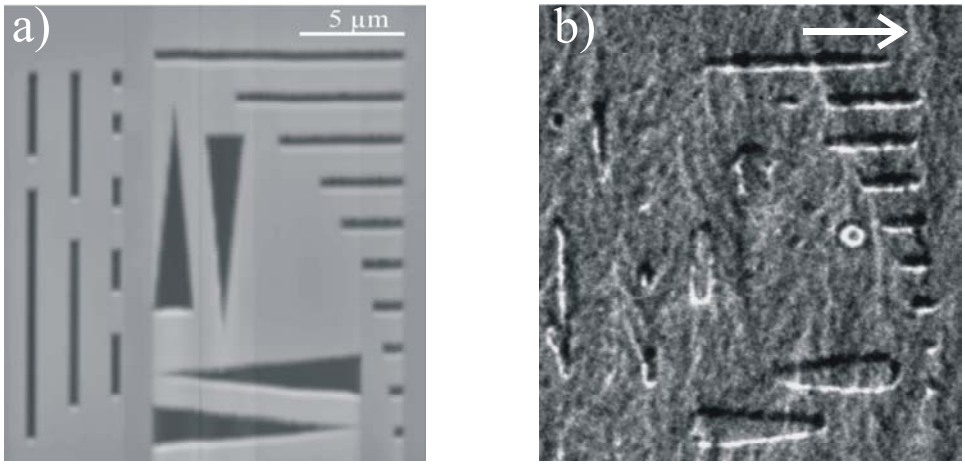

Fig. 2: a) Atomic force microscopy image of a PMMA resist pattern which has been used for the ion irradiation patterning. The rectangles are 0.5 µm wide and 0.5 – 12 µm long. The long axes of the horizontal rectangles are parallel to the exchange bias direction. The ion dose used for patterning is 8×10^{13} ions/cm^2 with a field applied antiparallel to the preparation field direction. b) Corresponding Fresnel image at an applied field of +10 Oe (comparable to Fig. 1d). The white arrow indicates the exchange bias direction.

wall energy is proportional to its length short domain walls are energetically favorable. On the other hand if the domain wall is shortened (e.g. rounded ends of the triangles) there exist areas where the magnetization is oriented antiparallel to the exchange bias field direction. This process increases the contribution to the free energy of the system due to the exchange coupling between the ferromagnetic and the antiferromagnetic layer and therefore favors minimization of these areas. Thus the resulting domain pattern is due to a competition between both effects which minimizes the free energy of the whole system.

The rectangles oriented perpendicular to the exchange bias direction show a more complicated behavior. Within one rectangle there coexist regions with the magnetization parallel and antiparallel to that of the surrounding area. For perfect antiparallel alignment one would find a large length of pattern boundary where the magnetization meets head-on [5]. Due to the large dipolar energy this is energetically unfavorable and thus the creation of domain walls in these small structures is suppressed to a large degree. The critical size for that behavior is about 700 nm. A full hysteresis cycle (not shown) shows for the structures oriented parallel to the exchange bias direction a magnetization reversal behavior that is similar to that of the 20×20 µm^2 square shown in Fig. 1. For structures oriented perpendicular to the exchange bias direction the interpretation is more difficult and further investigation is required.

Work supported by the Deutsche Forschungsgemeinschaft, the Studienstiftung des deutschen Volkes, the EC-TMR program "DYNASPIN" No. FMRX-CT97-0124 and the UK EPSRC.

References

[1] J. Daughton, J. Brown, E. Chen, R. Beech, A. Pohm, W. Kude, IEEE Trans. Magn. **30**, 4608 (1994).
[2] M. Rührig, B. Khamsehpour, K.J. Kirk, J.N. Chapman, P. Aitchinson, S. McVitie, C.D.W. Wilkinson, IEEE Trans. Magn. **32**, 4452 (1996).
[3] SRIM 2000 code, J. F. Ziegler, J.P. Biersack, U. Littmark, *The Stopping and Range of Ions in Solids*, Pergamon, New York, Oxford (1985).
[4] A. Mougin, S. Poppe, J. Fassbender, B. Hillebrands, G. Faini, U. Ebels, M. Jung, D. Engel, A. Ehresmann, H. Schmoranzer, J. Appl. Phys. **89**, 6606 (2001).
[5] M.F. Gillies, J.N. Chapman, J.C.S. Kools, J. Appl. Phys. **78**, 5554 (1995).

6.17 Advanced method for the fabrication of a Wheatstone bridge type spin-valve sensor element

T. Mewes, J. Fassbender, and B. Hillebrands[1]

Nowadays an increasing number of applications rely on the giant magneto-resistance effect (GMR). In magnetic read heads of hard disk drives GMR is commonly used [1]. Magnetic sensors for the automotive industry currently use the anisotropic magneto-resistance effect. Due to a higher signal level and thus increased specification tolerances GMR technology will probably enter the next generation of these devices. The sensor consists of two ferromagnetic layers which are separated by a metallic, non-magnetic layer. In angle sensing elements one ferromagnetic layer is fixed in its magnetization direction whereas the second one is free to follow any external in-plane field direction. One possibility to pin the magnetization direction of a ferromagnetic layer is to use exchange coupling to an adjacent antiferromagnetic layer. These layer structures are called spin-valve systems.

In order to achieve thermal drift compensation spin-valve sensor devices are commonly designed in a Wheatstone bridge configuration [2], which comprises at least two different pinning directions of the magnetically fixed layers. The main fabrication problem is the setting of different pinning directions on a local scale. Currently various methods are used to create different pinning directions: i) manifold deposition in an applied magnetic field with intervening lithography [3, 4], ii) local heating in an applied magnetic field [5], iii) inhomogeneous applied field during deposition and combinations thereof. All of these techniques are rather complex and time consuming. As an alternative approach He ion irradiation in an applied magnetic field can be used [6]. Facilitating resist masks a homogeneous post deposition ion irradiation allows the setting of the pinning direction in the uncovered regions in any direction required [7, 8].

As a test system the following multilayer structure was used:

Si/SiO_2/Ta(5.5 nm)/NiFe(6 nm)/Co(3 nm)/Cu(3 nm)/Co(3.6 nm)/FeMn(10 nm)/Ta(5.5 nm)

After sputter deposition and magnetic initialization of the multilayer stack during deposition the Wheatstone bridge has been prepared using optical lithography and Ar dry etching. Finally the

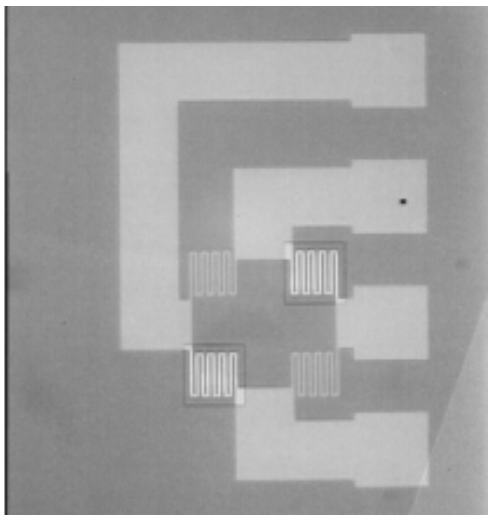

Fig. 1: Optical image of the Wheatstone bridge, comprising four spin-valve meander structures and connection leads. The whole structure apart from two meander structures is covered with PMMA resist.

[1] In collaboration with D. Engel, M. Jung, A. Ehresmann, H. Schmoranzer, Fachbereich Physik, Universität Kaiserslautern, Germany; and K.-U. Barholz, R. Mattheis, IPHT Jena, Germany.

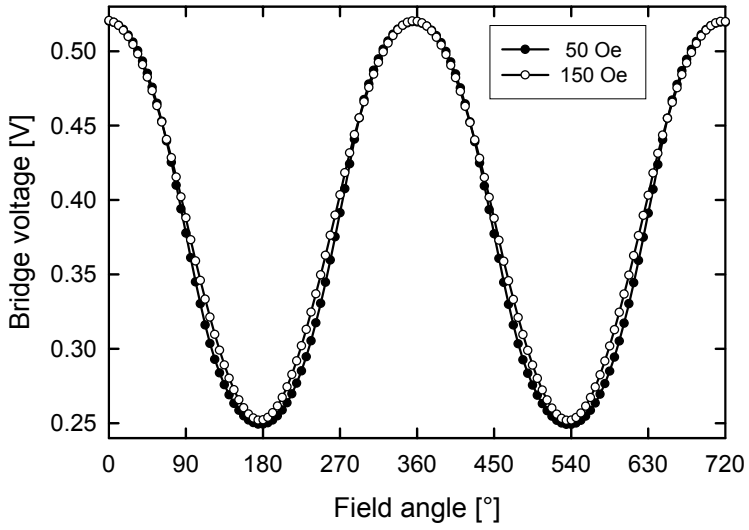

Fig. 2: Wheatstone bridge voltage as a function of the in-plane field angle for two different field magnitudes as indicated. The bridge voltage is 5 V.

structure has been covered with a 700 nm thick PMMA resist. The thickness of the resist has been chosen to completely stop the He ions during irradiation. Two windows have been opened in the resist layer in order to uncover two non-neighborhood sensing elements of the Wheatstone bridge. An optical image of the whole structure is presented in Fig. 1. Next the sample is homogeneously irradiated with 10 keV He ions with an ion dose of 6×10^{14} ions/cm^2 in a magnetic field applied antiparallel to the initial pinning direction. For a detailed description of the reversal of the pinning direction see Ref. [6].

In Fig. 2 the bridge voltage of the sensor element is shown as a function of the in-plane angle of the driving field for two different field magnitudes as indicated. In both cases a good performance of the Wheatstone bridge sensor element is found. First experiments using IrMn as antiferromagnetic material have also been successfully performed. Compared to the methods described above the use of ion irradiation for the fabrication of magnetic sensor devices is much easier.

T.M. acknowledges support by the Studienstiftung des deutschen Volkes.

References

[1] R. Coehoorn, *Giant magnetoresistance in Exchange-Biased Spin-Valve Layered Structures and its Application in Read Heads*, in: *Magnetic multilayers and giant magnetoresistance: fundamentals and industrial applications*, U. Hartmann (Ed.) Springer Series in Surface Science **37**, 65 (2000).
[2] J. Daughton, J. Brown, E. Chen, R. Beech, A. Pohm, W. Kude, IEEE Trans. Magn. **30**, 4608 (1994).
[3] K.M.H. Lenssen, D.J. Adelerhof, H.J. Gassen, A.E.T. Kuiper, G.H.J. Somers, J.B.A.D. van Zon, Sens. Actuators A **85**, 1 (2000).
[4] C.P.O. Treutler, Sens. Actuators A **91**, 2 (2001).
[5] J.K. Spong, V.S. Speriosu, R.E. Fontana, M.M. Dovek, T.L. Hylton, IEEE Trans. Magn. **32**, 366 (1996).
[6] A. Mougin, T. Mewes, M. Jung, D. Engel, A. Ehresmann, H. Schmoranzer, J. Fassbender, B. Hillebrands, Phys. Rev. B **63**, 060409(R) (2001).
[7] A. Mougin, S. Poppe, J. Fassbender, B. Hillebrands, G. Faini, U. Ebels, M. Jung, D. Engel, A. Ehresmann, H. Schmoranzer, J. Appl. Phys. **89**, 6606 (2001).
[8] J. Fassbender, S. Poppe, T. Mewes, A. Mougin, B. Hillebrands, D. Engel, M. Jung, A. Ehresmann, H. Schmoranzer, G. Faini, K. J. Kirk, J. N. Chapman, Phys. Stat. Sol. (b), in press.

E. Elastic Properties

6.18 Effective elastic constants of boron nitride films

T. Wittkowski, K. Jung, J. Jorzick, and B. Hillebrands[1,2]

Investigations of various cubic and hexagonal boron nitride films with the Brillouin light scattering (BLS) technique provide insight into their elastic properties in detail. The microscopic elastic behavior is averaged over some characteristic length of the order of the phonon wavelength (0.3 – 1 μm). The obtained so-called effective elastic constants reveal a more or less pronounced elastic anisotropy of the film material. The anisotropies measured so far are moderate, $c_{11}/c_{33} = 4/5$, for thick sputtered cubic boron nitride films (c-BN)[1] and they are as small as $c_{11}/c_{33} = 0.1$ for special hexagonal BN films (h-BN)[2]. The subject of this study is to investigate the texture of typical nanocrystalline materials as a possible cause for the observed elastic anisotropy.

The macroscopic elastic behavior of a polycrystalline material is related to the single-crystal elastic constants by the averaging procedures first described by Voigt and by Reuss [1]. The Voigt averaging procedure assumes the continuity of the strain field and the Reuss averaging the continuity of the stress field at the grain boundaries. For a constant strain field Hooke's law for a macroscopic aggregate of crystallites reads in terms of the stiffness constants $\sigma_{MN} = \tilde{c}_{MNRS}\varepsilon_{RS}$, σ and ε being the stress and the strain tensor, respectively. The effective stiffness constants are expressed as

$$\tilde{c}_{MNRS} = N^{-1}\int d\psi_q a_{Mi} a_{Nj} a_{Rk} a_{Sl} c_{ijkl} \tag{1}$$

with the elastic tensor of the single crystal, c_{ijkl}. The integration extends over the respective crystallite orientation distribution expressed in terms of the direction cosines a, the a's being functions of the angular distribution ψ_q. N denotes the normalization integral. Following the same procedure for a constant stress field yields the effective compliances, $\tilde{s}_{MNRS}$. It can be shown that the Voigt and the Reuss averages, which both use idealized elastic boundary conditions, represent the upper and lower bounds of the true elastic tensor components, C_{MNRS}

$$\tilde{c}_{MNRS} \geq C_{MNRS} \geq \left(\tilde{s}_{MNRS}\right)^{-1} \tag{2}$$

For the calculation of the effective constants of the aggregate it is appropriate to use the two-suffix notation of the stiffness and compliance tensors. Since the investigated film materials possess axial symmetry about the surface normal, the integration in Eq. 1 is simplified further. In the following we use the notation c_{ij}^{V} and $c_{ij}^{R} = \left(s_{ij}\right)^{-1}$ for the Voigt and Reuss averages, respectively. A specified aggregate texture is defined such that the respective crystallite axes are oriented parallel to the film normal in x_3-direction.

For the c-BN film an XRD and a transmission electron microscopy (TEM) analysis revealed a nanocrystalline [110] textured microstructure. The film grows in columnar grains of a few ten nanometers in diameter. The effective stiffness constants were deduced from the phase velocity of acoustic bulk and surface phonons observed with BLS. Compared to the values of a c-BN single crystal the film material exhibits a reduced overall stiffness, and the bulk modulus of the

[1] In collaboration with M. Keunecke and K. Bewilogua, Fraunhofer IST, Braunschweig, Germany.
[2] In collaboration with E. Weissmantel and F. Richter, TU Chemnitz, Germany.

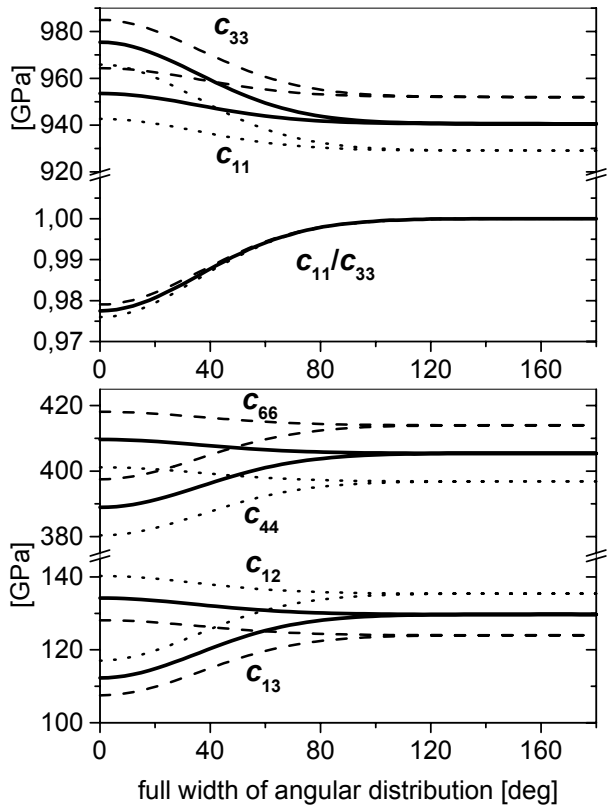

Fig. 1: Effective elastic constants of an aggregate of [110] oriented c-BN crystallites as a function of the texture strength. The ascissa shows the full width at 1/e of the maximum value of a Gaussian distribution of the <110> axes about the surface normal. Dashed lines show the Voigt averages, dotted lines show the Reuss averages, their mean value is indicated by the full lines. The perfectly oriented material exhibits hexagonal symmetry with most pronounced anisotropy $c_{11}/c_{33} = 0.978$. For broad distributions the constants degenerate and adopt the well known isotropic values of completely randomly oriented crystallites. The used single crystal constants are those of Ref. [3]: $c_{11} = 820$ GPa, $c_{12} = 190$ GPa, $c_{44} = 480$ GPa.

film is 3/4 of that of the single crystal. The elastic tensor possesses hexagonal symmetry, the anisotropy factor $A_1 = c_{11}/c_{33}$ amounts to 4/5 [2].

In order to evaluate the influence of the film texture on the anisotropy the effective elastic constants of an aggregate of [110] oriented c-BN crystallites were calculated. The aggregate tensor exhibits hexagonal symmetry. As mentioned above a hexagonal model is also used in the BLS analysis. Therefore the elastic constants can be compared directly with each other. Figure 1 shows the constants of the aggregate's elastic tensor as a function of the texture strength. For broad angular distributions of the <110> axes about the film normal the constants degenerate and adopt the values of the isotropic tensor corresponding to a fully random crystallite orientation. From Fig. 1 it is obvious that the anisotropy $c_{11}/c_{33} \approx 0.98$ of the perfectly textured aggregate makes only a small contribution to the measured anisotropy of 0.8. The influence of sp^2-bonded material at the grain boundaries and the shape anisotropy of the cubic crystallites are therefore relevant for the observed anisotropy and for the reduced bulk modulus. Due to the enormous difference in the overall stiffness of sp^3-bonded and sp^2-bonded BN the localization of the latter at the grain boundaries is responsible for both effects.

In case of the h-BN films the BLS analysis of the dispersion of surface phonons revealed an extreme elastic anisotropy down to $c_{11}/c_{33} = 0.1$ [4]. It is known from TEM investigations that for these films the hexagonal *c*-axes of the nanocrystallites orient perpendicular to the film normal. This is due to the minimization of the Gibb's free energy in a biaxial compressive stress field.

Figure 2 shows the anisotropy factor c_{11}/c_{33} for a textured h-BN aggregate as a function of the tilt angle of the <0001> axes measured from the surface normal. The pronounced single crystal anisotropy of h-BN, which is comparable with that of graphite, leads to an aggregate anisotropy which varies over two orders of magnitude. Especially the extreme anisotropy observed in the experiment is in good agreement with the calculated result for the aggregate with 90°-tilted <0001> axes. In Fig. 3 it is documented that even an imperfect texture does not change the ag

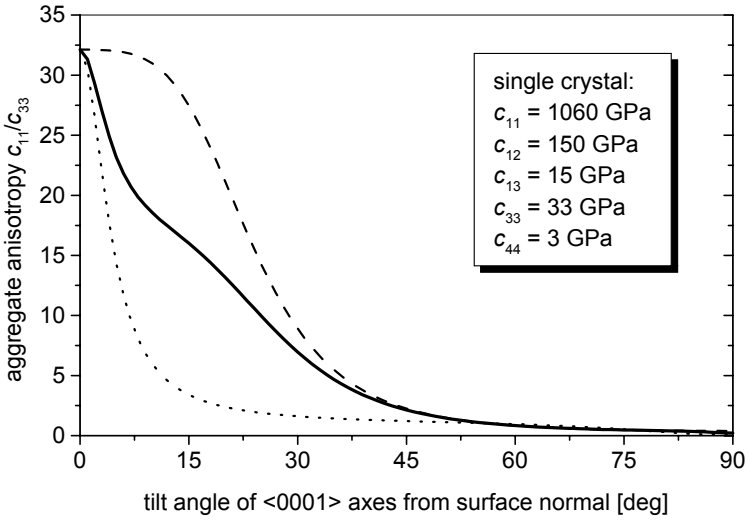

Fig. 2: Elastic anisotropy c_{11}/c_{33} of an aggregate of hegagonal BN crystallites as a function of the tilt angle of the crystallite c-axes. The c-axes possess random in-plane orientation. The resulting aggregate anisotropy varies over two orders of magnitude. Voigt, Reuss and mean value are indicated by the dashed, dotted and full line, respectively. The mean value is $c_{11}/c_{33} = \left(c_{11}^{V} - c_{11}^{R}\right)/\left(c_{33}^{V} - c_{33}^{R}\right)$. The single crystal constants used for the calculation are a mixture of constants of h-BN and graphite, see ref. [4].

gregate anisotropy much. Note, that the bulk modulus of the aggregate depends on the applied averaging procedure. For the 90°-tilted *c*-axes the Voigt stiffnesses correspond to a higher bulk modulus than the Reuss compliances. The bulk moduli of the films deduced from the BLS analysis lie slightly above those of the Reuss aggregate.

This means that the film anisotropy ratio c_{11}/c_{33} as well as the film bulk modulus is in surprisingly good agreement with the calculated results for an aggregate of hexagonal crystallites whose *c*-axes lie perpendicular to the surface normal. It is a remarkable result that the measured effective elastic behavior of these films is distinctly better reproduced by the assumption of continuity of stress (Reuss) than of continuity of strain (Voigt).

In a comparison of the c-BN and the h-BN films it becomes clear that, in case of h-BN, the elastic anisotropy and the bulk modulus are represented much better by a polycrystalline aggregate than in the case of c-BN. These differences are attributed to the different role of the sp^2-bonded grain boundaries in both materials. Since this material is much more compliant than the c-BN crystallites it reduces the c-BN film stiffness drastically. This fact, combined with the columnar growth, induces the film anisotropy which cannot be explained by the film texture. Thus the

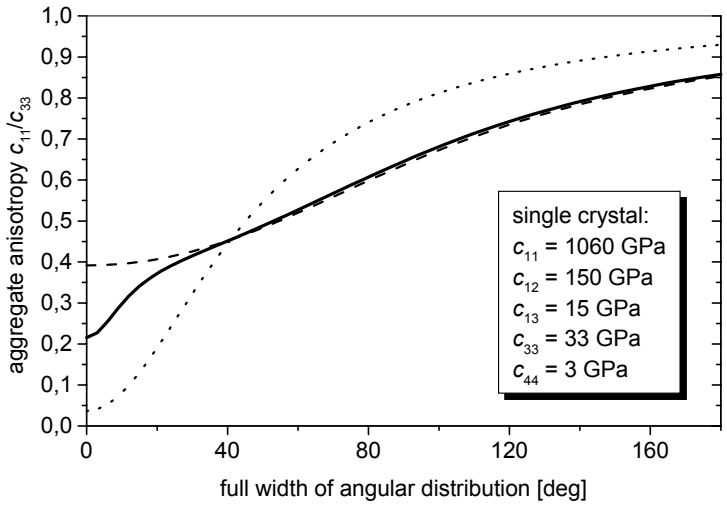

Fig. 3: Elastic anisotropy c_{11}/c_{33} of an aggregate of hexagonal BN crystallites as a function of the texture strength. The abscissa shows the full width at 1/e of the maximum value of a Gaussian distribution of the <0001> axes about the directions perpendicular to the surface normal. Dashed lines show the Voigt averages, dotted lines show the Reuss averages, their mean value, calculated as for Fig. 2, is indicated by the full lines. The variation of the aggregate anisotropy with the broadness of the distribution is moderate.

textured aggregate of c-BN crystallites provides an insufficient model for describing essential elastic properties of these kind of films[3]. This is different for the h-BN films. Here, the sp^2-bonded amorphous grain boundaries possess a similar stiffness as the crystalline material fraction. As was shown it is the film texture in combination with the pronounced single crystal anisotropy which leads to the observed film anisotropy. A structured film growth, if present, would have a much smaller relative influence on the film anisotropy than in the case of c-BN. An appropriate description of the effective elastic behavior of the c-BN films would thus require a model that incorporates the spatial arrangement of the two material phases.

Financial support by the Deutsche Forschungsgemeinschaft is gratefully acknowledged.

References

[1] M.J.P. Musgrave, *Crystal Acoustics*, Holden Day, San Francisco, 1970.
[2] T. Wittkowski, J. Jorzick, K. Jung, B. Hillebrands, M. Keunecke, K. Bewilogua, *A Brillouin light scattering study on the elastic properties of thick sputtered c-BN films*, submitted to J. Appl. Phys..
[3] M. Grimsditch, E.S. Zouboulis, J. Appl. Phys. **76**, 832 (1994).
[4] T. Wittkowski, P. Cortina, J. Jorzick, K. Jung, B. Hillebrands, Diam. Rel. Mat. **9**, 1957 (2000).
[5] X. Jiang, J.V. Harzer, B. Hillebrands, Ch. Wild, P. Koidl, Appl. Phys. Lett. **59**, 1055 (1991).

[3] These results may be compared with those on polycrystalline diamond films [5]. In case of the diamond films the sp^2-bonded material fraction at the grain boundaries is negligible. Although the single crystal anisotropy of diamond (1.21) is smaller than that of c-BN (1.52) the effective elastic constants of the polycrystalline diamond film agree completely with those of a textured aggregate.

F. Transfer of Technology

6.19 Plasma beam deposition of biocompatible thin films

L. Kleinen, H. Busch, U. Grabowy, K. Jung, and B. Hillebrands[1]

The work in the Institute for Thin Film Technology is aimed at the development of hard coatings for special applications in small and medium sized companies. Thin films of amorphous carbon modifications (DLC, ta-C, a-C and a-C:H) and several ceramic materials like WC/C, TiN, TiAlN, SiC and CrN have been developed for a variety of industrial applications. These efforts were supported by adapting the available coating plants and also by construction of new mounting equipment to meet specific customer requests, like, e.g., for all-around coating of miniature ball bearings with WC/C by magnetron sputtering.

Special emphasis is placed on the development and characterization of amorphous carbon thin films for biological equipment, medical implants and surgical instruments. As an example of our work the adaptation of amorphous carbon coatings to vascular stents (implants that keep clogged vessels open for the blood flow) are described.

In the field of cardiovascular implants a good hemocompatibility as well as a sufficient surface coverage with endothelial cells after the implantation are required.

Tests on the hemocompatibility and antithrombogenicity of amorphous carbon thin films were amongst other performed by *M.I. Jones* et al. by observing interactions of different surfaces with rabbit blood platelets [5]. The morphology of blood platelets on titanium and amorphous carbon substrates after an incubation period of 60 minutes differ largely. On the titanium surface the typical indications of an inflammatory process (seriously deformed blood platelets and severe fibrin formation) can be seen, whereas on amorphous carbon no hemolytic effect, no platelet activation and no tendency towards thrombus formation appear.

Based on the experiences of the past few years [1, 2, 3] we deposited elastic amorphous carbon films on a typical vascular stent. In cooperation with the Institute for Cell Biology of the University Bonn we studied the cell response to the amorphous carbon surface.

The experiments were performed with a plasma beam source of CCR GmbH. This plasma source is characterized by a very effective rf excitation of the plasma, the gas pressure can be chosen to be very low, and the delay time of the gas molecules in the source is short. Therefore predominantly $C_2H_2^+$ or C_2H^+ ions leave the plasma source. In the deposition process the ion energy and the ion flux are reduced by a factor of ten with respect to the conditions typical for the production of diamond-like carbon films. Thus the energy flux density is reduced by two orders of magnitude. The temperature of the substrate is practically not increased during the deposition process. Therefore this technique qualifies even for the coating of highly temperature sensitive materials (e.g. polymer catheters) with amorphous carbon. Despite the fact that the impinging ions have only a kinetic energy of 20 eV the deposited films are rather hard and scratch resistant with respect to steel. The films exhibit a Vickers hardness of H = 10 GPa and an elasticity of E = 60 GPa. The ratio E/H of 6 is in agreement with the constraint model of Angus [4]. That means the carbon films are thermodynamically stable.

[1] In collaboration with: nttf GmbH, 53619 Rheinbreitbach; V. Herzog and I. Gestmann, Institut für Zellbiologie, Universität Bonn, 53121 Bonn.

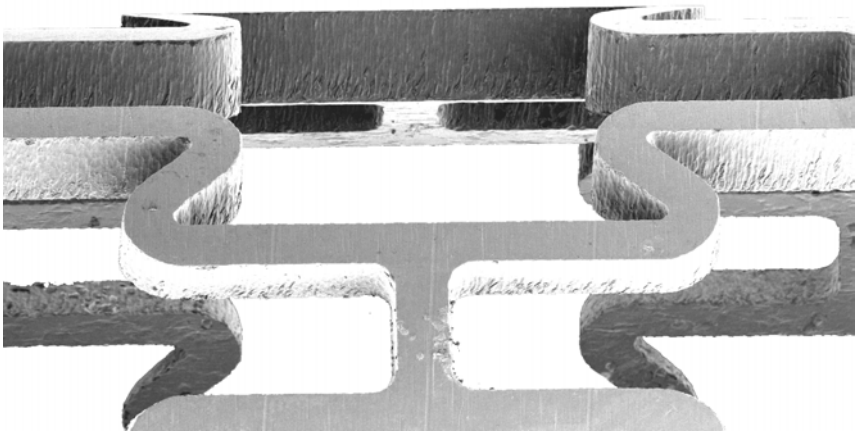

Fig. 1: Uncoated stent after two days in a culture of CHO-cells. The surface is hardly covered with cells.

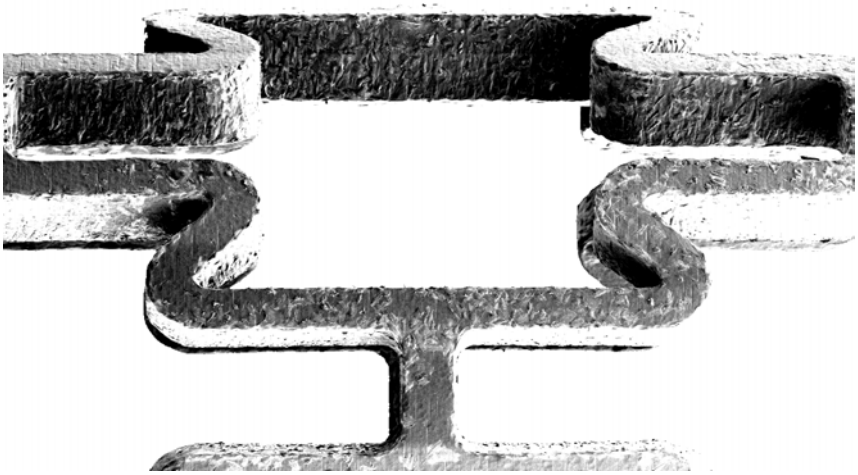

Fig. 2: Carbon coated stent after two days in a culture of CHO-cells. The surface is covered extremely well with cells.

The cell culture experiments were performed by Dipl.-Biol. Ingo Gestmann. (Picture with friendly permission of Prof. V. Herzog and Dipl.-Biol. Ingo Gestmann, Institut für Zellbiologie, Universität Bonn.)

First biological tests with CHO (chinese hamster ovary) cells show significant differences between the uncoated and the coated stent. The surface of the uncoated stent is hardly covered with cells whereas the surface of the amorphous carbon coated stent are covered extremely well with cells. Corresponding experiments with human endothelial cells will be performed.

Work supported by the Stiftung für Innovation of the state of Rheinland-Pfalz.

References

[1] M. Weiler, S. Sattel, T. Giessen, K. Jung, H. Ehrhardt. V.S. Veerasami, J. Robertson, *Preparation and properties of highly tetrahedral hydrogenated amorphous carbon*, Phys. Rev. B **53**, 1594 (1996).

[2] R. Kleber, M. Weiler, A. Krüger, S. Sattel, G. Kunz, K. Jung, H. Ehrhardt, *Influence of ion energy and flux composition on the properties of plasma-deposited amorphous carbon and amorphous hydrogenated carbon films*, Diam. Rel. Mat. **2**, 246 (1993).

[3] C. Osthöver, K. Jung, and B. Hillebrands, *Plasma beam deposition of hard amorphous carbon films*, AG Magnetismus, Annual Report (2000).

[4] J.C. Angus, P. Koidl, S. Domitz, *Carbon Thin Films*, in: *Plama Deposited Thin Film* (Ed.: J. Mort und F. Jansen), CRC press, Cleveland (1986).

[5] M. I. Jones, I. R. McColl, D. M. Grant, K. G. Parker, T. L. Parker, *Protein adsorption and platelet attachment and activation on TiN, TiC, and DLC coatings on titanium for cardiovascular applications*, Journal of Biomedical Materials Research **52**, 413 (2000).

Chapter 7: Publications

7.1 Published

1. *Brillouin light scattering from surface phonons in hexagonal and cubic boron nitride films*
   T. Wittkowski, P. Cortina, J. Jorzick, K. Jung, B. Hillebrands
   Diam. Rel. Mat. **9**, 1957 (2000).
2. *Successful suppression of magnetization precession after short field pulses*
   M. Bauer, R. Lopusnik, J. Fassbender, B. Hillebrands, H. Dötsch
   IEEE Trans. Magn. **36**, 2764 (2000).
3. *Modification of the exchange bias effect by He ion irradiation*
   A. Mougin, T. Mewes, R. Lopusnik, M. Jung, D. Engel, A. Ehresmann, H. Schmoranzer, J. Fassbender, B. Hillebrands
   IEEE Trans. Magn. **36**, 2647 (2000).
4. *Comparative study of the epitaxial growth of Cu on Mg(001) and on hydrogen terminated Si(001)*
   T. Mewes, M. Rickart, A. Mougin, S.O. Demokritov, J. Fassbender, B. Hillebrands, M. Scheib
   Surf. Sci. **481**, 87 (2001).
5. *Magnetic micropattering of FeNi/FeMn exchange bias bilayers by ion irradiation*
   A. Mougin, S. Poppe, J. Fassbender, B. Hillebrands, G. Gaini, U. Ebels, M. Jung, D. Engel, A. Ehresmann, H. Schmoranzer
   J. Appl. Phys. **89**, 6606 (2001).
6. *Local manipulation and reversal of the exchange bias field by ion irradiation in FeNi/FeMn double layers*
   A. Mougin, T. Mewes, M. Jung, D. Engel, A. Ehresmann, H. Schmoranzer, J. Fassbender, B. Hillebrands
   Phys. Rev. B **63**, 060409(R) (2001).
7. *Magnetization dynamics and concepts for fast magnetic switching*
   B. Hillebrands, J. Fassbender, S.O. Demokritov
   Magnetoelektronik, VDI-Technologiezentrum (2001) (ISBN 3-931384-31-4).
8. *Magneto-dipole coupling in arrays of micron-size rectangular elements*
   J. Jorzick, C. Krämer, S.O. Demokritov, B. Hillebrands, E. Søndergard, M. Bailleul, C. Fermon, U. Memmert, A.N. Müller, A. Kounga, U. Hartmann, E. Tsymbal
   J. Magn. Magn. Mater. **226**, 1835 (2001).
9. *Study of the oxidation processes of insulating barriers in magnetic tunnel junctions*
   B.F.P. Roos, P.A. Beck, S.O. Demokritov, B. Hillebrands
   J. Appl. Phys. **89**, 6656 (2001).
10. *Time domain MOKE detection of spin wave modes and precession control of magnetization*
    M. Bauer, R. Lopusnik, H. Dötsch, B.A. Kalinikos, C.E. Patton, J. Fassbender, B. Hillebrands.
    J. Magn. Magn. Mater. **226**, 507 (2001).

11. *Interlayer exchange coupling in layered magnetic structures*
D.E. Bürgler, S.O. Demokritov, P. Grünberg, M.T. Johnson
Handbook of Magnetic Materials, vol 13, K.J.H. Buschow (ed.), Elsevier, Amsterdam (2001).
12. *Spin wave quantization in laterally confined magnetic structures*
J. Jorzick, S.O. Demokritov, B. Hillebrands
J. Appl. Phys. **89**, 7091 (2001).
13. *Nonlinear waves in one- and two-dimensional magnetic waveguides*
A.N. Slavin, S.O. Demokritov, B. Hillebrands
in: *Spin dynamics in confined magnetic structures I*, B. Hillebrands, K. Ounadjela (eds.), Springer, Berlin, Heidelberg, New York (2001).
14. *Spin waves in laterally confined magnetic structures*
S.O. Demokritov, B. Hillebrands
in: *Spin dynamics in confined magnetic structures I*, B. Hillebrands, K. Ounadjela, (eds.), Springer, Berlin, Heidelberg, New York (2001).
15. *Magnetooptic ellipsometry in multilayers at arbitrary magnetization*
S. Visnovsky, R. Lopusnik, M. Bauer, J. Brok, J. Fassbender, B. Hillebrands
Optics Express **9**, 121 (2001).
16. *Brillouin light scattering studies of confined spin waves: linear and nonlinear confinement*
S.O. Demokritov, B. Hillebrands, A.N. Slavin
Phys. Rep. **348**, 442 (2001).
17. *Numerical investigations on the switching behavior of magnetic tunnel junctions in the quasi-static and dynamic regime*
J. Fassbender, M. Bauer
Europhys. Lett. **55**, 119 (2001).
18. *Growth morphology in the Co/Cu(001) system*
J. Fassbender, A. Bischof, R. Allenspach, O. May, M. Lange, U. Rüdiger, G. Güntherodt
Surf. Sci. **488**, 99 (2001)

7.2 in press

1. *Elastic properties of indium tin oxide films*
T. Wittkowski, J. Jorzick, H. Seitz, B. Schröder, K. Jung, B. Hillebrands
Thin Solid Films, in press.
2. *Influence of submonolayer carbon contamination on the growth of epitaxial metallic layers on MgO substrates*
M. Rickart, B.F.P. Roos, T. Mewes, J.Jorzick, S.O. Demokritov, B. Hillebrands
Surf. Sci. Lett., in press.
3. *Switching dynamics and write endurance of magnetic tunnel junctions*
M. Bauer, R. Lopusnik, J. Fassbender, B. Hillebrands, J. Bangert, J. Wecker
J. Appl. Phys., in press.

4. *Magnetization reversal of exchange bias double layers magnetically patterned by ion irradiation*
   J. Fassbender, S. Poppe, T. Mewes, A. Mougin, B. Hillebrands, D. Engel, M. Jung, A. Ehresmann, H. Schmoranzer, G. Faini, K.J. Kirk, J.N. Chapman
   Phys. Stat. Sol., in press.

7.3 submitted

1. *Auger electron spectroscopy studies of annealing effects on Al/Fe, Al/FeO/Fe and Al/CoO/Co interfaces*
   B.F.P. Roos, P.A. Beck, S.O. Demokritov, B. Hillebrands
   Submitted to Surf. Sci. Lett.
2. *A Brillouin light scattering study on the elastic properties of thick sputtered c-BN films*
   T. Wittkowski, J. Jorzick, K. Jung, B. Hillebrands, M. Keunecke and K. Bewilogua
   Submitted to J. Appl. Phys.
3. *Spin wave wells in micrometer size magnetic elements*
   J. Jorzick, S.O. Demokritov, B. Hillebrands, D. Berkov, N.L. Gorn, K. Guslienko, A.N. Slavin
   Submitted to Phys. Rev. Lett.
4. *Switching dynamics of magnetic tunnel junctions*
   J. Fassbender, M. Bauer, B. Hillebrands, J. Bangert, J. Wecker
   Submitted to J. Appl. Phys.
5. *Tuning exchange bias and coercive fields in ferromagnet/antiferromagnet bilayers with ion irradiation*
   J. Juraszek, J. Fassbender, S. Poppe, T. Mewes, B. Hillebrands, D. Engel, A. Kronenberger, A. Ehresmann, H. Schmoranzer
   Submitted to J. Appl. Phys.

Chapter 8: Conferences, Workshops, Schools and Seminars

(shown in chronological order with the speaker named)

8.1 Conferences

8.1.1 Invited talks

B. Hillebrands:

Dynamic properties of patterned magnetic films
25th Annual Meeting: Advances in Surface and Interface Physics, Modena, Italy, December 2000

B. Hillebrands:

Spin waves quantization in laterally confined magnetic structures
8th Joint MMM-Intermag Conference, San Antonio, USA, January 2001

J. Fassbender:

Sub-Nanosekunden Schalten von magnetischen Tunnelelement-MRAM-Stukturen
DPG Frühjahrstagung, Hamburg, Germany, March 2001 (Hauptvortrag)

B. Hillebrands:

Preparation of extremely thin AlO and nitride films using a novel low energy plasma beam process
International Conference on Metallurgical Coatings and Thin Films, San Diego, USA, May 2001

J. Fassbender:

Ion irradiation for magnetic sensor applications
Seeheim Conference on Magnetism, Seeheim, Germany, September 2001

8.1.2 Contributed talks and posters

1 contribution: 44th Conference on Magnetism and Magnetic Materials, San Jose, USA, October 1999

6 contributions: 8th Joint MMM-Intermag Conference, San Antonio, USA, January 2001

4 contributions: 248. Heraeus-Seminar, Bad Honnef, Germany, January 2001

12 contributions: DPG-Frühjahrstagung Hamburg, Germany, March 2001

2 contributions: Intermag 2000, International Magnetics Conference, Toronto, Canada, April 2000

4 contributions: ICMCTF, San Diego, USA, May 2001

5 contributions: MML´01, Aachen, Germany, June 2001

1 contribution: 8th c-BN expert meeting, Stuttgart, Germany, October 2001

8.2 Workshops

8.2.1 Invited lectures

B. Hillebrands:

Schichtsysteme, Streifen und Inseln in Kaiserslautern
Klausurtagung des SFB 277 (Saarbrücken), Homburg, Germany, November 2000

T. Mewes:

Lokale Modifikation der Pinning-Stärke und Richtung in Exchange-Bias-Schichten für Sensoranwendungen
6. Symposium Magnetoresistive Sensoren, Wetzlar, Germany, March 2001

J. Fassbender:

Magnetization dynamics of magnetic tunnel junction MRAM devices
Workshop on Magnetization Dynamics, Orsay, France, April 2001

S.O. Demokritov:

Barrierenbildung bei magnetischen Tunnelübergängen: "Ion-Embedding" gegen Diffusion
17. Sitzung des AK "Magnetische Schichten für technische Anwendungen", Halle, Germany, June 2001

B. Hillebrands:

Spin dynamics in the regime of spin precession at GHz frequencies
Joint Summer Workshop on Mesomagnetism, Spin Dynamics and Spin Electronics, Santorini, Greece, July 2001

B. Hillebrands:

Dynamic properties of patterned media
International Workshop on Ferromagnet-Semiconductor Nanostructures, Regensburg, Germany, July 2001

S.O. Demokritov:

Non-monotonic magnetic anisotropy in Fe films grown on vicinal Ag and Au(001) surfaces
258th Heraeus Seminar: Electronic origin of magnetoelastic anisotropy, Tegernsee, Germany, September 2001

B. Hillebrands:

Non-monotone step induced magnetic anisotropy of vicinal Fe films on Au(001)
ESF-NANOMAG meeting, Anglet, France, October 2001

8.2.2 Contributed talks and posters

M. Rickart:

Magnetische Anisotropien epitaktischer Fe-Filme auf vizinalen Ag(001) und Au(001) mit verschiedenen Verschnittorientierungen
Workshop des Graduierten-Kollegs "Laser und Teilchenspektroskopie", Bad Münster am Stein, Germany, December 2000

R. Lopusnik:

Zeitaufgelöste Messungen der Magnetisierungsdynamik auf der sub-Nanosekunden-Zeitskala
Workshop des Graduierten-Kollegs "Laser und Teilchenspektroskopie", Bad Münster am Stein, Germany, December 2000

J. Jorzick:

Spinwellen und dipolare Kopplung in Feldern von mikrometergroßen magnetischen Inseln
Workshop des Graduierten-Kollegs "Laser und Teilchenspektroskopie", Bad Münster am Stein, Germany, December 2000

S.O. Demokritov:

Non-monotonic uniaxial surface anisotropy of Fe films prepared on vicinal Ag and Au layers
Joint Summer Workshop on Mesomagnetism, Spin Dynamics and Spin Electronics, Santorini, Greece, July 2001

J. Fassbender:

Sub-nanosecond magnetization switching in magnetic tunnel junction prototype structures
1st European Workshop on Mass Storage Technology IMST 2001, Grenoble, France, April 2001

8.3 Schools

8.3.1 Invited lectures

S.O. Demokritov:

Light Scattering from spin waves in quantum dots and wires
Nanotubes & Nanostructures 2001, Frascati, Italy, October 2001

8.4 Invited colloquia and seminars

B. Hillebrands:

Dynamic properties of patterned magnetic films
Center for Materials for Information Technology (MINT), Tuscaloosa, USA, January 2001

B. Hillebrands:

Dynamische Prozesse magnetischer Speicherelemente
Symposium "Magnetoelektronik", IPHT Jena, January 2001

B. Hillebrands:

Dynamic properties of patterned magnetic films
Colloquium of the MPI Halle, Germany, February 2001

B. Hillebrands:

Kohlenstoff-Schichten für die Medizin
Vortrag anlässlich der Pressekonferenz der Landesregierung Rheinland-Pfalz zur Landes-Forschungsförderung, März 2001

B. Hillebrands:

Magnetic sensor elements: tayloring the exchange bias effect and the magnetic tunnel barrier
IBM Mainz, March 2001

J. Fassbender:

Local manipulation and reversal of the exchange bias field by ion irradiation for magnetic sensor applications
LPN Bagneux, France, April 2001

B. Hillebrands:

Brillouin light scattering from spin waves in confined magnetic structures
Hawaiian Institute of Geophysics and Planetology, Manoa, Hawaii, USA, May 2001

S.O. Demokritov:

Spindynamik in magnetischen Strukturen
SFB-Kolloquium, Konstanz, Germany, June 2001

S.O. Demokritov:

Propagation of nonlinear spin waves in magnetic films
Seminar, Bayreuth, Germany, July 2001

B. Hillebrands:

Schnelle Magnetisierungsdynamik in kleinen magnetischen Inseln
Physikalisches Kolloquium, Universität Stuttgart, Germany, May 2001

8.5 Contributions to other meetings

S. Poppe:

Local manipulation and reversal of the exchange bias field by ion irradiation
DYNASPIN-Meeting, Kaiserslautern, Germany, December 2000

S.O. Demokritov:

Excitations of spin waves
DYNASPIN-Meeting, Kaiserslautern, Germany, December 2000

S.O. Demokritov:

Brillouin Lichtstreusprektroskopie an Spinwellen
BMBF-Leitprojekttreffen, Halle, Germany, December 2000

S.O. Demokritov:

Light scattering on excited spin waves
INTAS Projekttreffen, Bochum, June 2001

8.6 Exhibitions and Fairs

The Institute of Thin Film Technology (IDST) presented posters and demonstrators of coated medical implants at the

- Medica 2000, Düsseldorf , November 22 – 25, 2000
- Hannover Industriemesse, Hannover, April 23 – 27, 2001
- Materialica, München, October 01 – 04, 2001
- BioTechnica, Hannover, October 09 – 11, 2001